UNIVERSITÀ DEGLI STUDI DI PADOVA

UNIVERSITÀ DEGLI STUDI DI PADOVA

Dipartimento Di Ingegneria Dell'Informazione DEI

Corso Di Laurea In Bioingegneria Industriale

Tool Wear Impact On The Superelasticity Of A Wrought And Additive Manufacturing Nitinol For Biomedical Applications

Relatore: Prof.ssa Rachele Bertolini

Correlatore: Prof.ssa Stefania Bruschi

Laureanda: Flavia Tucci

Matricola n. 2038470

ANNO ACCADEMICO 2023 – 2024

Contents

LIST OF FIGURES

LIST OF TABLES

SUMMARY

Chapter 1 introduces Nitinol, from its discovery to the explanation of its peculiar properties of shape memory and superelasticity. The fundamental role of this alloy in biomedical applications is deepened, particularly where its superelasticity is exploited. In addition, the main production processes of Nitinol are reported, from conventional to innovative, namely Additive Manufacturing (AM). The latter is analyzed through a specific process chain, validated in a previous study, which includes the fabrication of the workpiece through Laser Powder Bed Fusion (LPBF) technique, followed by heat treatments and machining. The complexity of the machinability of Nitinol is underlined, attributable to its unconventional stress-strain properties, with a focus on the challenges related to tool wear. In addition, a detailed overview of tool wear is provided, with particular attention to its causes and effects on Nitinol, since tool wear is one of the major factors that limit the use of this material, having a strong impact on machining performance and final product quality. The chapter concludes by underlying the importance of deepening the studies on tool wear of Nitinol manufactured by AM. This thesis aims to fill this gap by evaluating the effects of tool wear on machining, highlighting the differences between conventional and AM Nitinol, with particular attention to the variation of cutting parameters, specifically the cutting speed, which has been identified as a key factor on which the tool wear depends.

Chapter 2 provides a detailed view of the experimental procedures implemented to conduct the study, outlining the steps involved in characterization and machining of two types of Nitinols. These steps are fundamental to understand the effects of tool wear and evaluate the performance of the materials investigated. It starts from the characterization of the pre-machined materials, which includes the evaluation of the transformation temperatures of the samples through DSC analysis and metallographic analysis to examine the microstructures. Subsequently, the machining process by chip removal is exposed, which is essential to obtain precise final geometries of the parts and to ensure optimal mechanical properties for the applicability of this alloy. Furthermore, the methods of material characterization after machining are described, starting with the evaluation of tool wear, followed by the methods of measuring, and evaluating the latter, as well as DSC and microstructure analyses of the surface areas affected by machining. Moreover, the roughness characteristics of the workpiece are analyzed to determine surface integrity and the procedure for acquiring machining forces is explained.

Chapter 3 presents the results of the experimental tests carried out in two main sections. The first section analyzes the effects of the different cutting speeds applied to the machining on the settled material, while the second highlights the disparities in the results obtained by comparing the two manufacturing methods of Nitinol: conventional and additive. The results are presented through comparisons between the conditions defined in the experimental plan and are enriched by observations that clarify their context and relevance.

Chapter 4 aims to draw significant conclusions from the analysis in the previous chapters, highlighting the inherent limitations of the study and suggesting possible future developments. This section offers a critical reflection on the validity of the results obtained, identifying areas for improvement, and suggesting further research paths to extend the understanding of the studied phenomena.

SOMMARIO

Il **Capitolo 1** costituisce un'introduzione al Nitinol, dalla sua scoperta alla spiegazione delle sue proprietà peculiari di memoria della forma e superelasticità. Viene approfondito il ruolo fondamentale di questa lega nelle applicazioni biomedicali, in particolare in quelle dove viene sfruttata la sua superelasticità. Inoltre, vengono riportati i principali processi di produzione del Nitinol, da quelli convenzionali a quelli innovativi, nello specifico l'Additive Manufacturing (AM). Quest'ultimo viene proposto in combinazione con una specifica catena di processo, già convalidata in un precedente studio, che include la fabbricazione del pezzo tramite la tecnica Laser Powder Bed Fusion (LPBF), seguita da trattamenti termici e lavorazioni meccaniche. Viene sottolineata la complessità della lavorabilità del Nitinol, attribuibile alle sue proprietà non convenzionali, con particolare attenzione alle sfide causate dall'usura degli utensili. Inoltre, viene fornita una panoramica dettagliata dell'usura degli utensili, focalizzandosi sulle sue cause ed effetti sul Nitinol, poiché essa è uno dei principali fattori che limitano l'uso di questo materiale, avendo un forte impatto sulle prestazioni di lavorazione e sulla qualità del prodotto finale. Il capitolo si conclude sottolineando l'importanza di approfondire gli studi sull'usura degli utensili sul Nitinol AM. Questa tesi mira a colmare questa lacuna valutando gli effetti dell'usura degli utensili sulla lavorazione, evidenziando le differenze tra il Nitinol di fabbricazione convenzionale e quello AM, con particolare attenzione alla variazione dei parametri di taglio, nello specifico la velocità di taglio, che è stato identificato come un fattore chiave da cui dipende l'usura degli utensili.

Il **Capitolo 2** fornisce una visione dettagliata delle procedure sperimentali attuate per condurre lo studio, delineando le fasi coinvolte nella caratterizzazione e lavorazione delle due tipologie di Nitinol. Questi passaggi sono fondamentali per comprendere gli effetti dell'usura degli utensili e valutare le prestazioni dei materiali studiati. Si parte dalla caratterizzazione dei materiali pre-lavorazione, che prevede la valutazione delle temperature di trasformazione dei campioni attraverso analisi DSC e analisi metallografica per esaminare le microstrutture. Successivamente viene esposto il processo di lavorazione per asportazione di truciolo, indispensabile per ottenere precise geometrie finali dei pezzi e per garantire proprietà meccaniche ottimali per l'applicabilità di questa lega. Vengono inoltre descritti i metodi di caratterizzazione del materiale dopo la lavorazione, a partire dalla valutazione dell'usura degli utensili, seguita dai metodi di misurazione e valutazione di quest' ultima, nonché delle analisi DSC e microstrutturali delle aree superficiali interessate dalla lavorazione. Inoltre, le

caratteristiche di rugosità del pezzo vengono analizzate per determinare l'integrità della superficie e viene spiegata la procedura per acquisire le forze di lavorazione.

Il **Capitolo 3** presenta i risultati delle prove sperimentali effettuate in due sezioni principali. La prima sezione analizza gli effetti delle diverse velocità di taglio applicate alla lavorazione sul materiale specifico, mentre la seconda evidenzia le differenze nei risultati ottenuti confrontando i due metodi di produzione del Nitinol: convenzionale e additivo. I risultati sono presentati attraverso confronti tra le condizioni definite nel piano sperimentale e sono arricchiti da osservazioni dettagliate che ne chiariscono il contesto e la pertinenza.

Il **Capitolo 4** mira a trarre le conclusioni significative dall'analisi dei capitoli precedenti, evidenziando i limiti intrinseci dello studio e suggerendo possibili sviluppi futuri. Questa sezione offre una riflessione critica sulla validità dei risultati ottenuti, individuando aree di miglioramento e suggerendo ulteriori percorsi di ricerca per estendere la comprensione dei fenomeni studiati.

CHAPTER 1

1. INTRODUCTION

1.1 Nitinol

1.1.1 Historical Overview

In 1951, William J. Buehler began working at the Naval Ordinance Laboratory (NOL) in Maryland and played a crucial role in selecting metal alloys for submarine-launched nuclear re-entry missiles. While investigating different compounds, Buehler discovered that Nickel-titanium (NiTi) alloys exhibited exceptional impact resistance. The term "Nitinol" was introduced, associating the material with the laboratory name. During an accidental fall of NiTi arc bars, Buehler noticed that the piece produced two distinct sounds, which led to understanding the existence of two reversible phases in the material at different temperatures [1]. Further investigations revealed unusual behaviors, including strain recovery and shape memory capability. The alloy initially studied for its variable damping, proved to have significant potential for practical applications. The research team expanded in 1962 and demonstrated the alloy's ability to withstand cyclic loading and recover its original shape when exposed to heat. This discovery opened numerous possibilities for using shape-memory alloys, marking a lucky development in materials science.

1.1.2 Nitinol Properties

Shape memory alloys (SMAs), of which Nickel-Titanium alloy is part, have gained significant prominence in several engineering applications in recent years. Nickel-Titanium (NiTi) stands out as the most utilized SMA, primarily due to its exceptional features, notably the shape memory (SM) and superelasticity (SE) effects. The SM effect occurs due to a thermally induced transformation as a result of the increase in temperature, while the SE effect comes from a stress-induced phase transformation [2]. This distinctive capability is rooted in a solid-solid phase transformation between martensite and austenite, imparting the alloy with unique and programmable mechanical properties. The austenitic phase is characterized by a body-centered cubic structure, with a Nickel atom in the center and Titanium atoms around it, while the lattice structure of martensite is monoclinic and consists of a rhombic alignment with an atom in each of the rhombic corners. This phase transformation is a shear-dominant diffusionless solid-state

process, involving the nucleation and growth of the martensitic phase from the parent austenitic phase. Consequently, when an SMA alloy undergoes a phase transformation, it goes from the high-symmetry, cubic austenitic phase to the low-symmetry martensitic phase [2]. A diffusionless transformation manifests as an instantaneous distortion in the crystal lattice, contrasting with the diffusion transformations, common in steel alloys, which require the diffusion of atoms over extended distances, necessitating prolonged exposure to high temperatures. The term "shear-dominant" implies that the transformation of a unit cell element induces both volumetric and shear strains along clearly defined planes, originating from a shift in the thermodynamic stability of the system. In contrast to the irreversible dislocation motion witnessed in the martensitic transformation of steel alloys, twinning in Nitinol is a reversible process.

Critical transformation temperatures include A_s (austenite start) and A_f (austenite finish) marking the beginning and end of the transformation from martensite to austenite phase, and M_s (martensite start) and M_f (martensite finish) indicating the start and end of the austenite to martensite transformation. The maximum temperature at which superelasticity can appear is the martensite deformation temperature M_d. Beginning at M_s, the martensitic phase transformation unfolds as the temperature drops until M_f. The reverse transformation (martensite to austenite) can then occur at temperature A_s and continues until A_f is reached ($A_f > A_s$), signifying the material's return to fully austenitic state [2].

The alloy's composition and preceding processes play a primary role in influencing transformation temperatures, for example, alteration in these temperatures can result from microstructural defects, precipitates, and grain size. An exothermic phase transformation occurs during the direct transformation from austenite to martensite ($A \rightarrow M$), releasing heat due to a change in enthalpy. In contrast, the reverse transformation from martensite to austenite ($M \rightarrow A$) is characterized by heat absorption, making it an endothermic phase transformation. The measured amount of heat exchanged is proportionate to the volume fraction of the transformed material, enabling differential scanning calorimeters (DSC) to determine transformation temperatures.

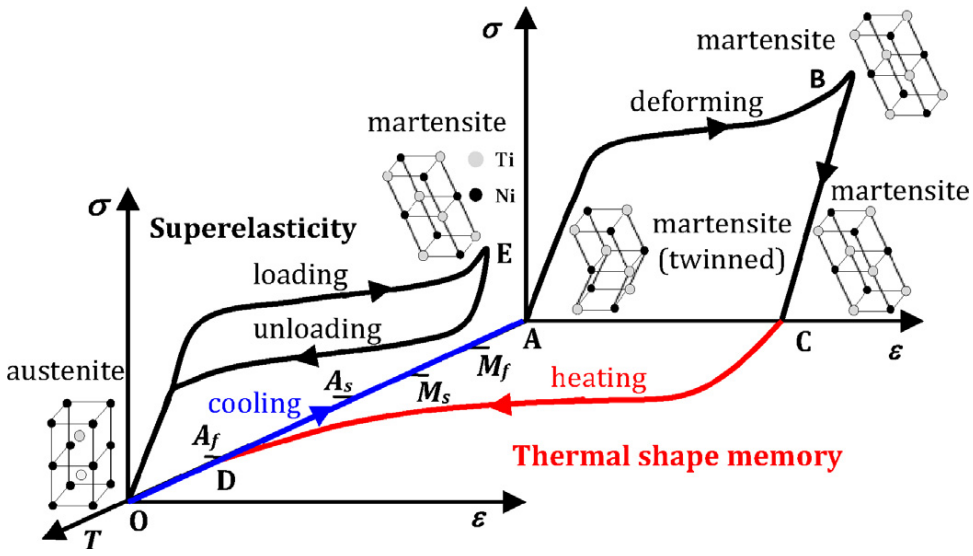

Figure 1.1 Stress-strain-temperature diagram of Nitinol [2].

Figure 1.1 illustrates the thermal shape memory process exhibited by Nitinol. Assuming Nitinol starts in an austenitic state at the origin point O, the cooling along path O to A, below the M_f, triggers a transformation from austenite to twinned martensite. An inelastic deformation occurs along trajectory A to B leading to the reorientation and detwinning of martensite. Subsequent load release along path B to C results in the elastic unloading of the reoriented detwinned martensite, locking the material in its deformed state. Upon heating above A_f the material transforms from martensite to austenite, recovering the pseudoplastic deformation and "remembering" its original shape.

Alternatively, Nitinol in its austenitic form can be loaded along the path O to E (see Figure 1.1) above $A_f$through stress-induced transformation to the martensitic state. This process facilitates a substantial elastic strain, reaching up to 11%. Unloading along the path E to O brings the material to revert to its austenitic state, recovering the superelastic deformation and exhibiting a hysteresis loop in the stress–strain diagram. Despite the remarkable features of shape memory and superelasticity effects, coupled with high flexibility and strong strain hardening, the machining of Nitinol is challenging and causes, for example, short tool life and the formation of burrs [3]. The difficulty in machining arises not only from the unconventional stress-strain curve but also from the low thermal conductivity and a low elastic modulus of NiTi alloys.

1.1.3 Common Applications

In addition to shape memory and superelasticity, NiTi exhibits other favorable characteristics that contribute to its desirability, particularly in fields such as aerospace and biomedical engineering but also in automobile construction, household appliances, and other fields of science and technology, such as temperature sensors, thermo-power actuators, thermomechanical connectors and other. Among these, as it is a Ni-based alloy, it displays resistance to elevated temperature. From this point on, the focus will be on common applications in the biomedical field, since NiTi has found extensive use in applications ranging from bone plates and screws to stents. The alloy possesses low stiffness, making it suitable for applications where flexibility and compliance with the natural movement of the body are essential. The damping characteristics of NiTi are notable, making it effective in absorbing and dissipating energy, which is beneficial in situations where controlled and gradual movements are required. Moreover, the corrosion-resistant nature of NiTi enhances its longevity and reliability in various environments [4].

The success of biomaterials hinges on two crucial factors: biomechanical performance, ensuring adequate mechanical strength, and biochemical compatibility, which involves non-toxicity or non-carcinogenicity. Biocompatibility, in this context, refers to a biomaterial's ability to fulfill its intended function in medical therapy without causing any undesirable effects on the recipients. The International Organization for Standardization (ISO) 10993 sets the standard for the biological evaluation of medical devices and dental materials and, given the known potential for metals to induce intricate biological reactions, it becomes imperative to address the biocompatibility and cytotoxicity concerns associated with Ni-Ti alloy in biomedical applications [4]. While Titanium itself is a biocompatible element, Nickel could lead to local and systemic toxicity, carcinogenic effects, and immune responses. In NiTi, Nickel is chemically bonded to Titanium through a strong intermetallic bond, minimizing the risk of reactions even in patients with Nickel sensitivity. Typically, NiTi devices are equipped with an external protective layer of Ti-based oxide, which not only enhances the corrosion resistance of this material but also acts as an efficient barrier to prevent the diffusion or release of nickel ions. Es-Souni et al. conducted in vitro cytotoxicity tests, revealing that the biocompatibility of NiTi alloys is generally positive, although it varies depending on cell types, material processing, and test conditions [5]. The utilization of the shape memory effect and superelasticity allows for the activation of medical devices either through the natural warmth of the body or external heat sources. Such designs are not achievable with conventional alloys, for example, stainless steel, as can be seen in Table 1.1.

An advantageous characteristic of NiTi implants is their ability to undergo shape changes post-implantation. This capability is exploited by activating the shape memory effect of the material through the natural temperature of the body. These alterations in shape provide two primary benefits: (i) enhanced bone fixation and (ii) reduction of the invasiveness associated with surgical procedures [5].

Ti-rich Nitinol, a room-temperature martensitic NiTi with a higher concentration of titanium compared to standard compositions, is mostly used in orthodontics, drug delivery systems, self-expanding stents, implant devices, atrial occlusion devices, and ophthalmology. Ni-rich Nitinol is austenitic at room temperature, so it exhibits superelasticity and imparts bone-like behavior in implants such as fracture fixation, orthotic, and rehabilitation devices.

Property	**NiTi**	**Stainless steel**
Recovered Elongation	8%	0.8%
Biocompatibility	Excellent	Fair
Effective modulus	Approx. 48 (GPa)	193 (GPa)
Torqueability	Excellent	Poor
Density	6.45 (g/cm^3)	8.03 (g/cm^3)
Ultimate tensile strength (UTS)	Approx. 1240 (MPa)	Approx. 760 (MPa)
Coefficient of Thermal Expansion (CTE)	Martensite – 6.6 x 10^{-6} (cm/cm/°C) Austenite – 11.0 x 10^{-6} (cm/cm/°C)	17.3 x 10^{-6} (cm/cm/°C)
Resistivity	80–100 (μΩ cm)	72 (μΩ cm)

Table 1.1 Physical and mechanical properties of NiTi vs. stainless steel [5].

Figure 1.2 shows two examples of NiTi applications in biomedical implants, with shape memory and superelasticity properties respectively.

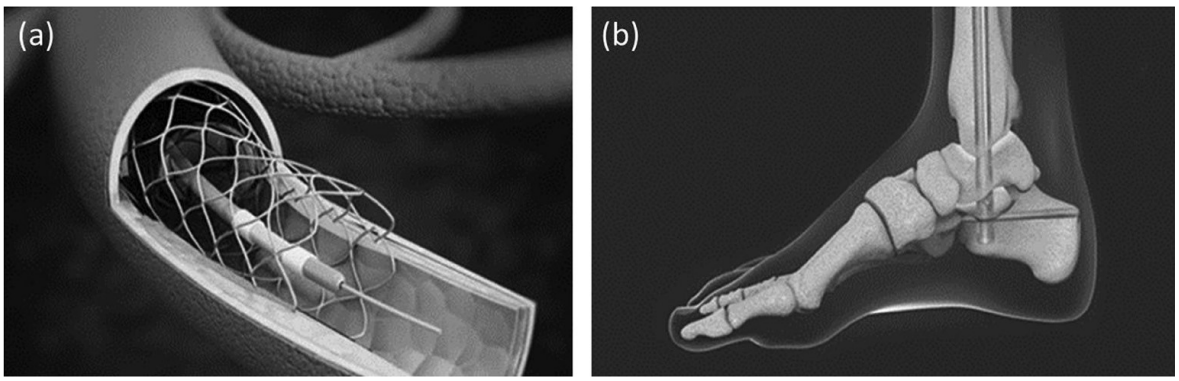

Figure 1.2 Two examples of NiTi common application in the biomedical field; (a) Stent (b) Fracture fixation device [6].

Since this thesis focuses on room-temperature austenitic Nitinol, the subsequent examination will address devices that primarily exploit the SE property of this smart material. In the broad field of biomedical applications, the use of smart materials such as NiTi is particularly important for the two biomedical fields of assistive and rehabilitation devices.

A prosthesis is an artificial substitute or replacement for a part of the body, allowing individuals to carry out their daily activities in a normal manner. The main problem with assistive devices lies in their actuation systems and research has found solutions by utilizing SMAs, creating NiTi wires that could exert relatively high forces, resulting in lightweight devices compared to old pneumatic, hydraulic, and electric actuators [7]. A Nitinol disc device's patent, specifically a scoliosis plate, has been registered and published by the United States Patent Application Publication. It comprises a lower section and an upper section. The upper section is curved in the sagittal plane and induces a forward bending of the user's spine due to the pressure exerted by the plate. A 2018 study conducted a comparative analysis between the use of superelastic nickel-titanium alloy rods (SNT) and conventional titanium alloy rods (CTA) in the surgical treatment of adolescent idiopathic scoliosis (AIS) [8]. The primary objective was to assess the efficacy of the rods in achieving the correction of coronal deformities. Secondary objectives included evaluating correction in sagittal deformities, assessing coronal balance, and measuring patient-perceived outcomes. The study revealed that the overall change in 'Fulcrum Bending Correction Index' (FBCI) was more favorable for the SNT group, showing a steady increase up to at least 1 month and extending up to 6 months postoperatively when compared to the CTA group.

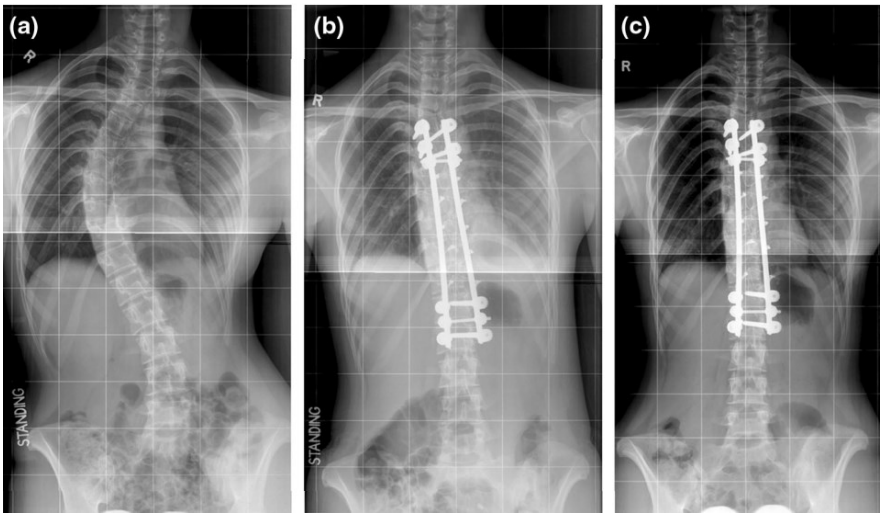

Figure 1.3 SNT rod's radiography. (a) preoperative (b) postoperative at 1 week (c) postoperative at 4 weeks [8].

Karnes et al. developed and filed a patent for an arthrodesis device capable of generating and applying compression within joints. Arthrodesis is the artificial induction of joint ossification between two bones by surgery and is performed to relieve pain in a joint that cannot be managed with pain-relieving drugs, splints, or other normally indicated treatments. The device can bring the bones near each other producing a compressive load for an extended period, until healing [7].

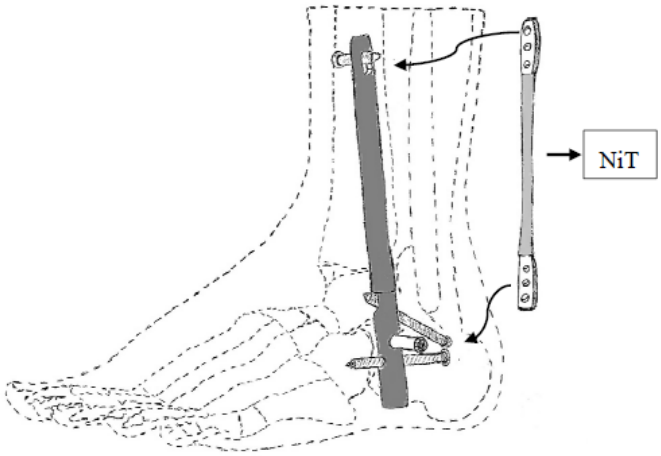

Figure 1.4 Artrodesis device developed by Kernes et al [7].

1.2 Nitinol Manufacturing

1.2.1 Conventional Manufacturing

Unlike many of the traditional materials, there is no single fabrication scheme for manufacturing NiTi devices. The casting technique is one of the common conventional methods for producing NiTi. However, this method involves high temperature melting procedures that lead to an increased impurity level, including carbon and oxygen. Consequently, Ti-rich phases like TiC and $Ti_4Ni_2O_X$ are formed, compromising the functional properties of NiTi due to the creation of these secondary phases. Another challenge associated with casting is the difficulty of machining procedures for these super-ductile alloys, resulting in excessive tool wear as machining is employed to shape the final products. Powder metallurgy (PM) is another conventional technique that is used for producing near-net-shape devices and requires powder preparation. Despite its advantages, such as achieving an almost net shape, this method has one major disadvantage: the large surface area of the powder particles leads to a high collection of impurities. Furthermore, conventional techniques such as casting, and powder metallurgy have the limitation of not being able to manufacture finished parts with complex geometry and it's not possible to control the size and the shape of the porosity when required [9]. The NiTi produced using conventional method will be also denoted as 'wrought' NiTi in this context.

1.2.2 Additive Manufacturing

Over the last ten years, there has been a notable rise in interest in Additive Manufacturing (AM) as a viable process to fabricate NiTi, primarily due to its ability to overcome numerous challenges inherent in conventional methods, explained in § 1.2.1. These innovative processes start from CAD data and involve the stepwise addition of material in successive layers, typically composed of powders and melted using a laser. Two predominant AM techniques for NiTi include powder-bed-based technologies like Selective Laser Melting (SLM) and flow-based methods such as Laser Engineered Net Shaping (LENS) [9]. A powder-bed technique begins by slicing the CAD model, and proceeds through powder deposition with a coater, as shown in Figure 1.5. The final product is ready once the supports and loose powders have been removed. Conversely, flow-based technologies involve the deposition of powder through one or more nozzles that feed the powder directly into the laser focus [10]. These AM approaches offer a promising alternative, avoiding the limitations associated with traditional methods and

exploiting the advantages of layer-by-layer processes. Notably, powder-bed-based technologies are more widely employed to create intricate and complex parts.

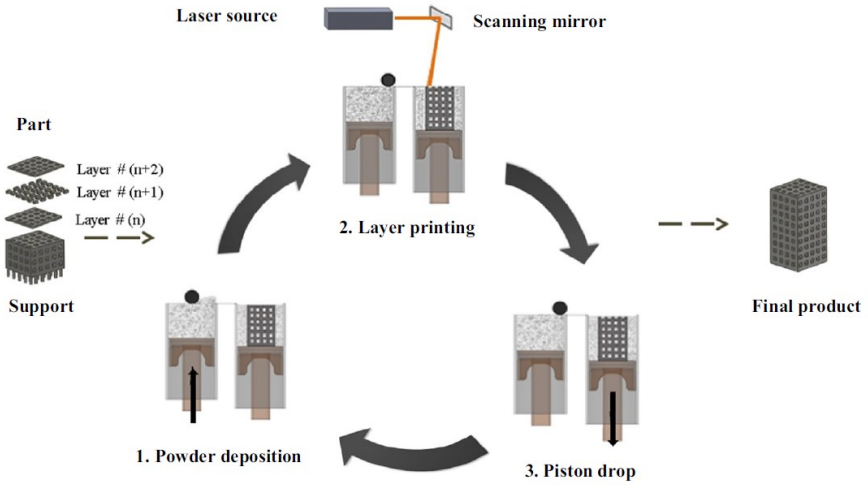

Figure 1.5 The operational sequence of powder-bed-based machines [9].

The initial step in AM processing involves preparing NiTi powder. The ratio of Ni and Ti elements is crucial in guaranteeing these properties in the final part. Parts crafted from a Ti-rich powder exhibit the shape memory effect, while those from a Ni-rich powder showcase superelastic behavior, after subsequent solution annealing and aging. Apart from the Ni/Ti ratio, the powder preparation procedure significantly influences the features of the end products. Powders can be generated through either pre-alloying or elemental blending of Ni and Ti particles. Processing from elementally blended powders results in the formation of intermetallic phases, pure nickel, and pure titanium in the fabricated parts. It's worth noting that the method of powder preparation, including mechanical attrition, water atomization, and gas atomization, is critical as it affects the final particle size, particle distribution, and impurity content of the resultant powders. The Electrode Inert Gas Atomization (EIGA) procedure is more favorable, producing more accurate particles and maintaining an acceptable level of impurity contents. The second essential step for additive manufacturing is the setting of optimal parameters to make the material reach the highest level of density and the lowest contamination content. These process parameters are described by the following equation, according to Meier and Haberland [9] :

$$E = \frac{P}{v \cdot h \cdot t} \tag{1.1}$$

The energy density input (J/mm^3) E is a combination of various processing parameters: P for laser power (W), v for scanning velocity (mm/s), h for hatch spacing (mm), and t for layer thickness (mm). There's a third requisite to minimize the oxidation and the impurity level,

which is given providing an inert atmosphere all along the process. The aim is to align the behavior of NiTi produced through AM more closely with that of wrought NiTi. This is crucial because generally the precision and the surface finish attained through the only additive process tend to be lower compared to conventional techniques [5]. Nevertheless, the accuracy and surface finish can be significantly impacted by operational parameters and the size of the powder particles. The aspect for which it is most important to implement AM is the possibility of creating patient-specific implants with customized stiffness. Materials characterized by low thermal conductivity contribute to improved accuracy, as they enable better control over the melting bath and solidification processes. Minimizing heat conduction not only enhances controllability but also minimizes grain growth, thereby enhancing the overall accuracy and surface finish in powder-based AM processes.

1.2.3 Thesis's Process Chain

This study would like to stand in continuity with the work of Bertolini et al., which has investigated the feasibility of a process chain – outlined in Figure 1.6 – including AM, through Laser Powder Bed Fusion (LPBF), followed by heat treatment and finish machining, to produce Nitinol components with improved surface integrity and more favorable superelastic characteristics. It was the first study proving a correlation between the process chain parameters and NiTi's superelastic property, with a focus on the microstructural analysis and surface integrity of the workpiece, varying the cooling condition during finishing machining [11]. This thesis aims to investigate the tool-wear behavior in the machining of superelastic Nitinol components produced through the previously proposed manufacturing approach and to bring proof of their applicability in the biomedical field.

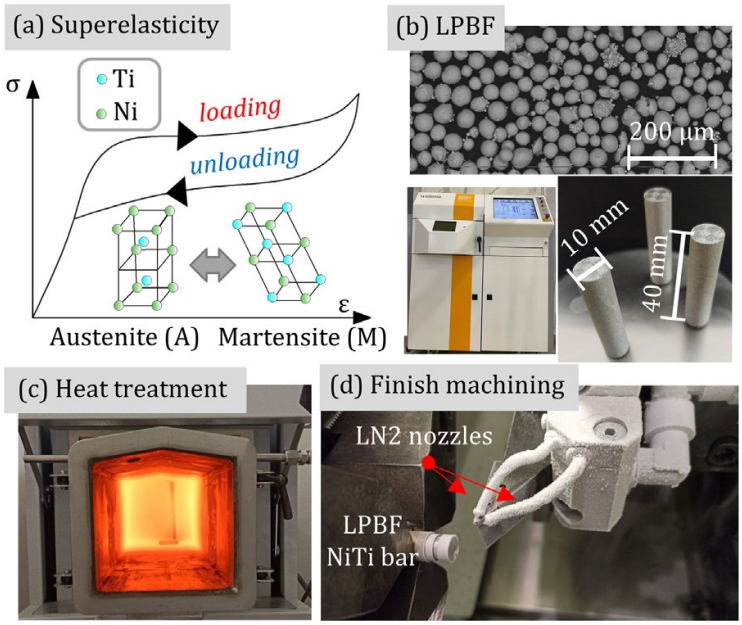

Figure 1.6 NiTi SE (a); process chain: LPBF (b), heat treatment (c), finishing machining (d) [11].

The process parameters used for LPBF outlined in Table 1.2 were previously optimized in a prior study [12]. The objective was to attain the highest density and promote the formation of the austenitic crystal structure at room temperature since Ni-rich powders were used. This specific crystal phase is crucial for imparting superelasticity to NiTi.

Power [W]	Scanning speed [mm/s]	Hatch distance [mm]	Layer thickness [mm]	Input energy density [J/mm^3]
70	1100	0.06	0.025	42.42

Table 1.2 LPBF parameters implemented.[12].

Once the cylinders were printed, some heat treatments were carried out, so the samples were: as manufactured (AB), aged at 300°C (T3), and aged at 600°C (T6). In all three cases, a fully austenitic crystalline structure was achieved, providing superelasticity properties to samples. Finishing work was then carried out, using the cutting parameters suitable for the difficult-to-machine alloys recommended by the manufacturers of the tools used (depth of cut 0.25 mm, cutting speed 62 m/min, and feed 0.07 mm/rev) [11]. The results consist of a comparison of the different heat treatments and the two different lubri-cooling strategies employed, namely flood and cryogenic cooling. The main achievements of Bertolini's study include:

(i) Heat treatment after AM triggers the formation of precipitate that influences the superelastic behavior of NiTi, particularly T6 increasing the work recovery ratio, calculated as the ratio between the recoverable deformation energy and the total one.

(ii) Machining improves the surface integrity in the case of cryogenic machining.

(iii) The wear test results indicated that employing T6 treatment following AM in conjunction with cryogenic machining guarantees minimal wear volume, thereby providing superior wear resistance.

1.3 Nitinol Machinability

The machining of NiTi alloy faces various challenges due to issues such as considerable tool wear, high cutting force, extensive hardness, and the occurrence of surface defects. Concerning the latter, there is a variety of surface defects produced by machining processes, including feed marks, surface drag, tearing, material cracking, surface cavities, adhered material particles, chip layer formation, deformed grains, slip zones, laps (material folded onto the surface), and lay patterns [13]. Figure 1.7 shows some examples of surface defects that affect NiTi.

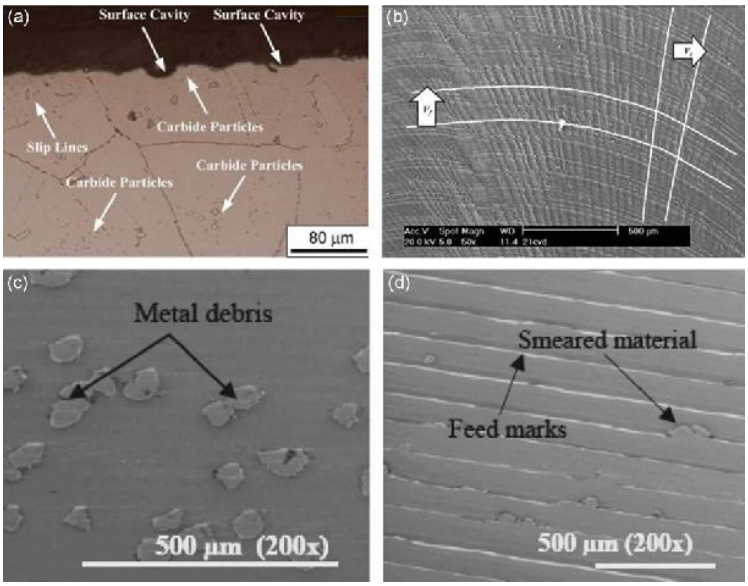

Figure 1.7 Surface Damages in Machining of Nickel-Titanium Alloys: (a) Metallographic Microstructure after Turning Process (b) Lay Pattern after Dry Milling Process (c) Metal Debris after Turning Process, and (d) Smeared Material and Feed Marks after Turning Process [13].

An aspect requiring consideration in material cutting processes is the existence and origin of residual stresses either on the surface or inside the material. Residual stresses are generated during the machining processes of nickel-titanium when the workpiece material undergoes

thermo-mechanical loads that cannot be fully recovered. Conversely, residual stress refers to the stresses that persist in the material after the applied load is removed. Tool wear is a critical factor influencing residual stresses in machined surfaces. On the one hand, tool wear can be influenced by pre-existing residual stresses in the material. On the other hand, the cutting process itself can generate new residual stresses due to the applied forces and plastic deformation of the material. Residual stress poses a potential risk for propagation, crack initiation, and fatigue failure. Hence, it is crucial to either eliminate or prevent its occurrence during machining processes [13]. As tools wear, changes in thermomechanical loads occur, leading to shifts in residual stress states. Initially, mechanical rubbing dominates, inducing compressive stresses. However, with prolonged tool wear, thermal effects become more influential, promoting tensile stresses. The evolution of tool wear under various cutting parameters amplifies differences in residual stress distributions, emphasizing the importance of understanding the interplay between thermal and mechanical effects. Notably, regardless of cutting speeds and feed rates, the use of worn tools leads to deeper penetration of residual stresses beneath the machined surface [14]. Tensile plastic deformation is induced by cutting parameters and tool conditions, influencing the workpiece material in terms of surface integrity.

1.3.1 Tool Wear

According to International Standard [15] tool wear is defined as “the change of the tool from its original shape, during cutting, resulting from the gradual loss of tool material or deformation”. Tool wear results from a combination of factors depending on the type of the tool and the workpiece, for instance the properties of the different tool materials employed, which must be appropriate to the work material in terms of chemical affinity. However, in the case of NiTi machining, it is also influenced by additional factors related to the type of machined alloy, such as phase transformation, superelasticity, microstructural purity, low elastic modulus, and limited ductility. Tool wear is therefore an indicator of the difficult machinability of Nitinol.

Different types of wear can be observed on the tool during machining processes, specifically on its rake face and flank face. The Figure 1.8 shows a section of both tool faces where tool wear occurs. According to ISO 3685, tool wear can be classified in three main classes: the wear of the major flank, including flank wear and notch wear, the wear of the minor flank, and the wear of the rake face [15].

The flank wear occurs gradually on the side of the cutting tool because of its rubbing against the workpiece material as it removes material during the cutting operation. As the cutting tool

wears, the flank wear can manifest as a gradual increase in the width of the worn area on the tool's flank. This wear can eventually lead to a reduction in tool performance, affecting the surface finish of the machined part and the dimensional accuracy of the cut. Monitoring and controlling flank wear are essential aspects of machining operation to ensure the efficiency and effectiveness of the cutting tool. Proper machining parameters can help to minimize the flank wear and extend the tool life.

Notch wear is a distinct form of wear that combines both flank and face wear, manifesting in the region adjacent to, but beyond, the point where the major cutting edge intersects with the work surface. Under specific conditions, notch wear may necessitate a tool change. The profile and length of the notch wear largely hinge on the precision of depth of cut settings. Due to these considerations, the assessment of the width of the flank wear land excludes notch wear from its evaluation.

Minor flank wear refers to wear occurring on the minor flank surface of the cutting tool. During finish turning with small feeds, it is common to observe one or more grooves on the minor flank after a period of cutting. These grooves contribute to an increased roughness of the machined surface, making a direct evaluation of this type of tool wear challenging. However, its impact can be assessed by measuring the roughness of the machined surface. Establishing a specific roughness value can act as a tool life criterion for finish turning. The oxidation of the minor flank is a concern, particularly when turning with carbide tools at elevated temperatures resulting from high feeds and cutting speeds. In such instances, the tool may become ineffective before reaching the initially chosen criteria. Therefore, the condition of the minor flank becomes a crucial tool-life criterion. This deterioration often occurs abruptly; otherwise, a predefined level of deterioration must be adopted as a criterion.

In the case of wear on tool rake face, it is most commonly referred to crater wear. Crater depth, named as KT, is a valid measure of tool wear and a predetermined KT value can be chosen as a criterion for tool life. The crater depth is the maximum distance between the crater bottom and the original face. Notably, crater wear holds greater significance for carbide tools compared to other types. The positioning of the crater relating to the cutting edge also carries significance: a deep and wide crater situated farther from the cutting edge may pose less risk to the tool compared to a less profound, narrow crater near the cutting edge. Additionally, the distance from the front edge of the crater to the major cutting edge proves to be a useful criterion because establishing a limit on this distance can mitigate the risk of catastrophic failure [15].

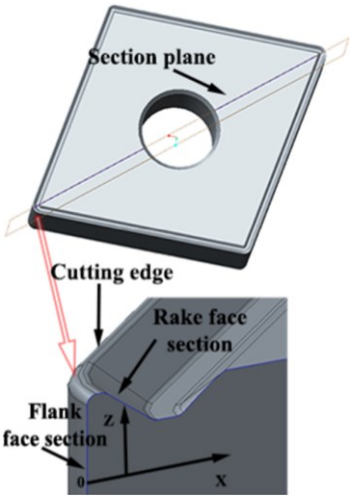

Figure 1.8 Flank and rake face section of a generic tool [16].

1.3.2 State Of The Art Of Tool Wear After NiTi Machining

To date, studies have been carried out on tool wear from finishing machining operations on NiTi wrought components, but never on NiTi AM components. This thesis work aims to make a study of tool wear during the turning of NiTi AM samples, as well as of wrought NiTi to investigate the effects of tool wear not only with respect to different cutting parameters, but also to different manufacturing techniques of this peculiar material. Studying the tool wear of a difficult-to-machine alloy aims to overcome the challenges associated with machining this unique alloy, which has limited its adoption in the orthopedic industry. This industry heavily relies on turning and milling operations to produce macro-scale products. Researchers have previously noted that specific cutting parameters during the machining of wrought NiTi alloy considerably influence the control of tool wear. Furthermore, they reported that uncoated carbide tools are not suitable for machining NiTi alloys and recommended the use of multi-layer coated cemented carbide tools to reduce tool wear, thus enhancing machining performance in the turning process of NiTi alloy. The mechanical behavior of NiTi alloys, temperature-dependence, and processing conditions (cooling, lubrication, etc.) must be considered to determine their potential contribution to improving the workability of these alloys. Moreover, the effects of wrought fabrication, i.e., melting techniques and heat treatments on tool performance were evaluated on austenitic NiTi alloys at room temperature [17]. To assess the machining-induced product performance, the surface quality and topography of the machined surfaces were considered.

Kaynak et al. considered three different manufacturing modalities for a room-temperature austenitic NiTi (50.8 at % Ni) which causes differences in morphology of inclusion and elastic moduli and therefore also influences the tool wear pattern. Additionally, two prior heat treatments were investigated: cold working and hot rolling followed by full annealing. The experimental set-up involved the use of a DCGT11T308HP-grade KC5410 tool coated by TiB_2, on a machine implementing CNC turning, using constant cutting parameters, and evaluating the differences in the use of three different lubrication conditions (i.e., dry, cryogenic, and minimum quantity lubrication (MQL)). Tool wear was assessed by measuring the length of the wear land in the nose region, so the parameter of interest was VB_{Cmax}, which was measured after each minute of machining, using an optical microscope, and surface roughness was also assessed in terms of the Ra parameter, calculated by averaging over five different measurements using the optical profiler. The findings involve considerations for both the alloy type and machining conditions. Machinability of not-treated samples was worse than fully annealed ones. Additionally, it was noted that tool life experiences a substantial decrease in samples containing TiC inclusions, indicating enhanced machinability of Nitinol when there is no carbon addition to the alloy. Regarding machining considerations, concerning the role of different lubricants, it has been demonstrated that the use of cryogenic technology is a promising technique as it significantly reduces tool wear. In terms of surface roughness, as tool wear increases over time, the surface roughness of wrought NiTi worsens. For short machining durations, around 1 minute, cryogenic lubrication proves to provide better surface roughness. However, after 4 minutes, the surface roughness levels of all three lubrication modes become equivalent [17].

Another previous study by the same author examined the challenges of Nitinol processing in terms of high tool wear, comparing the effects of different lubrication conditions and the impact of using various cutting parameters, particularly by varying the cutting speed. Several types of wear, cutting force components, and the surface quality of machined parts were investigated in this study [18]. A NiTi alloy, composed of 49.9% nickel and 50.1% titanium, underwent a cold working process. Differential Scanning Calorimetry (DSC) analysis indicated that the alloy exhibited a room-temperature martensitic phase, displaying a microstructure characterized by dynamic recrystallization and an equiaxial grain arrangement. The same type of tool as the previously mentioned study was used; a CNC lathe was employed for turning. The cutting parameters used were constant feed (f) and depth of cut (a_p), with variable cutting speed. This was done to investigate the effects of cutting speeds on tool wear. To assess the effects of the type of cutting fluid as well, progressive tool wear tests were conducted at a constant speed.

The VB measurement was carried out under an optical microscope, cutting forces were measured with a piezoelectric dynamometer, surface roughness was evaluated using a profiler, and cutting temperature was monitored using a thermocouple and an infrared camera. Regarding the effects of cutting speed on tool wear, the most common types of wear were identified: notch wear, nose wear (flank wear in the region of the tooltip), and crater wear on the tool face. The experimental results revealed that cutting speeds above 25 m/min led to higher wear rates, but the cryogenic lubricant tends to mitigate this tendency. On the other hand, concerning the results of using different types of lubricants, at a constant speed of 25 m/min, it was observed that when using cryogenic lubricant, wear occurs at a slower rate compared to other cases.

Many studies have also shown the effect on tool wear of different types of tools themselves. Jawahir et al. [19] highlighted that when utilizing grooved tools in machining, flank wear doesn't always play the most dominant role in tool failure or the end of tool life. Their findings indicated that in many cases, grooved tools fail long before significant flank wear reaches the failure criterion. Concerning the work material, a common issue in machining particularly nickel-based alloys, is the formation of a V-shaped notch wear at the depth-of-cut line; they demonstrate that cryogenic cooling presents a viable option to minimize the notch wear rate in the machining of NiTi SMAs.

Previous research by Weinert et al. in machining NiTi-based shape memory alloys also indicated extremely high-notch wear, and adjusting cutting speed and feed rate did not effectively mitigate tool wear [18]. Another observed tool wear or failure mode was chip flow damage, which significantly contributes to accelerated notch wear development. Under dry and Minimum Quantity Lubrication (MQL) conditions, fractures on the main cutting edge were observed due to inappropriate chip flow. Improper chip flow, combined with notch wear in the cutting tool, makes it challenging to maintain clear boundaries between notch wear and chip flow damage. Despite noticeable chip flow damage within the initial 5 minutes of dry cutting, the depth of chip flow damage did not show significant progression with cutting time. Instead, the damage spread along the main cutting edge of the tool with increasing cutting time.

As regards dry cutting, there were instances of multiple tool wear and fractures, embracing severe chipping, abrasive wear affecting the flank face of the cutting tool, and fractures on the rake face. In the case of MQL machining, observable issues included notching, chip-tool welding (where chip debris adheres to the main cutting edge), and evident abrasive wear. The level of abrasive wear observed in cryogenic machining was the most minimal when compared

to the other two cutting conditions and there were no occurrences of chip-tool welding observed after cryogenic machining.

1.3.3 Effect Of Tool Wear On Superelasticity

Since one of the most functional properties of NiTi is the superelasticity, it's important to investigate the effect of the tool wear on this feature. The super-elastic recovery of the workpiece leads to a decline in machinability, manifested by reduced dimensional accuracy, heightened cutting resistance, and a shortened tool life. When NiTi is heated above martensitic transition temperature (M_d) it loses its superelasticity and undergoes a plastic deformation that follows an elastic deformation, as observed in most metallic materials [14].

There are still many studies to be done to understand how to improve the machinability of NiTi alloys. Most of the studies in the literature that see preheating of the workpiece as the solution to improve machining performance, do not consider M_d temperature and its effects on the SE property. Yang et al. conducted an experiment on room-temperature austenitic NiTi machined with different cutting speeds and with the presence or absence of preheating. The preheating temperature was established at 175°C to keep the workpiece above the martensite desist temperature and preventing the formation of an excessive oxide layer [14]. The workpiece temperature during machining was monitored using a thermal camera. It was observed that the untreated workpiece never exceeded M_d in any of the tests, regardless of the cutting speed. This suggests that the workpiece can undergo superelastic deformations through the phase transition. Conversely, in the case of the preheated workpiece, the temperature consistently surpassed the M_d temperature during machining at all cutting speeds. Therefore, it is reasonable to expect that under these conditions, the effect of superelasticity is eliminated. In general, the values of the M_d in NiTi alloys vary with phase transformation temperatures, primarily influenced by the nickel content and the type of heat treatment. Consequently, a room-temperature martensitic NiTi alloy with higher phase transformation temperatures exhibits a superior M_d value compared to a room-temperature austenitic NiTi alloy. The workpiece's shape recovery, representative of its superelastic deformation, was assessed by calculating the recovery radius (R) during machining at various speeds. The results revealed a higher recovery without preheating compared to preheating. However, at Vc = 10 m/min (minimum speed) in both conditions, the maximum R was observed. Surface topography analysis showed significant built-up edge (BUE) formation at Vc = 10 m/min without preheating, reduced but still present with preheating. Measurement of the maximum height of the surface profile (Rz) indicated

higher values after machining at Vc = 10 m/min in both conditions, indicating a rougher surface. Superelastic deformation was analyzed through XRD measurements. The austenitic phase was detected in the as-received condition, but after machining without preheating, a phase change was observed with some martensite undergoing a reverse transformation, contributing to the pronounced superelastic recovery. With preheating, the recovery was limited, indicating better preservation of the initial state of the workpiece. Additionally, BUE deposition was reduced by increasing the cutting speed, improving the surface finish. Lastly, the workpiece temperature proved to be a key factor influencing superelastic recovery. XRD analysis confirmed that the higher temperature during machining at higher speeds favored a greater reverse phase transformation, contributing to the superelastic recovery.

Tool wear reflects the impact of the superelastic recovery of the workpiece in machining the NiTi alloy. Initial wear increases with cutting speed without preheating but is limited with preheating. Tool life decreases with higher cutting speed without preheating, but under preheating, there is an increase of 20%, 43%, and 100% at 25, 50, and 100 m/min. Without preheating, there are craters, adhesions, and regular wear; with preheating, wear is similar but without craters at 50 m/min. At 100 m/min without preheating, cutting edge fracture occurs, while with preheating, the tool withstands, thanks to reduced friction. The superelasticity of the workpiece reduces tool life, but preheating extends tool life, suggesting that a moderate cutting speed of 25-50 m/min is optimal. [17,18].

CHAPTER 2

2. EXPERIMENTAL PROCEDURE

2.1 Materials

2.1.1 Conventional Manufactured NiTi

The conventional or wrought manufactured parts were obtained from the Institute for Sustainable Manufacturing (ISM) at the University of Kentucky by Professor Jawahir, who used these same workpieces for his studies on NiTi tool wear. The chemical composition given in the research of Jawahir et al. is 50.8 at% Ni, and 49.2 at% Ti [17]. Specifically, four cylindrical bars were supplied with varying diameters and equal lengths (77 mm), see Figure 2.1.

Figure 2.1 One of wrought NiTi bars (left); AM NiTi bars (right)

2.1.2 Additive Manufactured NiTi

The additive manufactured parts were produced, in the form of two bars, each 15 mm in diameter and 40 mm in height (see Figure 2.1), using the LPBF technique with the SISMA MYSINT^{TM}100 machine in the Te.Si. laboratory at the University of Padova. This procedure, initially guided by a three-dimensional model derived from Computer-Aided Design (CAD), stands out for its accuracy and the complexity of the geometries it can achieve. After the design phase, the CAD model is sliced into thin layers, each consisting of horizontal slice. A metal powder bed acts as a substrate for the construction process. A titanium building platform evenly

disperses and compresses a layer of powder. The core of the process lies in the high-powered laser beam: the laser selectively melts powder particles into specific areas following the CAD model. The process parameters used for LPBF are shown in Table 1.2. The outcome is the formation of a solid layer, whose bond to the underlying substrate serves as the foundation for the subsequent layer. The cycle of compression, laser melting, and solidification iterates until the entire object takes shape, layer by layer. The subsequent cooling process can induce residual stresses that are often the cause of deformation in the component after printing. It is therefore essential that heat is properly dissipated. Upon completion of the printing, the resultant part is enveloped in residual powder and may undergo finishing operations, such as heat treatments, to impart desired characteristics. The powder composition was 50.8 at% Ni, and 49.2 at% Ti.

2.1.2.1 Heat Treatment

In Bertolini et al. study some cylinders were heat treated, with a solution treatment, and an aging treatment. Two different aging treatments have been chosen and compared: at 300 °C (T3) and 600 °C (T6). The results showed that the T6 treatment lowers the pre-machining temperature A_f more, raises the ratio strength vs. indentation depth, and raises the work recovery ratio and Martens hardness, compared to T3. Hence, the T6 emphasizes the superelastic behavior of NiTi, inducing precipitation of Ni-rich precipitates with a needle shape, which possesses less coherence with the matrix and reduces the deformation field associated with the difference between the lattice parameters of the precipitates and the matrix [11]. Furthermore, it is recognized that surface treatments are useful in enhancing the biocompatibility of the alloy [5].

In this thesis work, following the printing of the pieces, a T6 heat treatment was performed. A Carbolite Gero^{TM} CWF 1200 (see Figure 2.2) furnace has been used to carry out both the solution treatment and aging. The parameters of the two treatments are in the Table 2.1.

	Treatment temperature (°C)	**Treatment duration (min)**	**Inert atmosphere**	**Cooling system**
Solution treatment	1060	60	Yes (with Argon)	Water
Aging	600	180	No	Air

Table 2.1 Heat treatment parameters.

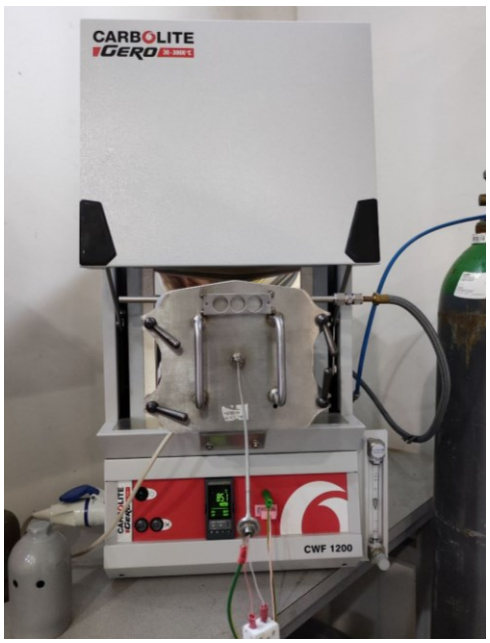

Figure 2.2 Carbolite GeroTM CWF 1200 furnace.

2.2 Characterization Before Machining

2.2.1 DSC Analysis

Differential scanning calorimetry (DSC) is a technique used to study the thermal transitions of materials, namely the temperature and heat flow associated with material transitions as a function of time and temperature. It supplies both quantitative and qualitative data on the heat-absorbing (endothermic) and heat-releasing (exothermic) processes of materials during physical transitions resulting from phase changes, melting, oxidation, and other heat-related alterations [20].

In the case of NiTi, DSC studies the alloy solid-solid transformation, providing information on the transformation temperatures. The difference in heat between the test sample and a reference is measured, while both are subjected to a controlled temperature ramp. The heat is supplied to the sample and the reference through a heating platform so that the reference temperature increases at a constant speed. The difference between the heat flows of the sample and the reference is proportional to their temperature difference which is measured by the thermocouples placed below the samples. The heat flow is influenced by changes in temperature and is governed by an analogy to Ohm's law in the thermal domain:

$$q = \frac{\Delta T}{R} \tag{2.1}$$

Where q is the sample heat flow, ΔT is the temperature difference between the sample and reference, and R is the thermal resistance of the thermoelectric disc. If a phase transition occurs in the sample, its temperature remains constant during the transition, allowing for the identification and analysis of such transitions. The change in the energy required to match the sample's temperature with the reference indicates the extra heat absorbed or released by the sample. In an endothermic process, where the sample absorbs energy during a phase transformation, a peak becomes evident in the heating phase. On the other hand, during an exothermic process, where the sample releases energy during a phase transformation, a peak appears during the cooling phase.

A fully operational DSC system comprises several essential components (see Figure 2.3), including a purging gas composed of nitrogen, serving the double purpose of cell cooling, and enhancing heat transfer efficiency. The instrument contains the system electronics, while the cell monitors the differential heat flow. Additionally, the system includes a refrigerated cooling system and a computer equipped with TA Instrument Q2000 software.

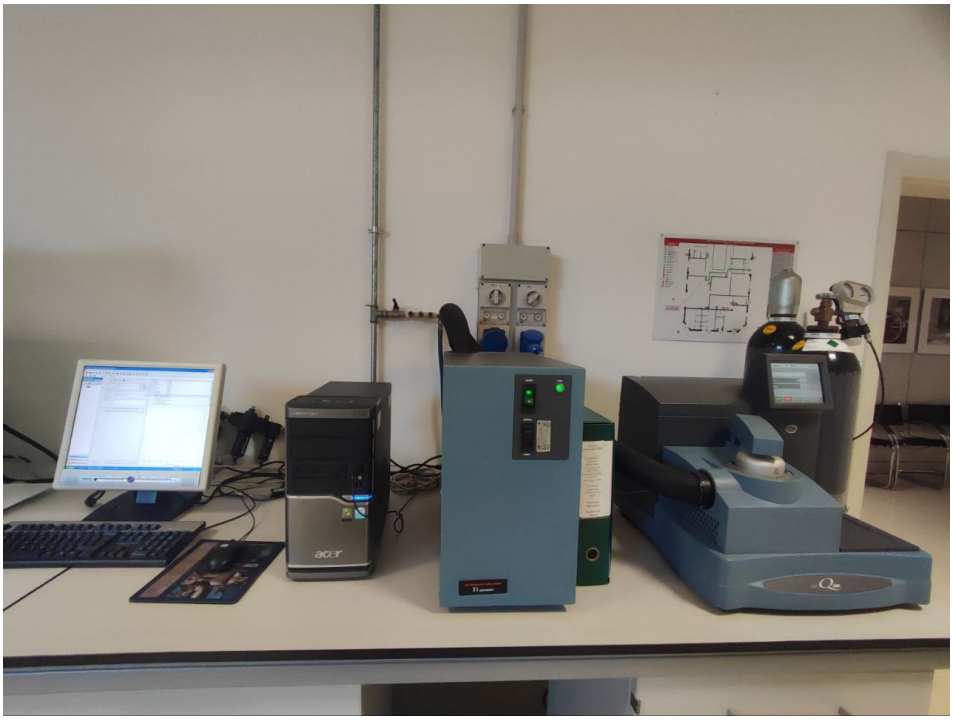

Figure 2.3 DSC setup.

The procedure adhered to the guidelines outlined in the Standard Test Method for Transformation Temperature of Nickel-Titanium Alloys by Thermal Analysis (F2004-17) [21].

The sequential steps involved in the DSC analysis, from sample preparation to data acquisition, are as follows:

1. Sampling: Utilize the Precision Cut-off Machine (described in § 2.2.2) to cut small NiTi pieces from the machined sample. The cut is performed employing a feed of 0.03 mm/s to prevent overheating during cutting. The mass of DSC samples tested should be ranged from 25 to 45 mg, according to the Standard Test Method.

2. Polish the Sample: Remove oxide layers by polishing the sample.

3. Ultrasonic Bath Cleaning: Wash the sample in a 99% ethanol ultrasonic bath and dry it using a hairdryer.

4. Weighing: Employ an analytical balance with a 100 mg capacity, capable of weighing to the nearest 0.1 mg, to measure the sample's weight.

5. Pan Placement: Position the sample on the aluminum pan and encapsulate it using the Tzero Sample Encapsulating Press.

6. DSC Cell Preparation: Open the DSC Cell, place the encapsulated sample pan on the test pedestal near the reference pan, and then close the cell.

7. Purge Gas Activation: Activate the purge gas at a flow rate of 50 mL/min.

8. Input Data Definition: Define input data through the machine software, specifying sample mass, sample name, and Test Method.

The following Test Method is used:

1. Ramp 10 °C/min to 90°C
2. Isothermal for 2 min
3. Ramp 10°C/min to -85°C
4. Isothermal for 2 min
5. Ramp 10 °C/min to 40°C

This involves elevating the sample temperature from the initial room temperature (24°C) to 90°C at a controlled rate of 10±0.5°C/min. The sample is then held at 90°C for 2 minutes to establish thermal equilibrium with the furnace. Following this, the sample is subjected to a cooling phase, decreasing from 90°C to -85°C at a rate of 10±0.5°C/min, with an additional 2-minute hold at -85°C. The subsequent step consists of reheating the sample to 40°C, maintaining the same heating rate. This entire sequence completes one cycle of the procedure.

9. Data Acquisition: Capture and document the curve obtained from both the cooling and heating test procedures.

10. Post-Processing: Start the post-processing phase of the data obtained.

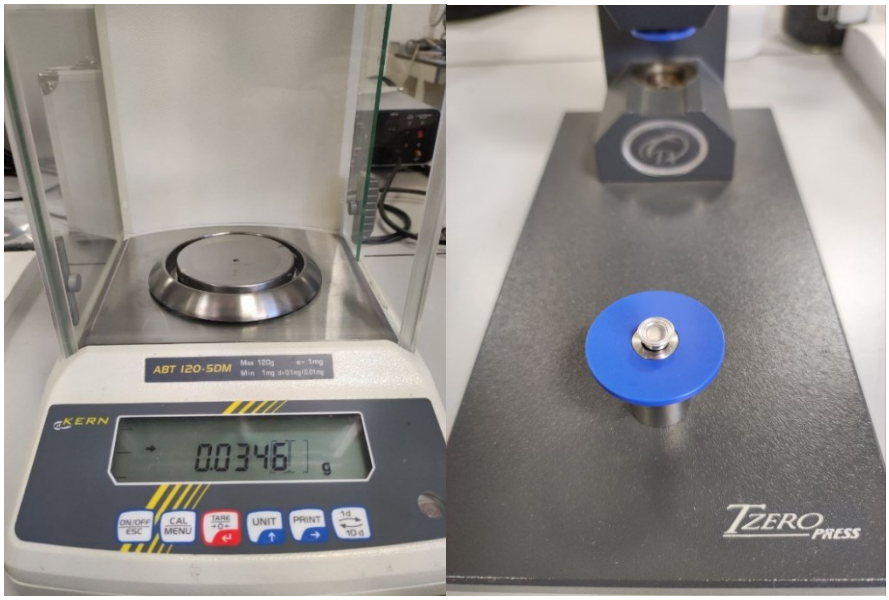

Figure 2.4 Weighed and encapsulated sample in the Tzero press.

The TA Universal Analysis program of the TA Instruments software is used to post-process the DSC data. The graph represented in Figure 2.5 shows the relationship between heat flow and temperatures in a DSC conducted on a sample of pre-machined wrought NiTi, which is given as an example to explain what has been done even on AM NiTi samples before turning.

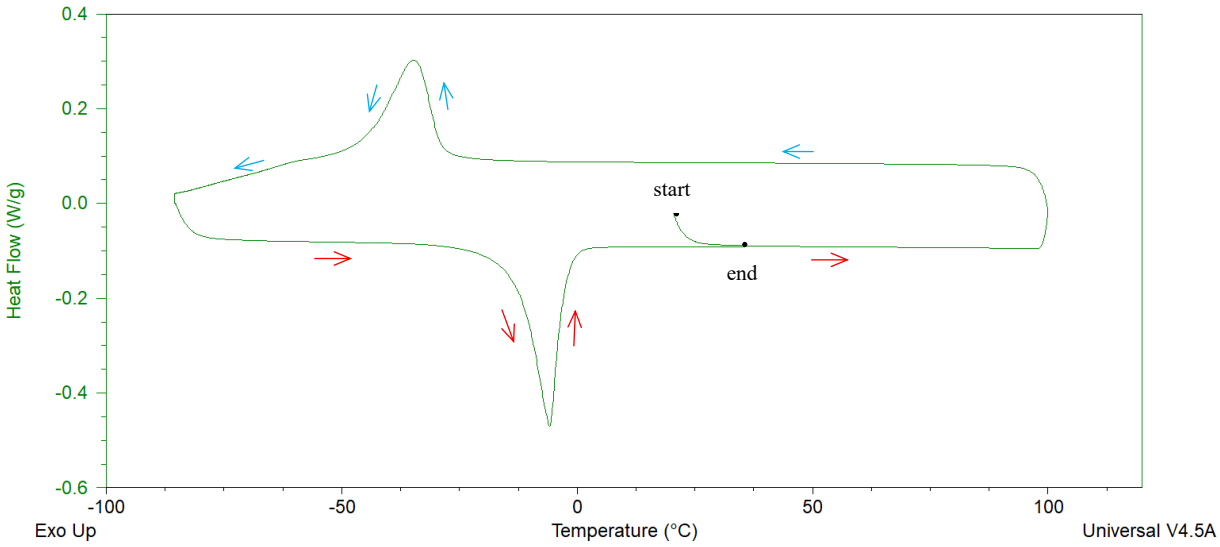

Figure 2.5 DSC graph of NiTi wrought pre-machining.

The enthalpy of transition, denoted as ΔH, can be determined by integrating the peak corresponding to the specific transition using the following equation:

$$\Delta H = KA \tag{2.2}$$

where K represents the calorimetric constant (which may vary between instruments), and A is the area under the curve.

The function Integrate Peak/Sig Horizontal of the software is utilized to calculate the integration which serves to determine ΔH. Firstly, a baseline is established, namely the line used as the base for calculating the peak area. The resulting value automatically appears on the graph as well as the curve's tangent and its intersection with the baseline. This intersection signifies the beginning of the peak and corresponds to the temperature at the onset of the transformation. Secondly, employing the Onset Point function involves drawing a tangent from the descending part of the peak. The intersection of this tangent with the baseline reveals the temperature at the end of the transformation. Additionally, the temperature values for the peaks (M_p and A_p) are plotted automatically. This is how the transformation temperatures are calculated.

Figure 2.6 depicts the graph, showcasing the calculated temperatures and enthalpy values derived from the graph presented in Figure 2.5.

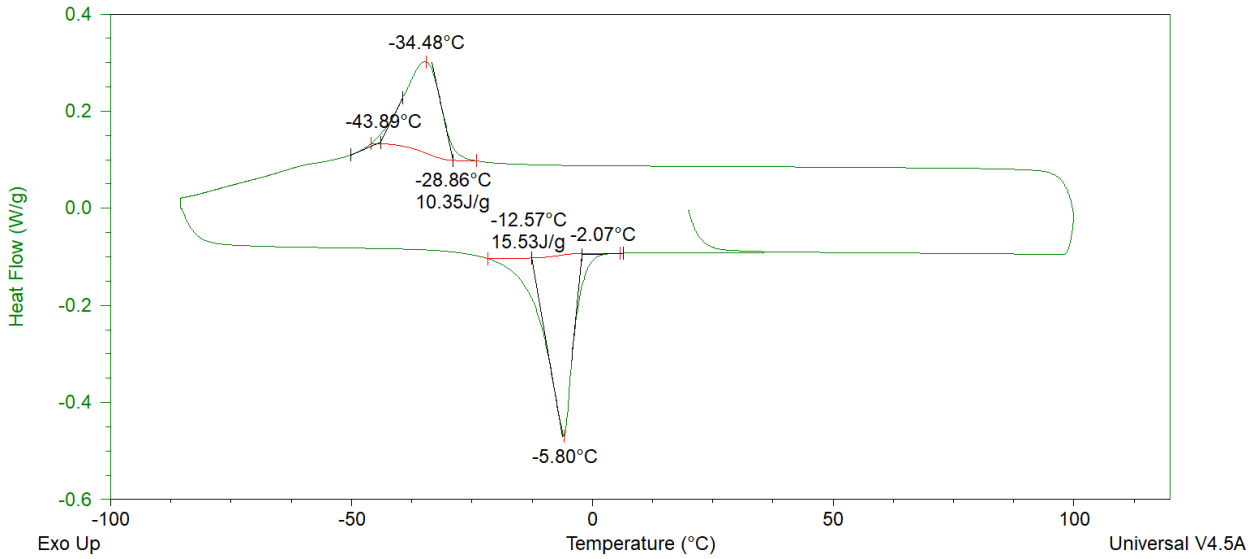

Figure 2.6 DSC graph with TTs and ΔH.

2.2.2 Microstructural Analysis

An analysis of the microstructure before turning provides detailed information about the composition and structure of the two differently manufactured NiTi samples, before they

undergo the turning processes. This type of analysis is useful to evaluate the characteristics of the initial material and predict how the material will respond to the machining process. For instance, it can lead to the detection of grain size and shape, the crystal structure of the material, or the presence of inclusions and defects in the microstructure that can affect the workability of the material. The process of microstructural observation involves polishing the samples to create a smooth surface and then subjecting them to chemical treatment to induce corrosion along grain boundaries. This corrosion reveals variation in light reflection between corroded and non-corroded areas, helping in the microstructural analysis. To achieve a polished surface on Nitinol, the initial step involves cutting small samples which are subsequently embedded in resin. The detailed steps for this preparation are outlined in paragraphs below.

2.2.2.1 Cutting

Utilizing the QATM™ compact automatic precision cut-off machine, Brillant 210A, Nitinol pieces were accurately cut from both wrought and AM samples. The machine, equipped with a variable speed cut-off wheel (150-3000 rpm) and a sample holder for positioning the specimen, allows for precise manual monitoring of the Y-axis (with a precision of 5 μm) for parallel cuts. To prevent excessive heat and potential phase changes in the material, coolant was applied to the cutting area.

The cutting-off parameters were set as follows:

- Speed of the cut-off wheel: 2200 rpm

- Feed rate: 0.04 mm/s (feed rate possible ranges: 0.03 – 0.05 mm/s)

Figure 2.7 QATM™ cut-off machine, Brillant 210A.

2.2.2.2 Mounting of Specimens

The mounting process for nitinol samples was performed at room temperature, using a cold method and a specific epoxy resin, a combination of Epoxy 1000 Harz and Harter 1000 resins (see Figure 2.8). The steps taken during the encapsulation process with this resin mixture are now described. First, the sample preparation was carried out, making sure that the objects intended for encapsulation were perfectly clean and dry, subsequently establishing their optimal position inside the sample holders. Subsequently, the amount of resin required for the correct encapsulation of all samples was measured and mixed. The resin and catalyst were mixed according to the recommended ratio, which included 10 parts of Epoxy 1000 Harz resin for 2 parts of Harter 1000. A correct mixing of the resin and the catalyst is essential to obtain a uniform hardening. Subsequently, the mixed resin was poured onto the objects to be encapsulated inside the sample holder, ensuring uniform coverage. Finally, it was left to harden for at least 24 hours, during which the encapsulated samples were left undisturbed so that the resin could dry and harden completely.

Figure 2.8 Epoxy resin and encapsulated samples.

2.2.2.3 Abrasion and Polishing

To achieve a reflective metal finish, the specimens undergo a polishing process after embedding. The Abramin-controlled machine is employed for grinding and polishing, with an horizontally rotating disc and a sample holder eccentrically pressed against it (see Figure 2.9). Adjustments for pressure, lubricant, and cooling water can be manually determined, while the machine autonomously manages time and disc speed. The grinding and abrasion sequence progresses from coarse to fine using P500, P800, P1200 and P4000 papers. The sample should be washed and cleaned whenever changing the paper to prevent impurities and small particles from contaminating the finer abrasive paper.

The same machine is then utilized to conclude the polishing procedure and attain a mirror-like finish on the specimen. For this step, a specialized solution is applied. This solution comprises 2/3 volume of alkaline silica suspension with a particle size of 0.2 µm and 1/3 volume of 30% hydrogen peroxide (H_2O_2). A perforated cloth, specifically designed for silica suspensions, was used. At this stage, the sample is mirror-polished, completely clean, and free of impurities.

Figure 2.9 Abramin-controlled machine.

2.2.2.4 Etching

After polishing, the metallographic specimen has a smooth, reflective surface that appears very clear under an optical microscope. In this condition, cracks, porosities, or metallic inclusions can be identified, as they reflect light differently than the surrounding metal matrix. However, to examine the microstructure of the material, a chemical or electrochemical attack is necessary. The attack aims to preferentially corrode the grain boundaries or a specific phase. Sometimes, granules are dissolved differentially according to their crystallographic orientation. The corroded area reflects light differently than the non-corroded area, allowing the microstructure to be observed due to the light-dark effect created. The chemical attack on the Nitinol, performed with a solution of 1 ml HF, 2 ml HNO and 47 ml H_2O, for about 45 seconds, allowed the microstructure of the material to be identified, revealing the grain boundaries.

2.2.2.5 Optical Microscope

To conduct the metallographic analysis, a Leica® DMR optical microscope equipped with a Zeiss AxioCam ERc5s camera was used. The microscope's integrated software allows real-time display of the sample on the monitor, image adjustment, and post-acquisition measurements. This microscope model is equipped with six objectives: 5x, 10x, 20x, 50x, and 100x, while the camera offers 10x magnification. During the analysis, the sample was fixed on a support plate using plasticine and a press, ensuring optimal positioning for orthogonal observation of the objective.

2.2.2.6 Scanning Electron Microscope

The Scanning Electron Microscope (SEM) is an essential instrument for the detailed analysis of the microstructure of solid samples. This instrument consists of an electron emitter, usually a tungsten filament, which generates an electron beam focused on the sample. The interaction between the electrons in the beam and the sample produces different types of signals, including backscattered electrons (BSE), secondary electrons (SE), and X-rays, which are subsequently detected by specific detectors. The BSE mode provides information on the composition of the sample based on the backscatter coefficient – it depends on the atomic number Z: the higher it is, the clearer the material appears in the image – while the SE mode provides high-resolution images of the surface morphology. To generate the electron beam, a tungsten filament can be used to enhance brilliance and durability. The SEM must operate in a vacuum environment to function properly and generate the above-mentioned signals. The specific model used at the Te.Si. laboratory is the FEI Quanta 450, which has three operating modes: HiVac (High Vacuum), LowVac (Low Vacuum), and ESEM (Environmental Scanning Electron Microscope).

The detailed analysis procedure shall include the following steps:

1. Ultrasonic bath of the sample for about 3 minutes in ethanol, to carefully clean the sample.
2. Drying of the sample, taking care not to touch the area to be examined.
3. Ventilation of the scanning electron microscope chamber, followed by the opening of the door.
4. Application of a double-sided carbon tape on the sample board, to make the ground connection of the metal sample, making sure it does not cover the area to be observed.
5. Care should be taken that samples do not cause collisions with internal parts of the SEM when closing the door.
6. Closing the door and starting the vacuum pump, keeping the door pressed in the closing position until the seals seal thanks to the generated vacuum in the chamber.
7. Adjust the sample height to about 10 mm from the microscope lenses.
8. Electron beam ignition and sample focus first at low magnifications.
9. Performing the analysis by selecting the most appropriate detector (BSED or ETD) and setting the working voltage of the filament and the beam size (typically 20 kV and spot size 5).

10. Beam shutdown when no analysis is being performed, to preserve the filament. Also, keep the chamber closed and vacuum to avoid contamination.

2.3 Machining Operation

Machining processes are crucial in converting raw materials into precise components in various industries. These processes involve the removal of material from a part to achieve desired shapes, dimensions, and surface finishes. In the field of machining, a fundamental concept is the orthogonal cutting model, which stands as a keystone to understanding the mechanics involved in material removal. In the context of orthogonal cutting a perfectly sharp tool enters the workpiece at a right angle. This action gives rise to discernible cutting forces and distinctive chip formation patterns, induced by plastic deformation within the shear plane. The contact between the machined material and the tool is supposed to be at the level of the tool rake face and no helical chip is formed. This two-dimensional model - operating under plane strain conditions - is a fundamental framework for analyzing the intricate interplay of forces, temperatures, and material flow during the machining process, especially during turning, which is one of the types of machining operations. Figure 2.10 shows a representation of orthogonal cutting model.

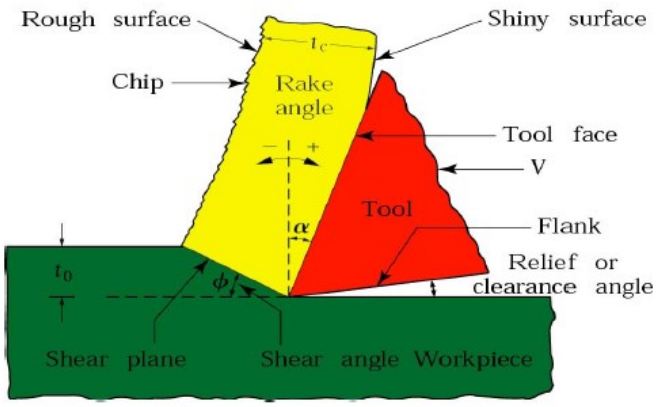

Figure 2.10 Representation of chip formation in the orthogonal cutting model.

Tool geometry is defined by the rake angle (α), situated between the tool face and the direction perpendicular to the cutting speed, as well as the clearance angle, which is the angle between the tool flank and the cutting direction.

The depth of cut, denoted as t_0, represents the undeformed chip thickness, namely the desired thickness of material to be removed during the machining process, while t_c denotes the thickness of the resulting chip, formed along a shear plane determined by angle ϕ. Based on experimental

observations, it is consistently noted that the depth of cut (t_0) is always inferior to the chip thickness (t_c), and their proportional relationship is denoted as the cutting ratio (r).

$$r = \frac{t_0}{t_c} < 1 \tag{2.3}$$

However, t_c can be measured experimentally, knowing t_0 and α, the shear angle ϕ can be calculated from the following equation:

$$\tan\phi = \frac{r\cos\alpha}{1 - r\sin\alpha} \tag{2.4}$$

Knowing this angle is crucial for determining the velocity of the chip relative to the cutting speed.

Using geometric relations, it is possible to determine the sliding force (F_s) and the force normal to the sliding plane (F_n) using the shear forces (F_c) and feed resistance forces (F_t), both of which can be measured experimentally. The resultant (R) of the forces Ft and Fc can be decomposed from the tool face into N and F, representing the normal force and tangential frictional force, respectively. Figure 2.11 represents all forces involved in orthogonal cutting model. These are related through Coulomb's relation, with μ as the coefficient of friction and β as the angle of friction:

$$F = N \cdot \mu = N \cdot \tan\beta \tag{2.5}$$

As manufacturing continues to evolve with technological advances, a comprehensive understanding of machining processes and the application of models such as orthogonal cutting remain essential to optimize efficiency and achieve precision in the production of mechanical components.

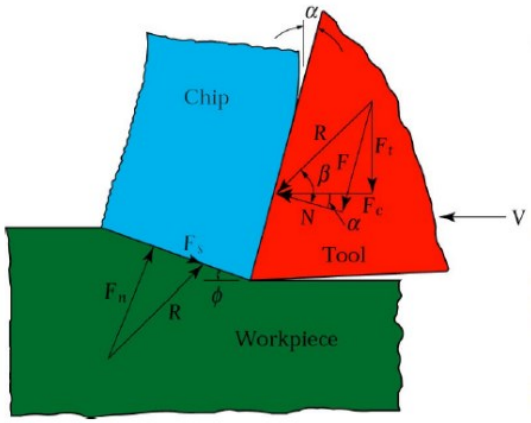

Figure 2.11 Cutting Forces in the orthogonal cutting model.

2.3.1 Turning

Turning, a method for removing chips during machining, involves securing the workpiece with the chuck's grips and inducing rotation, creating components with axisymmetric features. The cutting motion of the tool is rotational, while the feed motion may follow a longitudinal or curved path. Figure 2.12 shows a scheme of a workpiece gripped in a spindle and the main turning parameters.

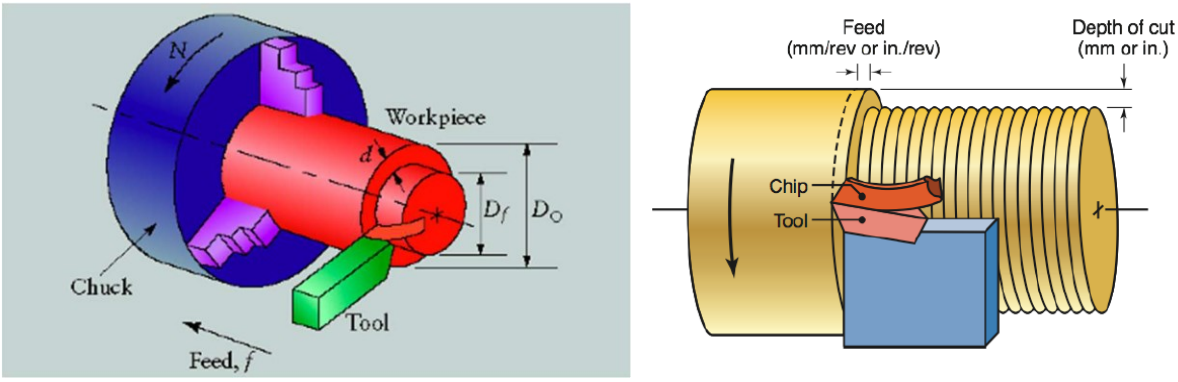

Figure 2.12 Schematic example of a turning process and process parameters.

The principles of the orthogonal cutting model are equally applicable to turning, employing the distinctive parameters specific to this machining process [22], which are:

- Cutting speed, V_c [m/min], the relative rotational speed, between the tool and the workpiece. It is calculated with the following equation, where D is the perimeter of the workpiece [mm], and N is the spindle speed [RPM].

$$Vc = \frac{\pi \cdot D \cdot N}{10^3} \tag{2.6}$$

- Feed, f [mm/rev], the distance traveled by the tool on the feed direction for each turn of the workpiece. It corresponds to the undeformed chip thickness, t_0, of the orthogonal cutting model.

- Feed rate, v_f [mm/min], the speed of the tool in the feed direction. The following equation defines its calculation.

$$v_f = N \cdot f \tag{2.7}$$

- Depth of the cut, d [mm], it's the amount of material to be removed, measured perpendicular to the feed direction, and calculated with the underlying equation. Where D_0 and D_f are the initial and final diameter of the workpiece.

$$d = \frac{D_0 - D_f}{2} \tag{2.8}$$

- Material removal rate, MRR [mm^3/min], describes the volume of material removed in the unit of time and it's calculated as follows.

$$MRR = \pi \cdot \left[\left(\frac{D_0}{2}\right)^2 - \left(\frac{D_f}{2}\right)^2\right] \cdot v_f \tag{2.9}$$

  In cases where Vc is constant, this formula should be used:

$$MRR = Vc \cdot f \cdot d \tag{2.10}$$

- Machining time, t [min], i.e. the time required to machine a section along a stretch of length l, which does not include the time required to approach and remove the tool from the workpiece, is calculated using the following formula.

$$t = \frac{l}{f \cdot N} \tag{2.11}$$

Common problems in machining of NiTi alloys, thoroughly analyzed in the § 1.3.3, could be mitigated by a proper optimization of the cutting parameters mentioned above. [13]

Tool geometry is also crucial, with the various angles performing key functions. Upper rake angles guide chip flow and tool strength. If positive, they reduce forces and temperatures, but impose limited cutting angles: the primary upper rake angle overrides the secondary angle, determining chip direction. Lower rake angles handle interference and tool-workpiece friction, if too high they cause chipping which increases tool wear. The angles of the main and secondary cutting edges affect chip formation, tool strength, and cutting forces. The tip radius impacts the surface finish and tool strength: a smaller radius increases roughness and reduces strength, while a larger radius can generate vibration.

The proper choice of cutting tool materials is also crucial due to the extreme conditions they are subjected to during machining operations. The tool must possess hot hardness to maintain performance at elevated temperatures, toughness to resist impact forces in interrupted cutting operations, wear resistance to ensure acceptable tool life, and chemical stability to avoid negative reactions with the workpiece material. Numerous materials with these properties are

available, with the most frequently employed options including carbon steels, high-speed steels, metal carbides, and coated tools. Depending on the type of tool chosen, there are typical ranges of cutting parameter values for turning operations. [22]

The three main forces affecting the tool are fundamental to the assessment of tool integrity in machining. The cutting force, Fc, acts on the tool tip from top to bottom and is the one that provides the energy required for the cutting operation. The feed force, Ft, acts laterally along the feed direction, while the repelling force, Fr, acts radially tending to move the tool away from the workpiece. [22]

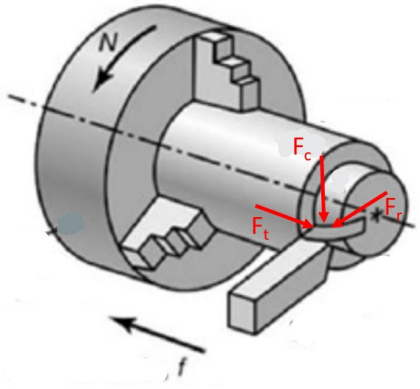

Figure 2.13 Force components.

Cooling lubricants, commonly used in machining operations, have several purposes, including cooling the cutting zone, reducing friction and tool wear, and protecting against corrosion. These fluids can act as coolants and lubricants. However, in interrupted cutting operations, they can cause thermal fatigue cracks or thermal shock on the tool. [21] In addition, the use of cooling lubricants can pose environmental challenges and require costly recycling and disposal processes. The choice between lubricants and dry machining depends on various factors, including materials and machining conditions.

2.3.2 Setting Of Parameters In Machining Trials

All the samples were turned longitudinally on a Mori Seiki™ CNC lathe using VCEX 110301L-F 1125 inserts. This type of lathe has 12 turrets for various machining operations. The cutting parameters used were chosen from ranges recommended by the manufacturer of the inserts, for machining difficult-to-machine materials, namely ISO-S alloys. Specifically, the recommended ranges are as follows: a_p=1 mm (0.05 - 3), f=0.07 mm/rev (0.01 - 0.21), Vc= 31 m/min (31 – 31), where a_p corresponds to the depth of cut, f to the feed rate and Vc to the cutting speed.

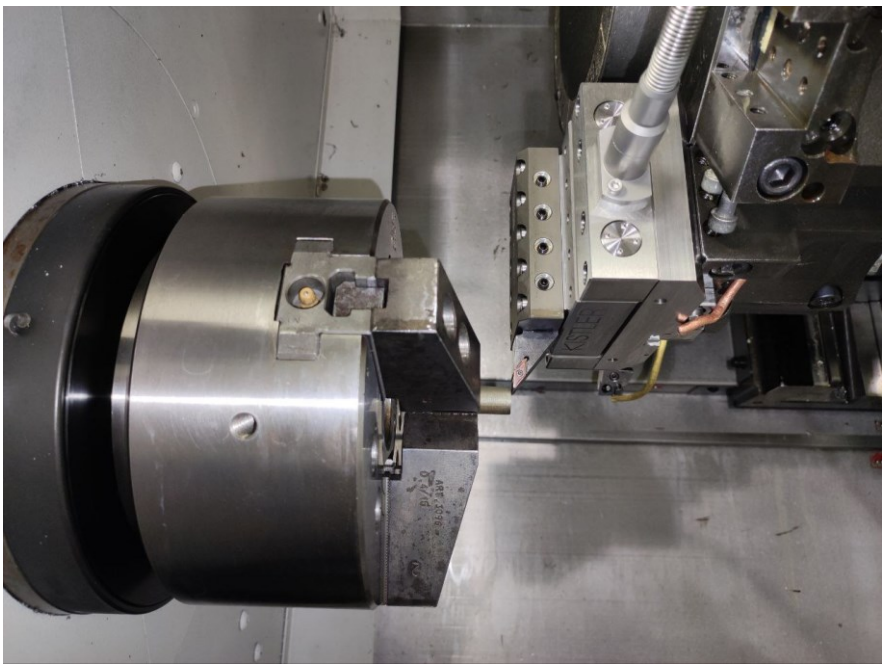

Figure 2.14 Mori Seiki™ CNC lathe set up with VCEX 110301L-F 1125 tool.

Initially, the cutting parameters were optimized by turning tests on a wrought NiTi sample, following the ranges just mentioned. In detail, the feed has been kept constant at 0.05 mm/rev in all lathes. In the first phase, the depth of cut was kept constant at 0.25 mm, while the cutting speed was varied, including the recommended value of 31 m/min, plus a lower value (20 m/min) and a higher one (50 m/min). The optimal result, evaluated on the basis of a lower surface roughness - a parameter that reflects the surface integrity of a workpiece, as will be discussed in the § 2.4.4 - was obtained with the highest cutting speed. Subsequently, the depth of cut was varied while maintaining the best speed just determined. The three considered cutting depths were 0.25 mm, 0.35 mm, and 0.5 mm. Once again, the best results in terms of surface roughness were obtained with a depth of cut of 0.35 mm.

The chosen experimental approach involves the use of two different cutting speeds for both types of material manufacturing, conventional NiTi and AM NiTi. This was done with the aim of evaluate the effect of cutting speed on tool-wear rate and the consequent impact on the superelasticity of Nitinol in each machining process. The values in the underlying

Table 2.2 represents the cutting parameters used in the machining operations conducted in the study.

Type of NiTi manufacture	Cutting speed [m/min]	Feed rate [mm/rev]	Depth of cut [mm]	Insert
Conventional	50	0.05	0.35	1.A ut_1_VCEX
	80			2.B ut_2_VCEX
AM	50	0.05	0.35	3.B ut_3_VCEX
	80			6.A ut_4_VCEX

Table 2.2 Cutting parameters and tool used.

VCEX 1103 01L-F 1125 inserts belonging to the CoroTurn® 107 family of Sandvik Coromant™ were chosen for the sample turning. This type of tool is also suitable for processing materials of ISO S class, which includes nickel and titanium alloys. These alloys tend to the adhesion of the processed material (which therefore generates Built-Up Edge), harden during processing, generate a lot of heat, and are also very difficult to work with, resulting in a reduction in tool life compared to machining other materials. In Figure 2.15 there is a photo of the inserts and their technical illustration taken from the manufacturer's website. The main features of this type of insert are also retrieved from the manufacturer's website and reported in Table 2.3.

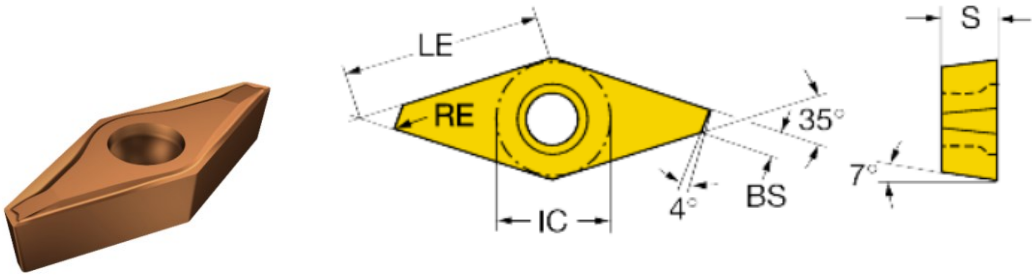

Figure 2.15 Sandvik Coromant™ VCEX 1103 01L-F 1125 insert.

VCEX 1103 01L-F 1125	
Number of cutting edge	2
Corner radius	0.1 mm
Substrate	HC
Coating	PVD TiAlN + TiAlN

Table 2.3 Insert's most important features.

The inserts in question were assessed before turning to verify that they met the characteristics declared by the manufacturer and that the coating was in good condition. This was done by analyzing them at the SEM in order to prefer the best for turning operations (see Figure 2.16).

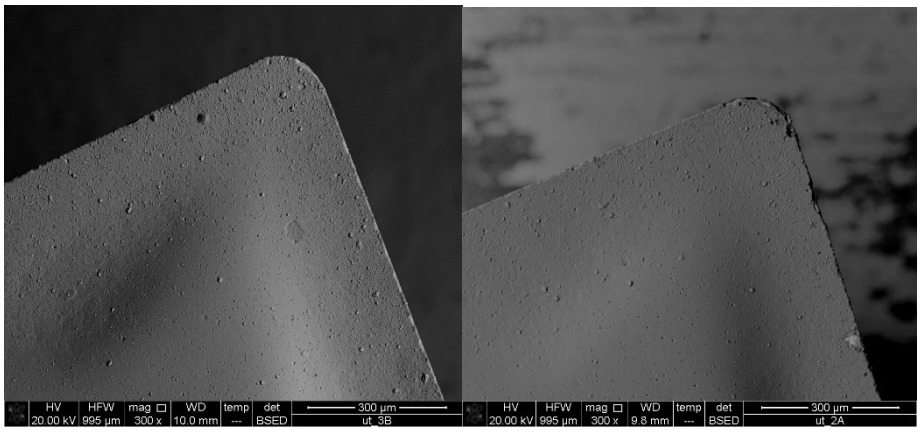

Figure 2.16 Example of SEM images of received inserts, on the left a well-coated tip, to the right a tip where part of its coating is damaged.

The inserts placed within a box were labeled with a numerical designation, followed by a dot and then a letter distinguishing between the two cutting edges (A or B). Four insert tips were selected, each systematically renamed and assigned to a specific experimental condition as illustrated in Table 2.2 Cutting parameters and tool used.

A classic flood cooling lubricant was chosen because, for the purpose of the thesis, it was found to be necessary to cool the cutting zone, reducing the temperature and possible distortion of the workpiece, reducing friction and wear, improving tool life and workpiece surface finish, and to reduce forces in the machining process.

2.4 Characterization After Machining

2.4.1 Tool Wear Characterization

One of the most critical parameters for assessing the machinability of a material is the tool life. Tool life is defined as the total cutting time of the tool to reach a critical value of tool life-criterion. The latter is defined as the threshold of a tool wear measure. The aim of a tool-life testing is to determine how some factors affect the useful life of a tool [15].

Since the tool wear isn't an absolute value, the proper choice of materials for cutting tool with a good wear resistance is an aspect of primary importance, as already discussed in 2.3.1.

Beyond its role as a parameter influencing the efficacy of a machining process, tool wear has an influence on the features of the final product. This impact can be summarized as follows: growth in production costs, influence on the surface quality and integrity of the processed material, amplification of cutting forces resulting in augmented energy consumption, and elevation of cutting temperatures with the potential to induce a modification in the active phase of the material during the cutting process.[18]

Tool wear is influenced by various factors, including the physical, mechanical, and chemical properties of tool and workpiece materials, tool geometry, the use of cooling lubricants and cutting parameters (such as cutting speed, cutting depth and feed rate). All types of wear occurring on a tool depend on the complex interaction of these variables. The occurrence of wear in cutting tools can be represented, as shown in the Figure 2.17, and the different kind of wear can be identified mainly as flank wear, crater wear and chipping of the cutting edge.

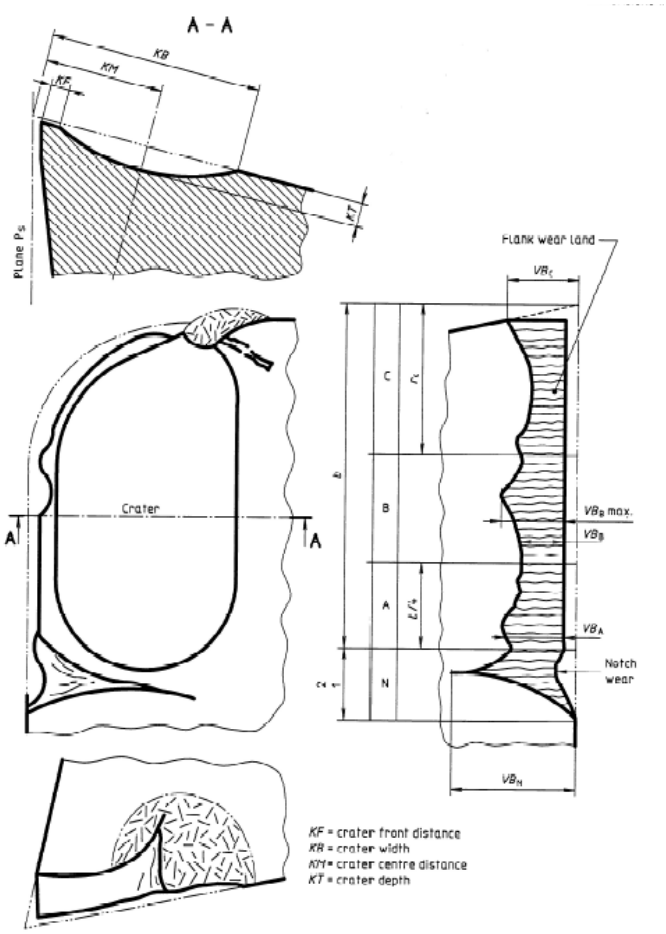

Figure 2.17 Tool wear measurements.

Wear is a gradual process, while chipping of the cutting edge is sudden and leads to rapid tool failure. In addition to wear, plastic deformation of the tool can occur when the material loses strength and hardness at high working temperatures. All these processes, including wear and damage, alter the profile of the cutting edge, thus influencing the results of the machining process.

The evaluation often involves assessing the degree of wear in terms of width, length, or other measurable parameters. For enhanced accuracy and comparability of test results, it is crucial to define a specified value of the tool-life criterion [15]. When multiple types of wear become measurable, it is advisable to record each type. Under these circumstances, the type believed to contribute the most to the termination of useful tool life in a specific series of tests should guide the selection of a tool-life limit. The end of tool life is considered reached when any kind of the wear criterion is attained. In cases where it is unclear which type of wear predominates, the utilization of two criteria or a mixed criterion becomes a viable approach. This strategy ensures a comprehensive evaluation and facilitates a better understanding of tool performance.

2.4.1.1 Flank Wear

This type of wear is generally attributed to the sliding of the tool on the machined surface, resulting in adhesive and/or abrasive wear depending on the materials involved and the temperature rise during machining, so it's a thermally activated phenomenon. A relationship that binds the cutting speed and the duration of the cutting edge is Taylor's law, described by the following equation.

$$Vc \cdot T^n = C \tag{2.12}$$

Where Vc is the cutting speed (m/min), T is tool life (min), n and C are empirical constants that depend on the materials of both tool and workpiece.

In numerous instances, the width of the flank wear land tends to be consistently uniform along the central section of the straight segment of the major cutting edge. Measuring the width of the flank wear land is generally a straightforward task. Typically, all cutting tool materials exhibit a high initial rate of flank wear, which tends to decrease significantly after a brief period of cutting, unless excessively high cutting speeds are employed, as can be seen from Figure 2.18. When machining at elevated cutting speeds, the increase in flank wear for all cutting tool materials usually follows an approximately uniform pattern after the initial phase of high wear. The concluding segment of the flank wear versus time graph often reveals an accelerated wear rate, ultimately leading to catastrophic failure.

For wear measurement purposes, the primary cutting edge is divided into four zones, as illustrated in Figure 2.17. Zone C is the curved part at the tip of the tool, and the flank wear detected in this zone is defined as VB_C. Zone B represents the straight segment of the cutting edge located between zones C and A., and the specific flank wear at this level is called VB_B. The zone A constitutes one-fourth of the length of the worn cutting edge, situated farthest away from the tool corner. Zone N has an extension beyond the region where the tool and workpiece come into contact, spanning approximately 1 mm to 2 mm along the major cutting edge. The wear observed in this zone is characterized by a notch-type pattern, which is distinct from of flank wear [15].

Generally, the width of the flank wear is the predominant criterion for every type of tool. For irregularly worn flanks, the typical criterion is the maximum width of the flank wear land in zone B, denoted as VB_{Bmax}, which is set at 0.6 mm. Alternatively, in cases where the flank wear exhibits a more uniform pattern, the average width, VB_B = 0.3 mm, is considered as the

criterion. This approach provides a standardized and practical method for evaluating the wear characteristics of cutting tools.

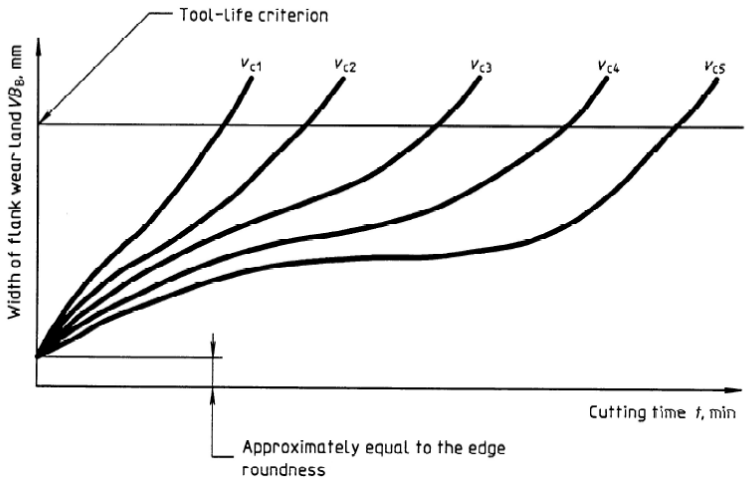

Figure 2.18 Flank wear vs. time for different cutting speeds, vc1 - vc5 [15].

2.4.1.2 Crater Wear

The factors inducing wear on the tool flank are likewise responsible for the wear observed on the tool rake face, commonly known as crater wear. It is known that the temperature and the level of chemical affinity between the tool and the workpiece are the most important among these aspects. Notably, the position of the maximum crater depth typically coincides with the point of highest temperature at the tool-chip interface. The increase of temperature explains the mechanism of crater formation and propagation, involving diffusive phenomena (atom migration) as well as abrasive and adhesive processes.

In this work, the crater wear was evaluated and correlated to the roughness of the workpiece, illustrated in 2.4.4. The wear crater is a phenomenon that varies over time, because during machining, some pieces of adhered material, namely the built-up-edge (BUE), could detach from the tool, eventually increasing roughness, thereby worsening the surface quality.

2.4.1.2.1 EDS Analysis

To offer a more comprehensive elucidation of the aforementioned wear phenomenon, particularly concerning the identification of element distribution on the tool rake face during wear evaluation, Energy Dispersive Spectroscopy (EDS) was employed. EDS is an analytical technique utilized in scanning electron microscopy (SEM) for the identification and

quantification of elements in a sample. This method depends on the energy dispersion of X-rays emitted when an electron beam interacts with the sample. An energy detector gauges the distribution of these X-rays, enabling the identification of elements and the determination of their concentrations.

The Oxford Instruments AZtec EDS system in Te.Si. laboratory comprises the following components:

- EDS Detector, which captures the X-rays generated from the sample and converts their energy into a voltage signal of proportional size.
- Control Module, to communicate with and to control the EDS detector.
- EDS Computer, which runs the Aztec software, which is used to acquire, process, and analyze the EDS date, communicates with the microscope, and receives data from the control modules.

There are different acquisition methods available for this instrument. It was decided to employ the EDS SmartMaps function for mapping. After establishing parameters, the map data is gathered systematically, scanning the electron beam point by point across the area of interest in the SEM's field of view. For each point, an EDS spectrum is collected, measuring element intensities. EDS maps are then generated to display element intensity in relation to position. During data acquisition, various viewing options exist, including EDS layered images, where element colors blend and overlay on the electron image, providing an impression of phase distribution. Other viewing options include individual element maps, spectra containing EDS data from all points in the specified area, and spectra reconstructed from regions of the EDS map data.

2.4.2 DSC Analysis

The procedure extensively described in § 2.2.1 was also implemented on all samples post-machining processes. This enabled the collection of essential experimental results to understand the influence of machining under varying conditions on the superelasticity of NiTi. Since the phase state of NiTi significantly affects the machining performance of the alloy, it is crucial to examine it. Typically, cutting forces and tool wear are low during machining in the martensitic phase.

The important difference between the preparation of a sample for a pre-machining DSC and a post-machining DSC is that the cut in the latter case is performed to obtain a specimen primarily

composed of the external layer of the workpiece. The objective is to ensure that the analysis accurately identifies the process temperature, capturing the impact of the machining process on the workpiece, which is visible on its surface rather than in bulk.

2.4.3 Microstructural Analysis

The analysis of NiTi's microstructure is commonly conducted in studies on tool wear for several reasons. Firstly, knowing how the microstructure can alter during tool wear is essential to gain crucial information about the material's mechanical properties, including strength and hardness. Moreover, it allows the identification of phase changes contributing to the distinctive characteristics of NiTi. Another significant aspect involves alterations in the microstructure resulting from tool wear, such as plastic deformation, and the development of scratches, or fractures. These modifications can impact the durability and performance of Nitinol, underscoring the necessity to carefully monitor the microstructure throughout such investigations. Additionally, examining the shape of grains, inclusions, and other microscopic details provides specific insights into understanding fatigue strength and wear resistance of Nitinol within specific tool wear contexts. So, the analysis of microstructure in tool wear studies is of fundamental importance in comprehending the impact of differences in microstructure before and after machining with a tool exhibiting varying degrees of wear. This influence extends to the alteration of grain shape in the surface layers of the specimen, specifically those influenced by the machining process. Furthermore, it facilitates the detection of phase transitions between the pre- and post-machining states, thereby contributing to any modifications in the distinctive properties of NiTi, particularly its superelasticity.

2.4.4 Roughness Analysis

Surface integrity analysis techniques have been extensively employed to define the machinability of a material [22]. The general aim is to enhance the surface quality of manufactured components. Surface roughness is often used as an indicator for assessing surface quality as it provides a quantitative measure of surface asperities [23]. Several studies in the field of materials processing have examined how machining parameters (cutting speed, depth of cut, tool type, machining temperatures, residual stresses, etc.) influence surface roughness and, consequently, surface quality and surface integrity. In turning, the tool produces spiral feed marks on the machined surface of the workpiece in correspondence with its cutting motion.

These feed marks are more pronounced the greater the feed (*f*) and the smaller the tool tip radius (*R*), as expressed in the simplified equation describing the total height of the roughness profile (R_t). [22]

$$R_t \cong \frac{f^2}{8R} \tag{2.11}$$

The current standard that defines and enables the quantification of surface topography parameters is ISO 21920-2:2021. However, as this is a recently published standard, the software used in this study for analyzing surface quality still refers to the previous standard, defined by ISO 4287:1997.

Surface roughness is commonly defined as the presence of irregularities on a surface, resulting from variations in the heigh of individual points on the surface. Typically, surface roughness is assessed by slicing the component perpendicular to the targeted surface using a plane known as the relief plane. This slicing process produce the roughness profile, marked by the presence of alternating peaks and valleys. The periodicity of this profile can vary, depending on the spacing between the two above mentioned features. A profile exhibits three types of irregularities - shape errors, waviness errors, and roughness errors - that collectively contribute to the overall surface topography. Roughness, as quantified by the *R-parameters* of ISO 4287, is assessed independently of shape and waviness errors. To achieve this, the evaluation length is subdivided into smaller segments known as base lengths (*lr*), acting as low-pass filters. These base lengths serve to filter out wavelengths attributed to waviness error. The ISO for roughness measurements incorporates Gaussian filters denoted as λs and λc. λs excludes wavelengths below a specified threshold, treating them as background noise, while λc, also known as the cut-off, eliminates lengths above a certain value, typically equivalent to the base length. Other parameters to express the roughness are surface parameters (*S*), thereby extending in three dimensions the traditional *R* parameters.

In this thesis work conducted in the Te.Si laboratory, the Sensofar Metrology™ S Neox 3D optical profiler was employed to perform surface roughness measurements, and the Sensofar Metrology™ SensoSCAN software was used to process the scans.

The method employed for analyzing the surface involves positioning one of the profiler's lenses – Nikon™ TU Plan Flour EPI 2.5x lens – at the center of the machined specimen, to prevent the undesirable effects of turning, such as the formation of burrs at the ends of the part. Then with a larger magnifying lens – Nikon™ TU Plan Flour EPI 20x – the focus is directed onto the

sample. An image capture is performed to provide a preview of the scanned area and then the desired area size is chosen, divided into overlapping cells, with an overlap range from 15% to 20%. The scanning process starts with Bright Field mode and subsequently switches to Confocal mode for Z quote configuration. During this phase, precise adjustments are made to Top-Range and Bottom-Range parameters to cover the entire depth range, from the deepest valley to the highest peak. Following these adjustments, the area acquisition can start.

For the acquisition processing, the SensoView software is used, and a series of steps are taken to determine the *S* and *R* parameters of interest. The roughness measurements carried out for a wrought NiTi sample machined with *Vc*=80 m/min are given as an example to make clear the steps taken after each sample for each machining required by the test plan.

1. Raw acquisition and eventually a crop to remove the peripheral effects that may alter the measurements.

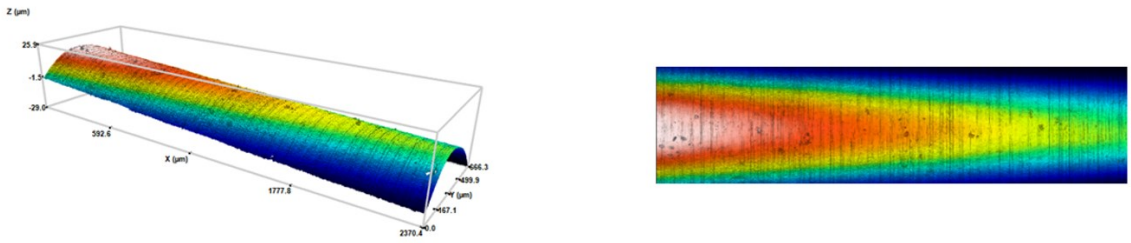

Figure 2.19 Raw acquisition in 3D (left) and 2D views (right)

2. Form removal: the Polynomial3D is applied to eliminate form errors arising from the cylindrical shape of the sample. A 6th degree polynomial has been selected to ensure optimal results.

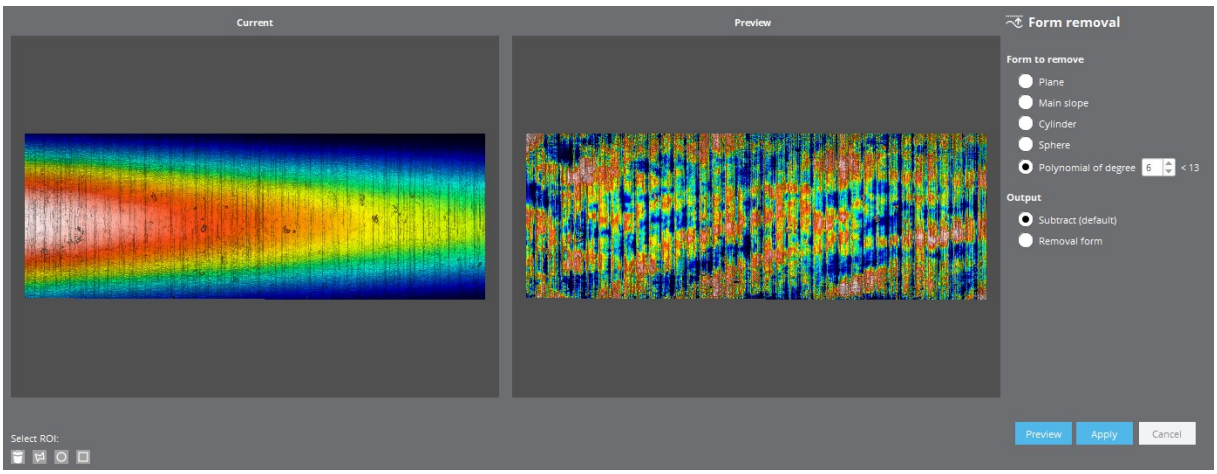

Figure 2.20 Form removal Polynomial 3D.

3. S-parameters: as per ISO 25178 guidelines, the Gaussian Filter values mentioned earlier are selected. λs is set at 2.5 µm, while λc is determined based on whether the profile is aperiodic or periodic. In the context of turning, which yields periodic profiles, the cutting filter is a function of *RSm* parameter – the average height of the profile feed marks. In this scenario, *RSm* corresponds to the feed value imposed during turning, specifically *RSm* = *f* 1 rev= 0.05 mm. ISO 4287 provides a table to ascertain the sampling length and subsequently determine the value of the cut-off filter based on the *RSm* parameter (see Table 2.4). After the application of the filter, the resultant parameters S are depicted in the lower right window in the Figure 2.21.

RSm (mm)	Sampling length, *lr* (mm)	Evaluation length (mm)
0.013<*RSm*≤0.04	0.08	0.4
0.04<*RSm*≤0.13	0.25	1.25
0.13<*RSm*≤0.4	0.8	4
0.4<*RSm*≤1.3	2.5	12.5
1.3<*RSm*≤4	8	40

Table 2.4 Sampling length corresponding to RSm range.

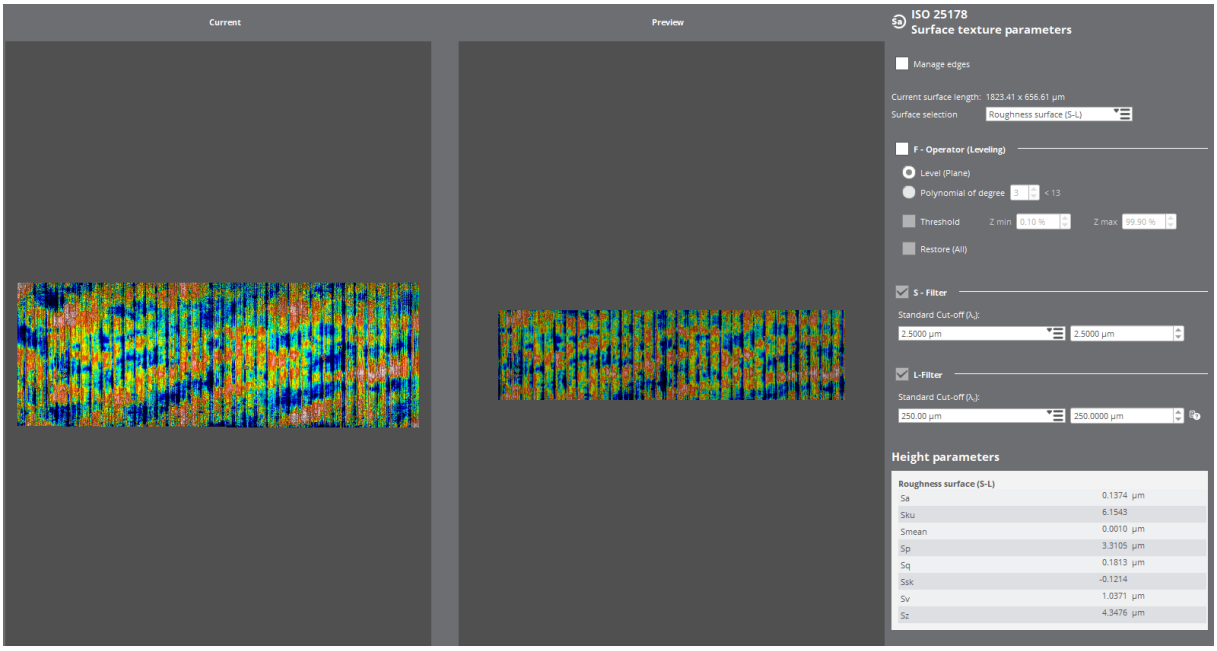

Figure 2.21 ISO 25178 filter for S-parameters.

4. R-parameters: Transitioning to 2D view and selecting a profile are the initial step, as it can be seen in Figure 2.22. Then, in accordance with ISO 4287, the measurement conditions suggested by the standard should be chosen, as illustrated in Figure 2.23. At this stage, the values corresponding to roughness and waviness become visible within the two windows below in Figure 2.23.

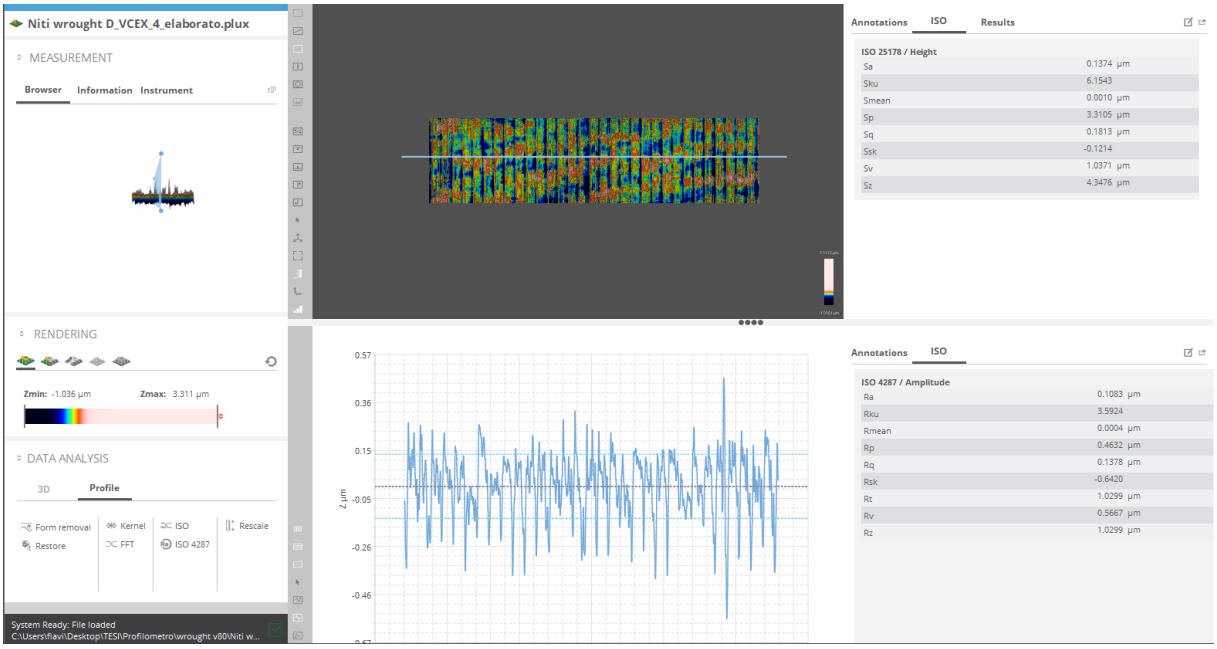

Figure 2.22 Software interface with an example of surface profile.

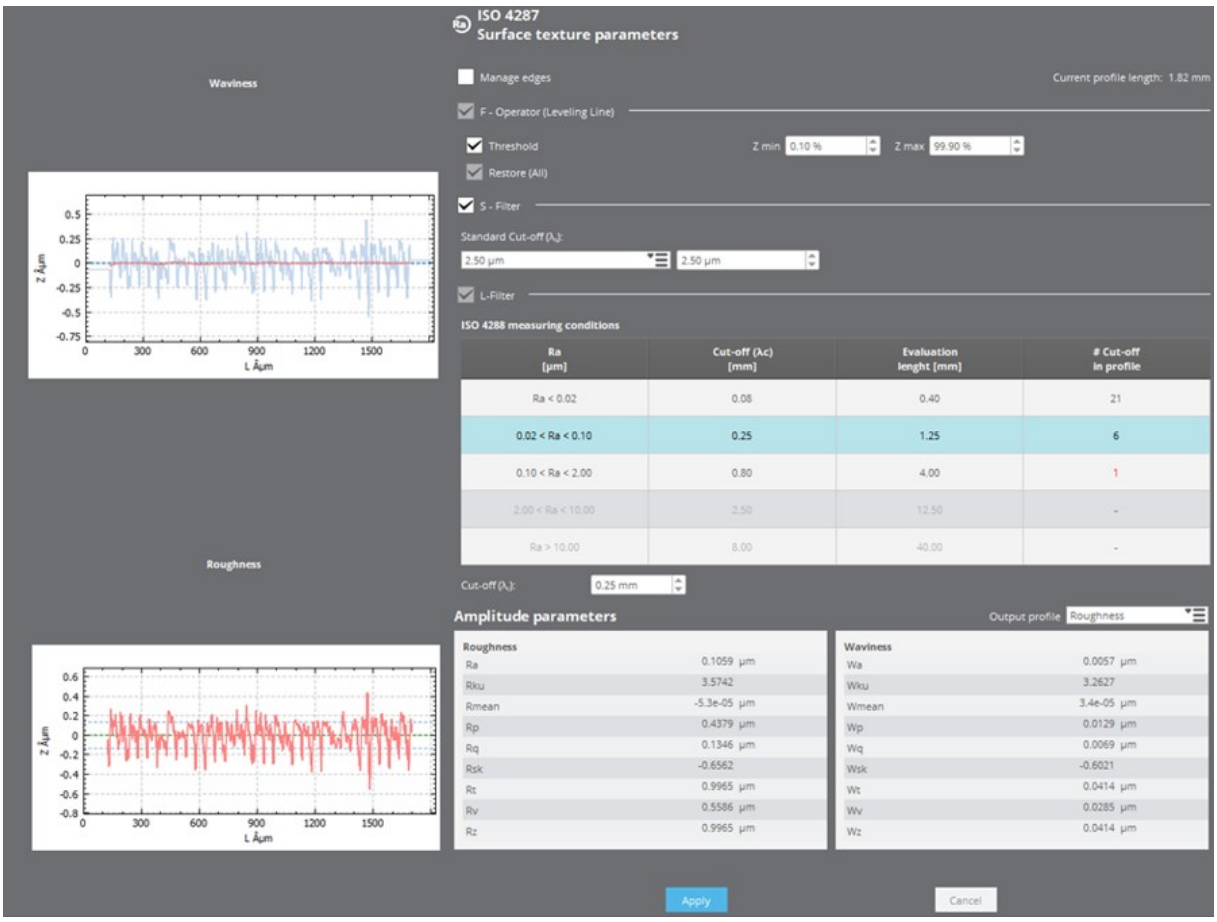

Figure 2.23 ISO 4287 for R-parameters.

2.4.5 Machining Forces Analysis

In the assessment of machining performances, during a progressive tool wear study, it is crucial to examine and to quantify the generated force components, mentioned in 2.3.1 and shown in Figure 2.13. Unlike the evaluation of flank wear and surface integrity, measuring forces does not require interrupting the machining process, thereby streamlining the procedure, and reducing time consumption [18].

These forces are gauged using a load cell equipped with four 3-component force sensors. Specifically, the Kistler Type 9129AA multi-component piezoelectric dynamometer has been employed. This instrument is designed to measure the orthogonal components Fx, Fy and Fz of the force that develops when cutting a metal in a lathe or milling machine. Due to the particular mounting of the sensor, a minimal temperature error is achieved. The ground isolation is guaranteed as well. Moreover, the dynamometer is corrosion resistant, so it is protected against the penetration of coolant.

The complete configuration of Kistler instruments includes a specific adapter for the lathe, the actual load cell, the tool-holder, suitable screws, a connection cable, the charge amplifier with an Ethernet cable, and the PC equipped with a USB stick containing the DynoWare force processing software license. In the Figure 2.24, a photo illustrates the load cell mounted on the adapter, complete with the tool-holder and connection cable.

The assembly of the dynamometer on the lathe involves the following step, with the important prerequisite of keeping every component thoroughly clean:

- Place the adapter onto the desired lathe turret.

- Position the load cell with the cable inlet facing upwards.

- Secure the load cell to the adapter by means of the specified screws, tightened with the torque wrench to the recommended force of 3-4 Nm.

- Fix the tool-holder to the cell in the same way.

- Place the insert and the tool in the tool holder.

- Pass the connection cable through the lathe and place it in the appropriate input of the cell ensuring proper pin connection.

- Connect the remaining end of the cable to the charging amplifier. Attach the Ethernet cable to the port on the back of the amplifier and connect the other end to the Ethernet port on the PC.

At this stage, data acquisition can start through the DynoWare software by identifying the IP address of the amplifier. Set the appropriate sensitivity parameters (see Table 2.5) and establish the pre-filter value to be less than about 1/3 of the natural frequency of the system calculated for the three force components.

Upon signal acquisition, it is essential to consider that it may be influenced by vibrations arising from the machining. The post-processing of the acquired signals was performed using MATLAB R2023a software since DynoWare is unable to export the filtered signal. It has been decided to implement a low-pass filter with a cut-off frequency set to 5 Hz.

Calibrated Range (kN)	Sensitivity (pC/N)
Fx 0 … 0.5	-8.059
Fy 0 … 0.8	-4.137
Fz 0 … 0.5	-8.086

Table 2.5 Sensitivity parameters.

Figure 2.24 Kistler Type 9129AA.

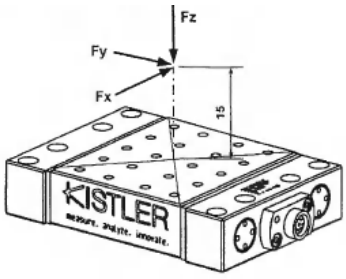

Figure 2.25 Forces component measured with dynamometer.

The forces generated during machining represent a parameter that can be readily measured during a wear analysis and can straightforwardly be correlated with the gradual progression of wear. The fundamental idea is that reduced cutting forces lead to lower power consumption. The correspondence between the forces developed in turning and those measured with the piezoelectric dynamometer is given in the following Table 2.6.

Measured Force	Machining Force	Description
Fx	Fr	Radial force
|Fy|	Fc	Cutting Force
Fz	Ft	Feed Force

Table 2.6 Forces notation.

CHAPTER 3

3. EXPERIMENTAL RESULTS

3.1 Characterization Before Machining

3.1.1 DSC Analysis

DSC analyses were conducted on samples prior to machining to make a comparison between conventional (C) and additive (AM) and subsequently evaluate changes in transformation temperatures (TTs)- especially A_f - caused by tool wear (see Figure 3.1). Figure 3.2 reports a confrontation between values of TTs in two aforementioned cases.

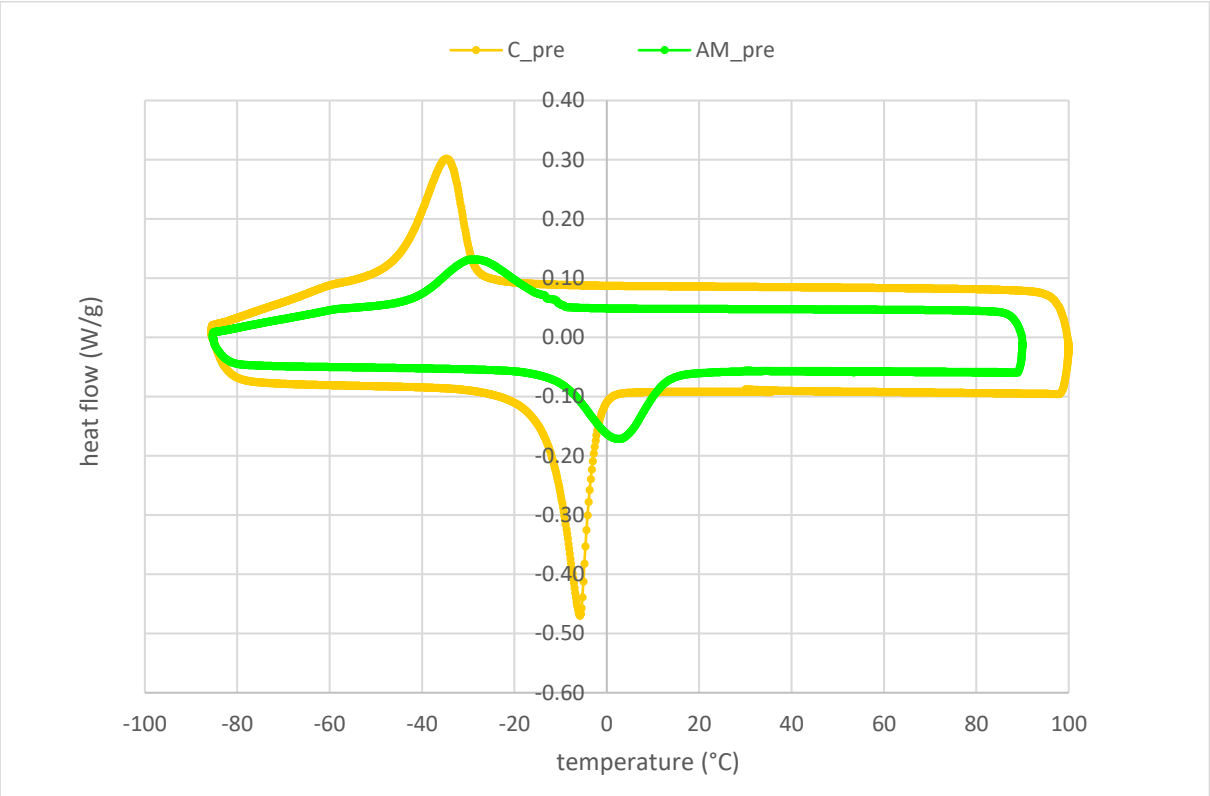

Figure 3.1 DSC curve of C_pre and AM_pre machining.

Figure 3.2 TTs of C_pre and AM_pre machining.

From this point on in this discussion, the attention will be directed towards the A_f temperature, which must remain below room temperature to ensure the superelasticity of NiTi. C_pre case exhibited an A_f of -1.7 °C, whereas the AM_pre case demonstrated an A_f of 11.7 °C. However, both cases show an $A_f < T_{room}$. It's noteworthy that in both pre-machining cases, no R-phase, also known as the rhombohedral phase, was observed. This phase, an intermediate state between the austenitic and martensitic crystalline structures, is recognized for its adverse effects on the superelasticity of NiTi.

3.1.2 Microstructural Analysis

The Figure 3.3 displays images captured using an optical microscope, illustrating the microstructures of NiTi samples within the bulk cross-sections. In both scenarios, the microstructures consist of equiaxed B2 cubic austenite grains. From an observation of the images, the AM samples exhibit larger and more irregular grains in contrast to the conventionally manufactured samples. It is important to highlight that the AM samples underwent heat treatment, notably aging at 600°C, resulting in grain size enlargement and the emergence of Ni-rich precipitates. The size of grains significantly impacts the properties of metals, particularly their yield stress. Hall-Petch's law indicates that the yield stress rises with decreasing grain size, as described by the empirical equation:

$$Y = Y_i + kd^{-\frac{1}{2}} \quad (3.1)$$

Where *Yi* is the threshold yield stress, *k* is a constant reflecting the level of dislocation stacking, and *d* denotes the grain size. Larger grains typically correlate with lower mechanical strength, reduced hardness, and increased ductility. With the help of a MATLAB code that implements the intercept method - one of the methods for determining the average equivalent diameter of the grains - the mean values of the grain size and the respective standard deviations found in Table 3.1 have been obtained.

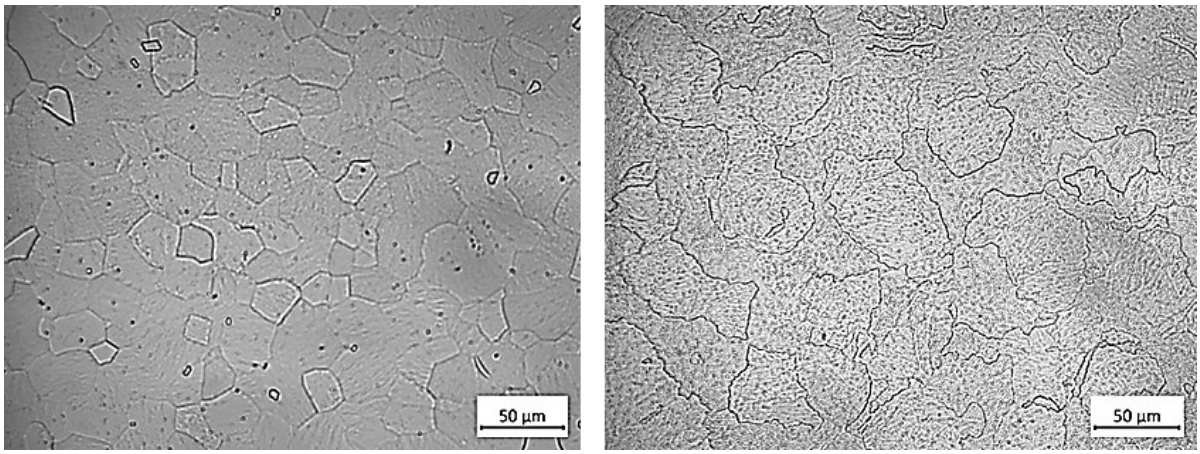

Figure 3.3 Microstructure of C (left) and AM (right) bulk cross-sections.

	Average grain size (µm)	Standard deviation
Conventional	37	19
Additive	66	45

Table 3.1 Average grain size of C and AM.

3.2 Characterization After Machining

3.2.1 Effects Of Cutting Speed

In the subsections following this paragraph, the objective is to draw comparisons between all the conducted measurements, which will be clarified in the next section, emphasizing the influence of two distinct cutting speeds on the two differently manufactured NiTi machining.

3.2.1.1 Tool Wear Characterization

Determining the tool-wear behavior with the respect of time is important for understanding the machining performance of difficult-to-machine work materials. The aim is to control the tool wear process and understand how to reduce its adverse effects that affect both the machining process itself, for example its cost, but also the surface quality of the parts. Tool-wear, as has already been said in the previous chapters, is not an absolute value, but depends on several factors. This research attempts to investigate the impact of employing two distinct cutting speeds on the machining of workpieces manufactured through two different methods. An overview of the experimental plan and adopted notation is given in

Table 3.2 below.

NOTATION	MANUFACTURING METHOD	CUTTING SPEED
C_v50	Conventional manufacturing	50 m/min
C_v80	Conventional manufacturing	80 m/min
AM_v50	Additive manufacturing	50 m/min
AM_v80	Additive manufacturing	80 m/min

Table 3.2 Experimental plan

For the wear analysis of each condition in the plan, a progressive wear measurement was carried out as a test to understand the material's behavior in relation to tool wear. It is important to note that the evolution of adhesive wear is not clearly predictable due to the instability and non-linearity of the process compared to time and space.

In characterizing tool wear based on ISO 3685 standards, nose wear, a form of flank wear occurring at the tool nose region, was selected. This specific wear type, occurring on the tool's flank, was chosen for measurement due to its observed greater contribution to overall process compared to face wear. It represents an adhesive wear mechanism, particularly prevalent in Ni-alloys. To accomplish this task, the conventional manufactured sample was machined at a cutting speed of 50 m/min, with feed and depth of cut parameters set as stated in Table 2.2. Subsequently, a cutting edge life curve was obtained, revealing a trend consistent with literature findings (see Figure 2.18). The cutting edge life curve displayed an initial running-in phase, during which wear advanced rapidly (from 0 to about 1 min), a stationary zone (from 1 to 9 min), and a final segment where it escalated with an accelerated wear rate, leading to the catastrophic failure of tool. It was observed that the end of the tool's life occurred when the maximum length of the flank wear in the nose region (VB_{Cmax}) was around 0.3 mm; therefore, this value was chosen as the maximum life criterion for this and for all subsequent measurements. For the other conditions of the experimental plan, a less detailed cutting edge life curve was chosen for convenience. It was decided to complete all the curves until each condition reached the end of useful life of the tool. The Figure 3.4 shows the above-mentioned cutting edge life curve of the tool selected for the machining of conventional NiTi at a cutting speed of 50 m/min and the fixed tool-life criterion.

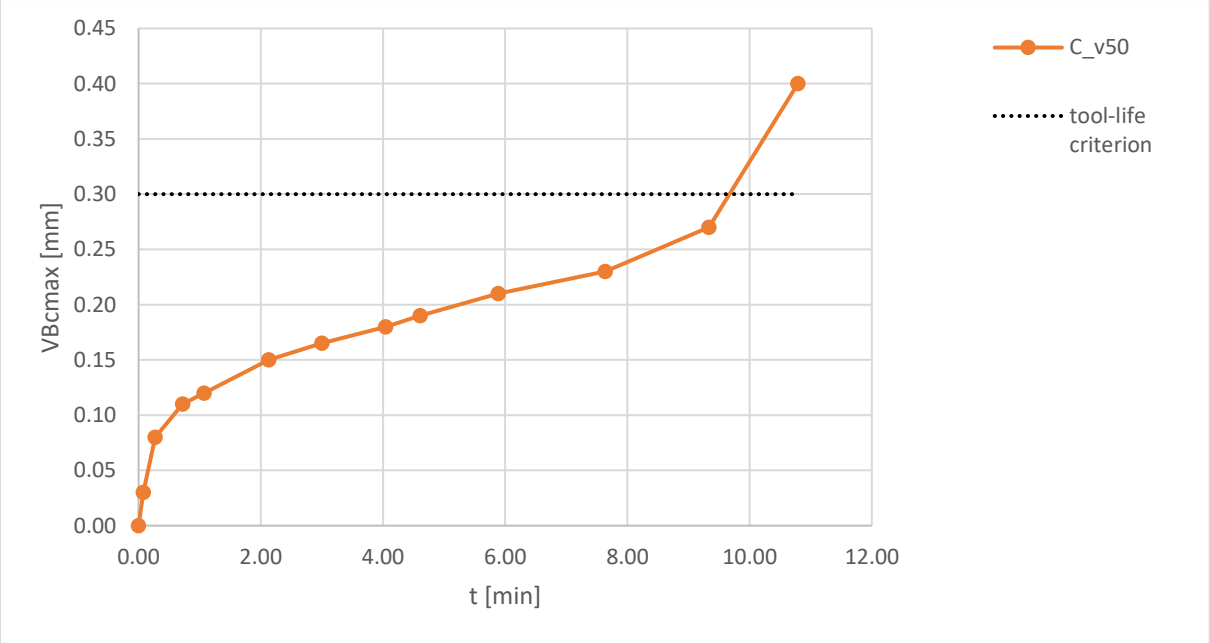

Figure 3.4 Cutting edge life curve.

3.2.1.1.1 Flank Wear

The flank wear is generally quantified in terms of length by VB_B and VB_{Bmax} which are measured outside of the nose radius area, namely in zone B of the cutting edge. Since in finishing operations the depth of cut is normally less than the radius of the tool nose, the maximum flank wear land width measured at the major flank face is not a suitable criterion for evaluating tool life in such applications [16]. When surface finish quality is one of the main concerns, the flank wear land width in the nose area (in zone C) represented by VB_C is a more meaningful parameter for assessing tool life.

Tool-wear rate was periodically measured during progressive experiments, using SEM after variable machining time intervals for each material. The Figure 3.5 illustrates the phenomenon of flank wear on the major cutting edge of the tool, in the first case studied, namely the machining of a conventional manufacturing NiTi with Vc=50 m/min. It has been chosen to report four significant SEM measurements representing respectively the case of minimum wear (w_min), a first intermediate step (w_int1), a second intermediate step (w_int2) and the case of maximum wear (w_max) when the end-of-life criterion has been exceeded.

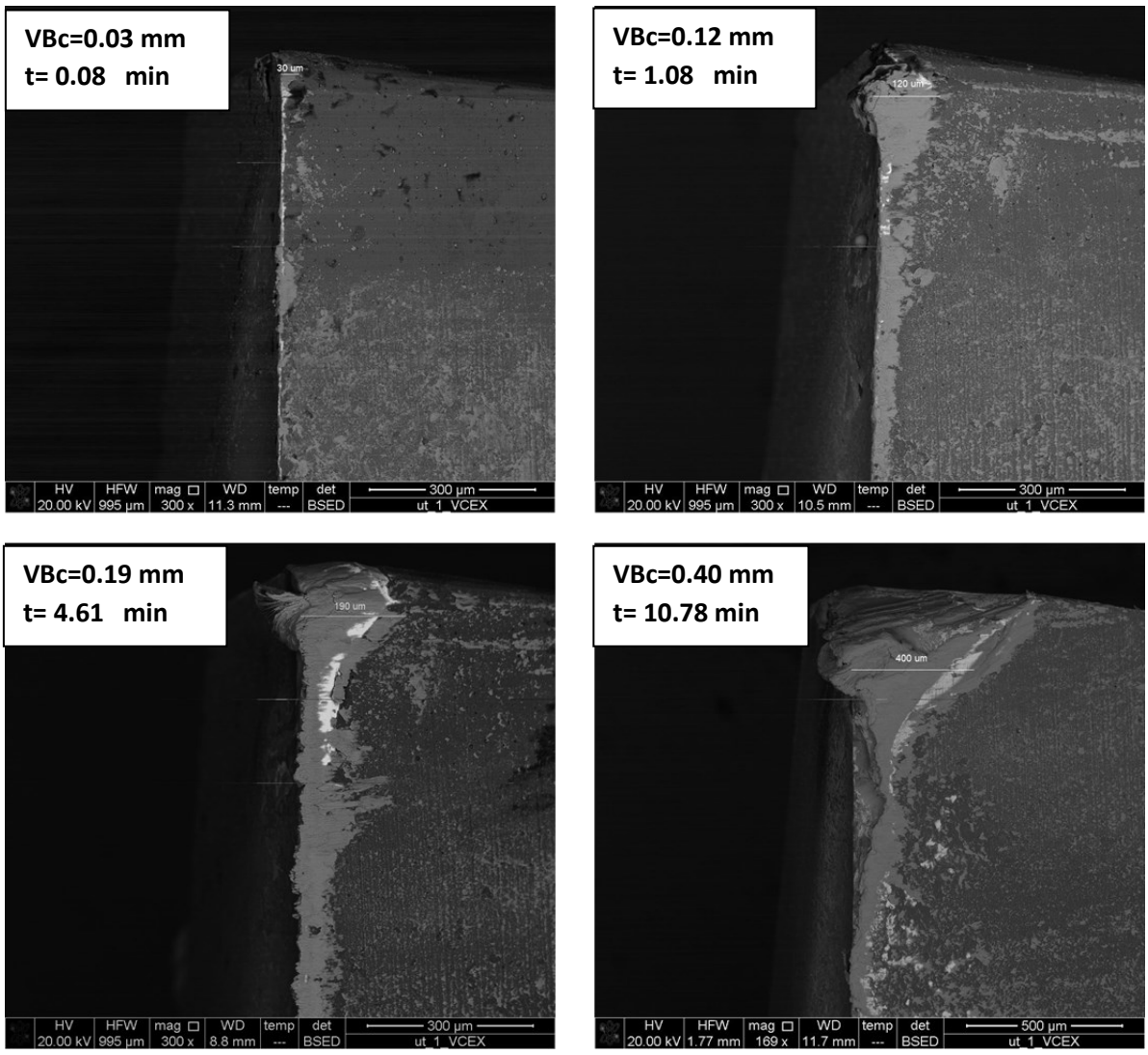

Figure 3.5 SEM images of VBcmax for C_v50 at w_min, w_int1, w_int2 and w_max.

In figure Figure 3.6 the same pattern of representation has been followed, for the case of working of a conventionally manufactured NiTi, at higher speed (v=80 m/min).

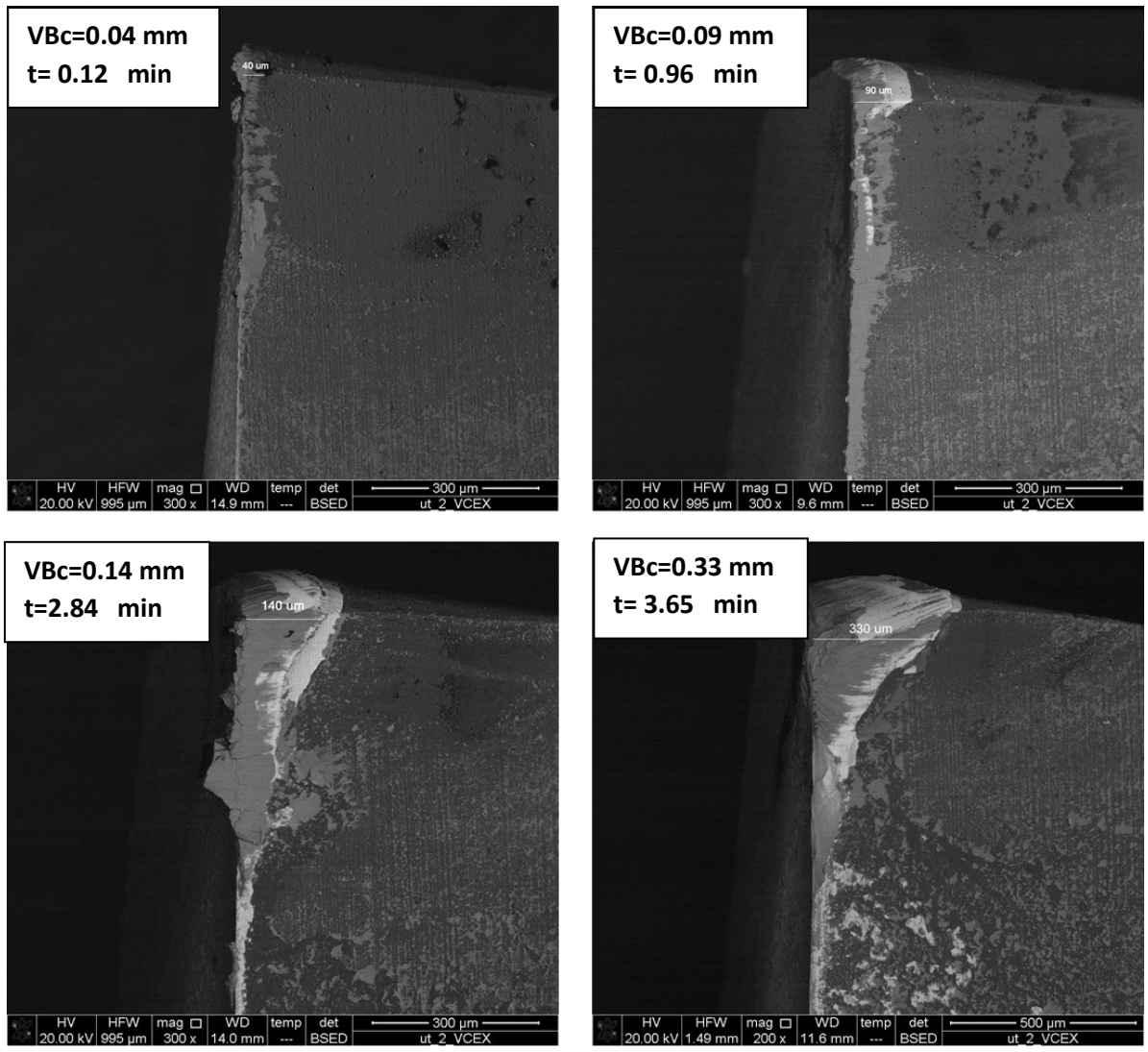

Figure 3.6 SEM images of VBcmax for C_v80 at w_min, w_int1, w_int2 and w_max.

From an observation of the qualitative images just reported, it can be observed that a machining carried out at a speed of 80 m/min leads more quickly to the tool-life limit (VBc=0.3 mm), therefore increasing tool wear. Moreover, a similar wear pattern has been observed also in the analysis to the SEM of the analysis of the tool-wear in the case of AM NiTi.

The measured progression of maximum flank wear at the tool nose region as function of cutting time, by comparing the cutting speed, is shown in Figure 3.7, for conventional NiTi and in Figure 3.8 for AM NiTi.

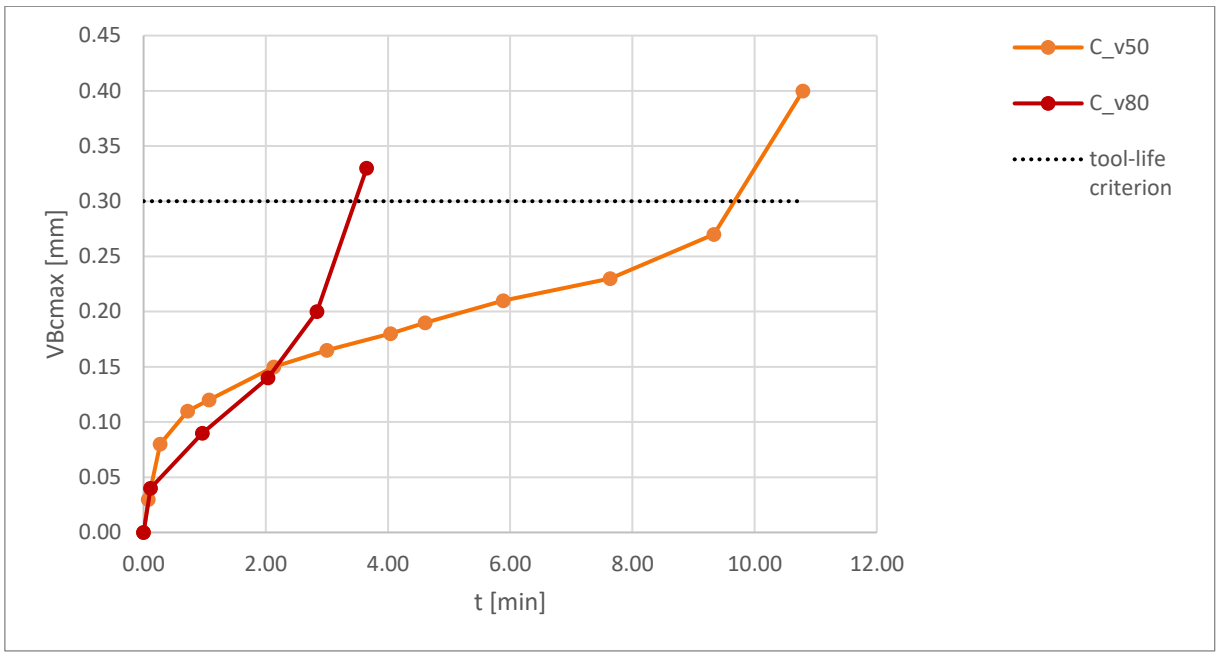

Figure 3.7 Effect of v in VBcmax progression of conventional NiTi.

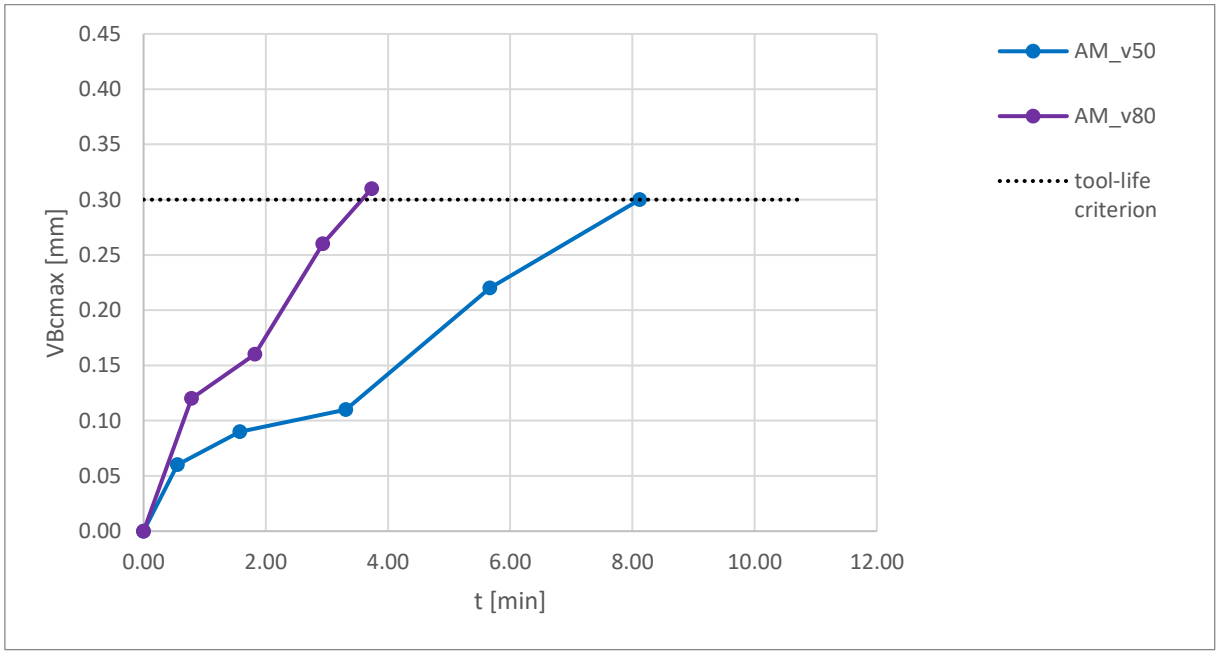

Figure 3.8 Effect of v in VBcmax progression of AM NiTi.

In the first case (Figure 3.7), it is observed that in the initial part of curve, which represents from 0 to 2 minutes of machining, the wear rate in C_v50 case exhibits a steeper slope compared to the C_v80 case. However, this discrepancy is completely lost in subsequent minutes. Notably, the C_v80 reaches the threshold of tool-life shortly after 3 minutes of processing, whereas the C_v50 adheres to the typical pattern of flank wear, reaching its limit around 10 minutes of machining.

In the second graph (Figure 3.8), it is evident that the curve patterns of both cases display an initial phase of accelerated tool wear, followed by a brief stationary period, and subsequently a rapid escalation culminating in tool failure. The primary difference lies in the different slope of the two curves and, consequently, the attainment of the criterion at two distinct machining times: the AM_v50 case exhibits a useful tool-life of about 8 minutes, which is twice the value of tool-life in AM_v80 case.

3.2.1.1.2 Notch Wear and Chip Flow Damage

The notch wear pattern, which normally manifests as a special type of combined face and flank wear beyond the contact zone between the tool and the workpiece as per ISO 3685, has been noted in literature to also occur within the depth of cut boundary when processing Ni alloys. During the study, observations conducted with SEM revealed the presence of this notch wear at the depth of the cutting edge. Among the types of wear is the most severe and has been observed in all the conditions tested, particularly evident during the maximum wear step.

Figure 3.9 illustrates notch wear at the maximum wear step in the case of conventional NiTi machined with a cutting speed of 50m/min. The width of the notch wear is denoted as VB_N, and in this instance, it was measured to be 580 microns. In Figure 3.10, which examines the maximum wear step during processing at 80 m/min, the VB_N value is recorded at 390 microns. Given that the maximum wear step recurs across different cases, it was considered appropriate to assess VB_N at a fixed time, enabling a comparison between the two cutting speeds. A rapid increase in notching often occurs on carbide tools at higher cutting speeds, as highlighted in Figure 3.11, which compares the machining of conventional NiTi at two different speeds, with a processing time of approximately 3 minutes. The latter figure illustrates a pronounced notch extension during machining at higher speeds, as evidenced in the right figure; specifically, VB_N value measures 390 microns, while 140 microns were recorded at the same machining time for the lowest cutting speed case.

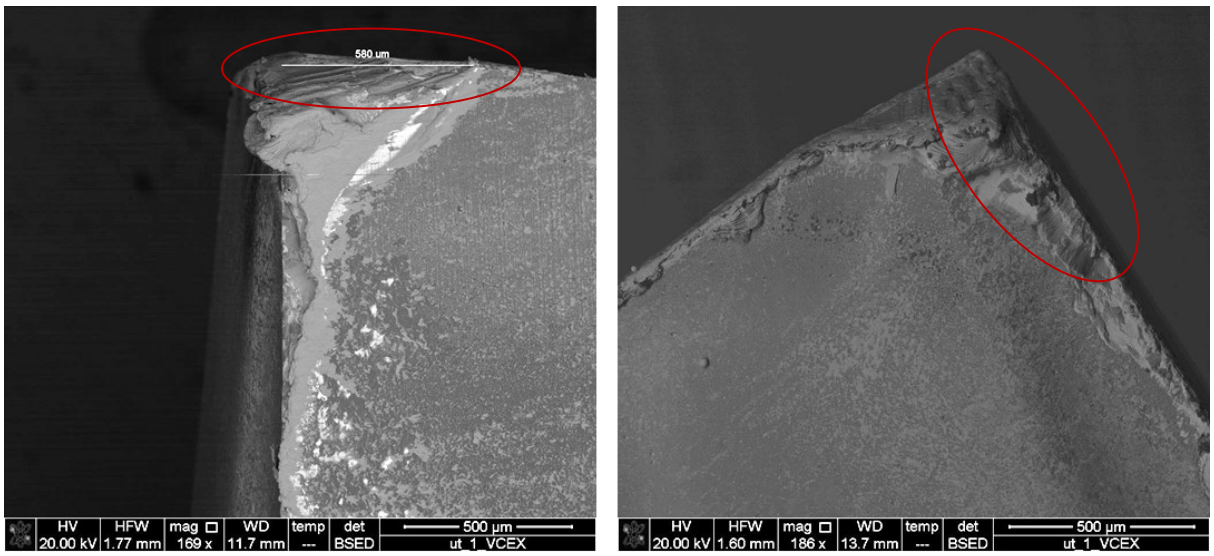

Figure 3.9 Notch wear at C_v50_w_max.

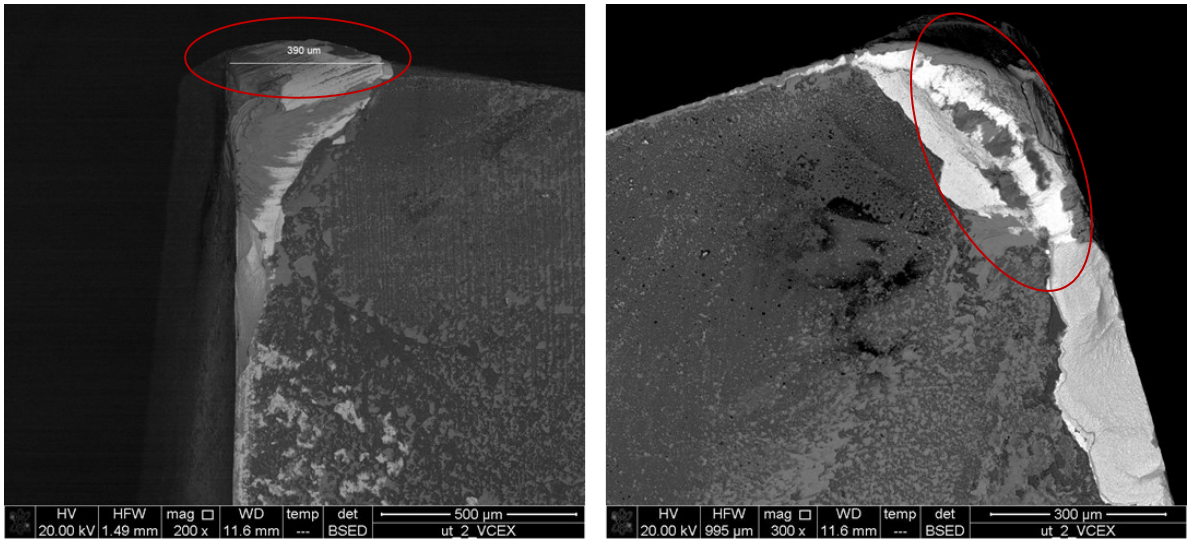

Figure 3.10 Notch wear at C_v80_w_max.

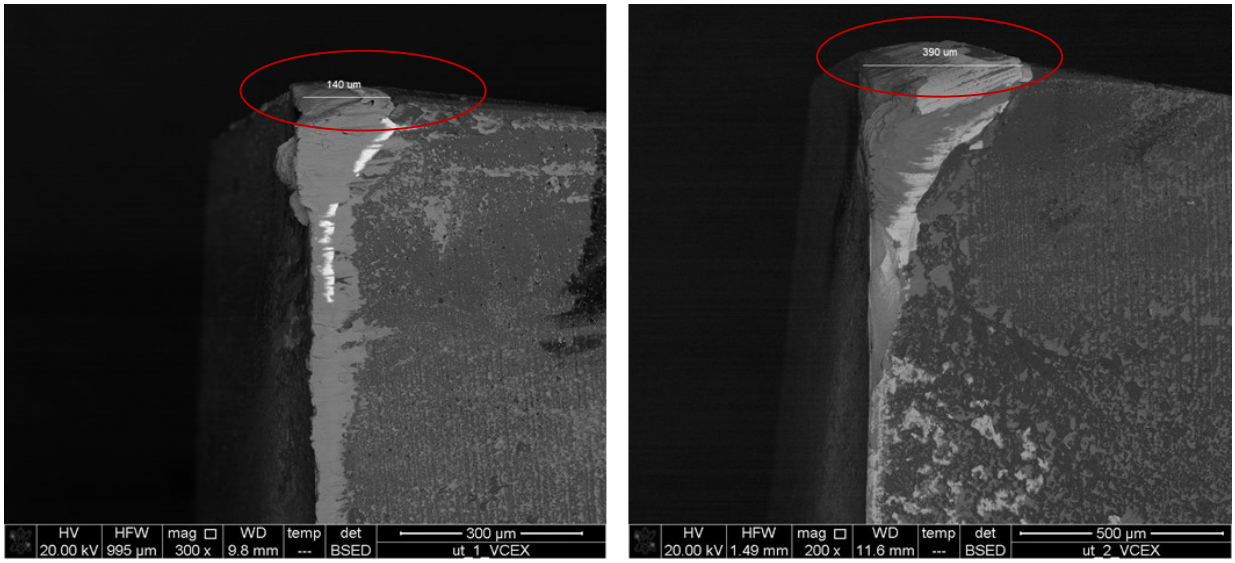

Figure 3.11 Notch wear at C_v50 (left) and C_v80 (right) at t≈3 min.

Chip flow damage is a further problem that is evident in NiTi machining. The Figure 3.12 shows an example of this fractured area in the tool at the level of the main cutting edge, beyond the zone of contact between tool and piece. For short machining times, it has no direct influence on the cutting process, but the more time increases the more it becomes a problem and can be one of the causes of the failure of the tool. Chipping is caused by the instable cutting edge fragment detachment under adhered workpiece material layers that weld onto the tool surfaces since the cutting beginning. This underscores that even the chipping process is initially activated by the adhesive wear mechanism.

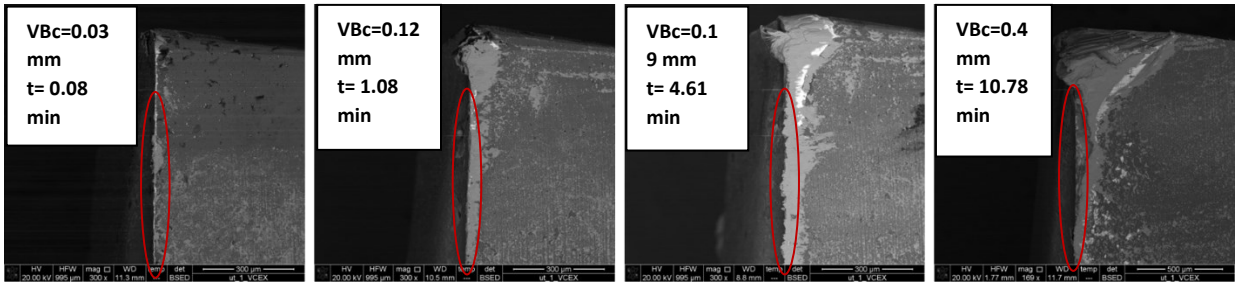

Figure 3.12 Chip flow damage at different machining times for C_v50.

3.2.1.1.3 Crater Wear

An analysis of face wear was also carried out, which showed - as expected - that this type of wear is not significantly occurring during the machining of nickel-based materials. Nevertheless, the most noteworthy images, namely those depicting maximum wear step, are reported for a qualitative comparison between the two cutting speeds employed, for both types of material. These analyses show that there are no visible wear craters.

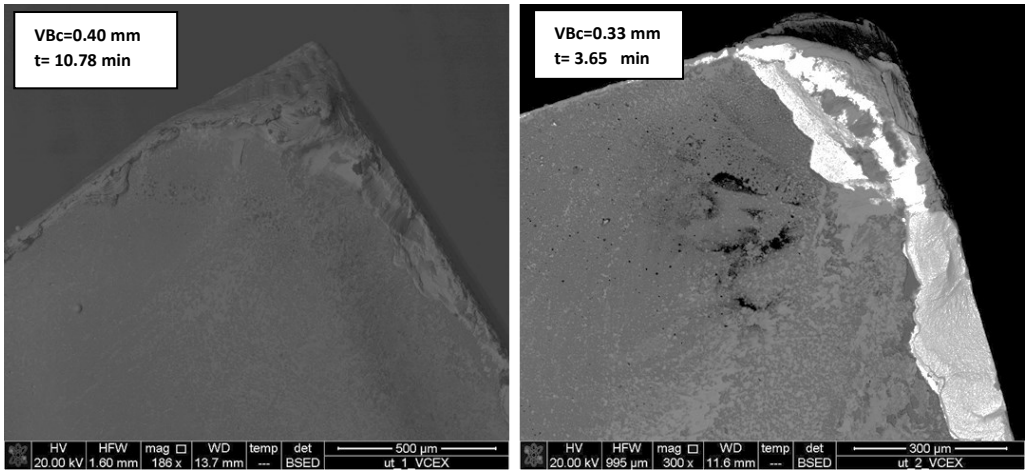

Figure 3.13 Tool face at C_v50_wmax (left) and C_v80_wmax (right).

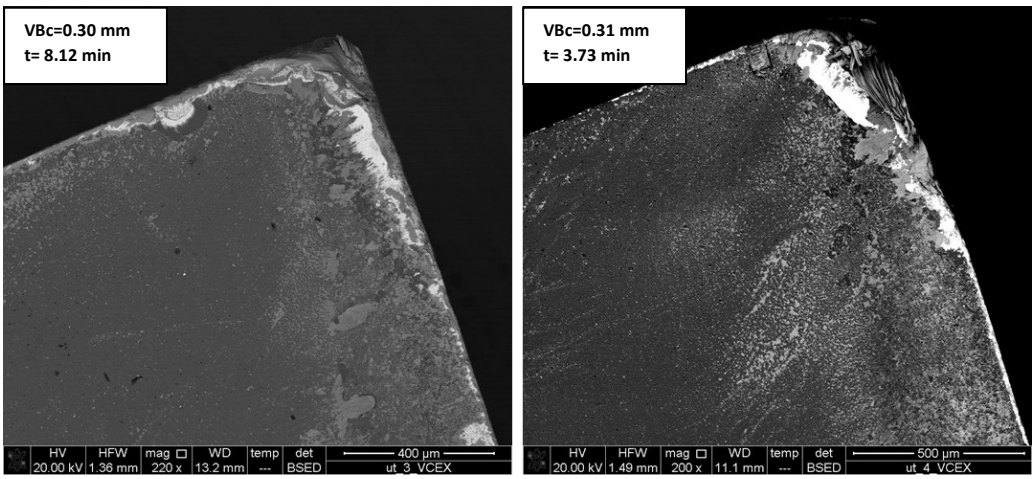

Figure 3.14 Tool face at AM_v50_w_max (left) and AM_v80_w_max (right).

The step-by-step progression of the face wear of the tool is also reported for greater clarity of treatment, in the case of AM NiTi machining at both cutting speeds.

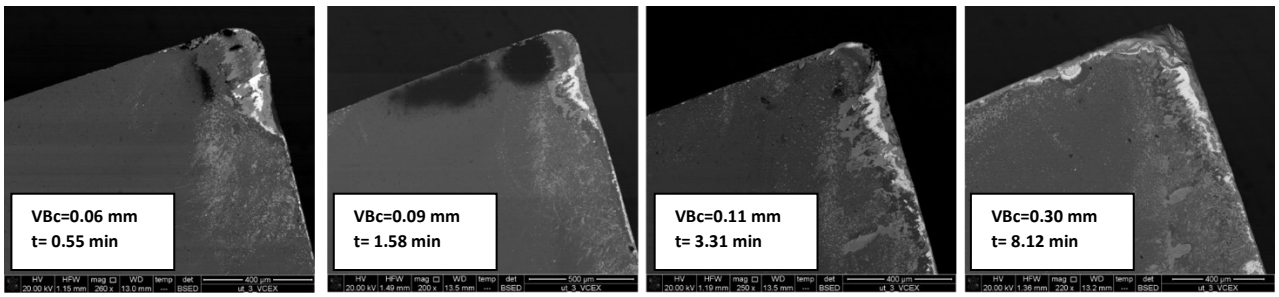

Figure 3.15 Face wear progression for AM_v50.

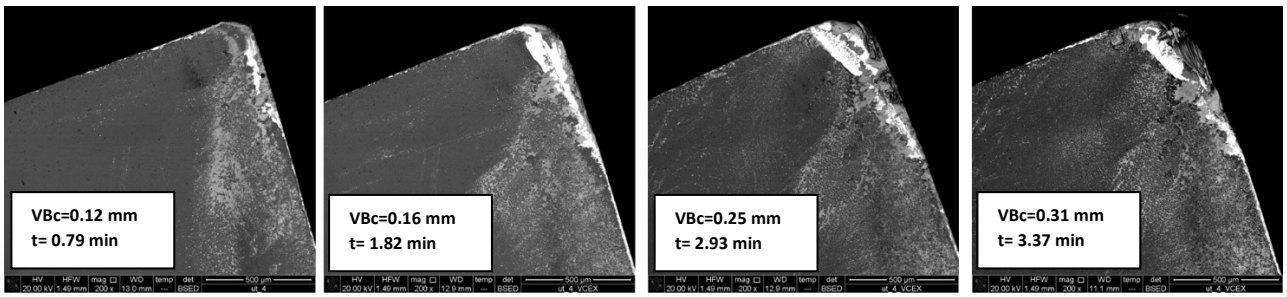

Figure 3.16 Face wear progression for AM_v80.

In addition to the images of the analysis at SEM, the EDS of the tool face were conducted to improve the explanation of the adhesion mechanism occurred during these tests. Figure 3.17 and Figure 3.18 shows the EDS analysis of maximum wear step of C_v50 and C_v80 in comparison to highlight the differences in wear mechanisms as the cutting speed changes.

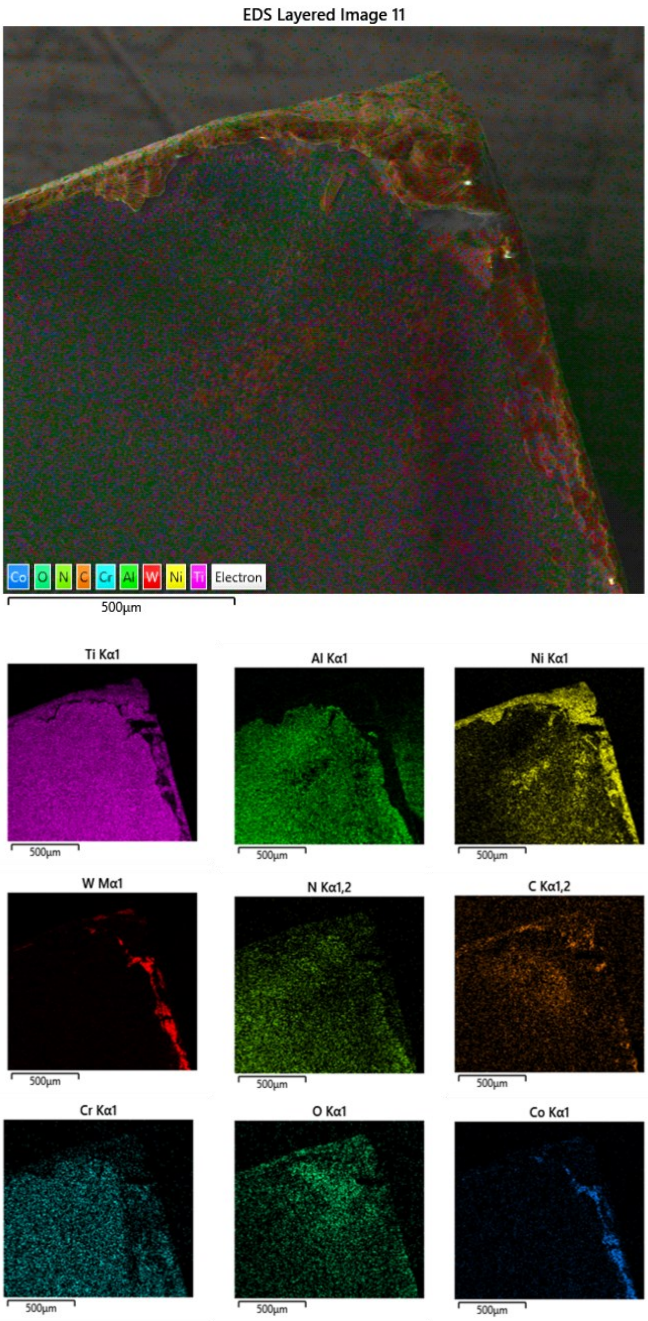

Figure 3.17 EDS of C_v50_w_max.

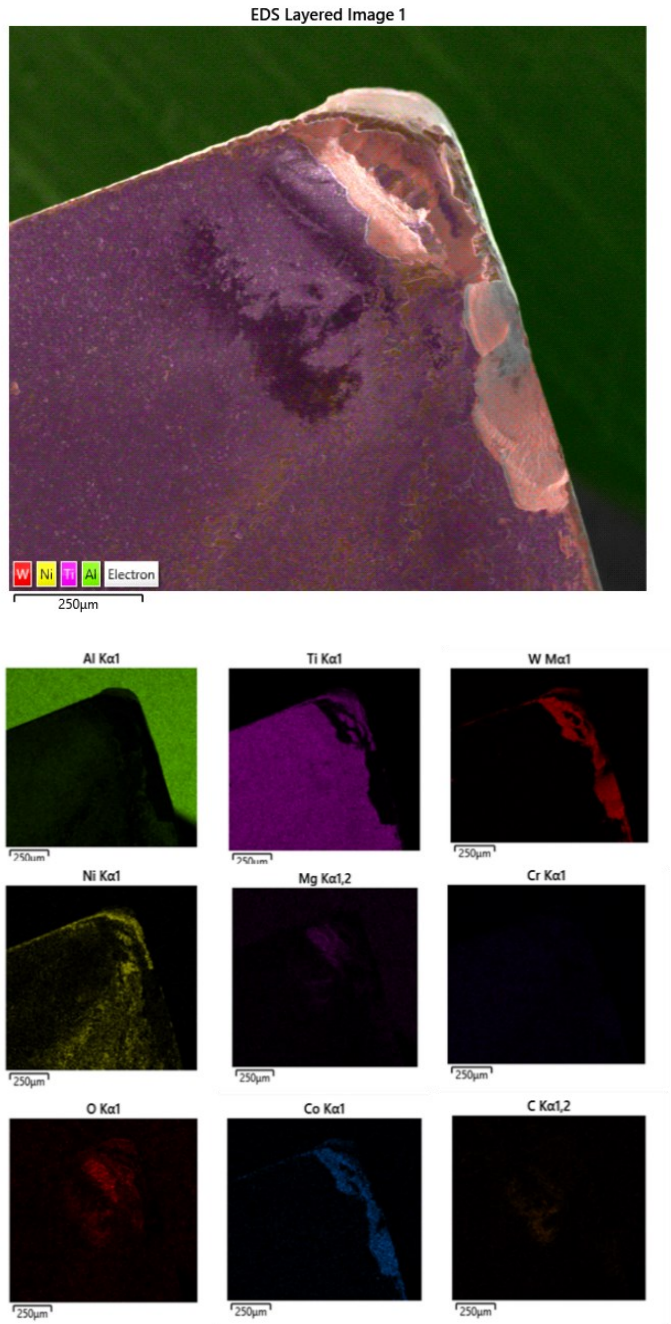

Figure 3.18 EDS of C_v80_w_max.

The EDS results indicate that employing a higher cutting speed leads to less material adhesion on the workpiece compared to processing at lower speeds. This is evident from the higher concentration of nickel (Ni) on the tool face in case of C_v50 compared to C_v80, decreasing from 8 at% to 3 at% (atomic percentage). This discrepancy in Ni concentration reveals the dynamics of the Built-Up Edge (BUE) phenomenon. BUE, a common occurrence in metal cutting, involves the accumulation of material on the cutting surface due to the chemical interaction between the material of the tool and the workpiece at high temperatures and pressures. The connection between cutting speed and BUE formation seems to be the cause of these results. At higher cutting speeds, the high temperatures generated during cutting operations can facilitate better separation of chips from the cutting surface, potentially inhibiting the adhesion of the material to the edge of the tool. On the other hand, lower cutting speeds could facilitate the conditions conducive to BUE formation, as demonstrated by the higher concentration of Ni at C_v50.

3.2.1.2 DSC Analysis

The outcomes of DSC post-machining are presented in this section, aiming to analyze and contrast the impacts on *Af* temperature when varying cutting speed on the machining of the employed materials.

Niti shows the results of DSC performed on conventionally manufactured NiTi samples. It is evident that the transformation temperature *Af* remains relatively stable and similar to that recorded pre-machining, without substantial variation observed both during machining with *Vc*=50 m/min and *Vc* =80 m/min.

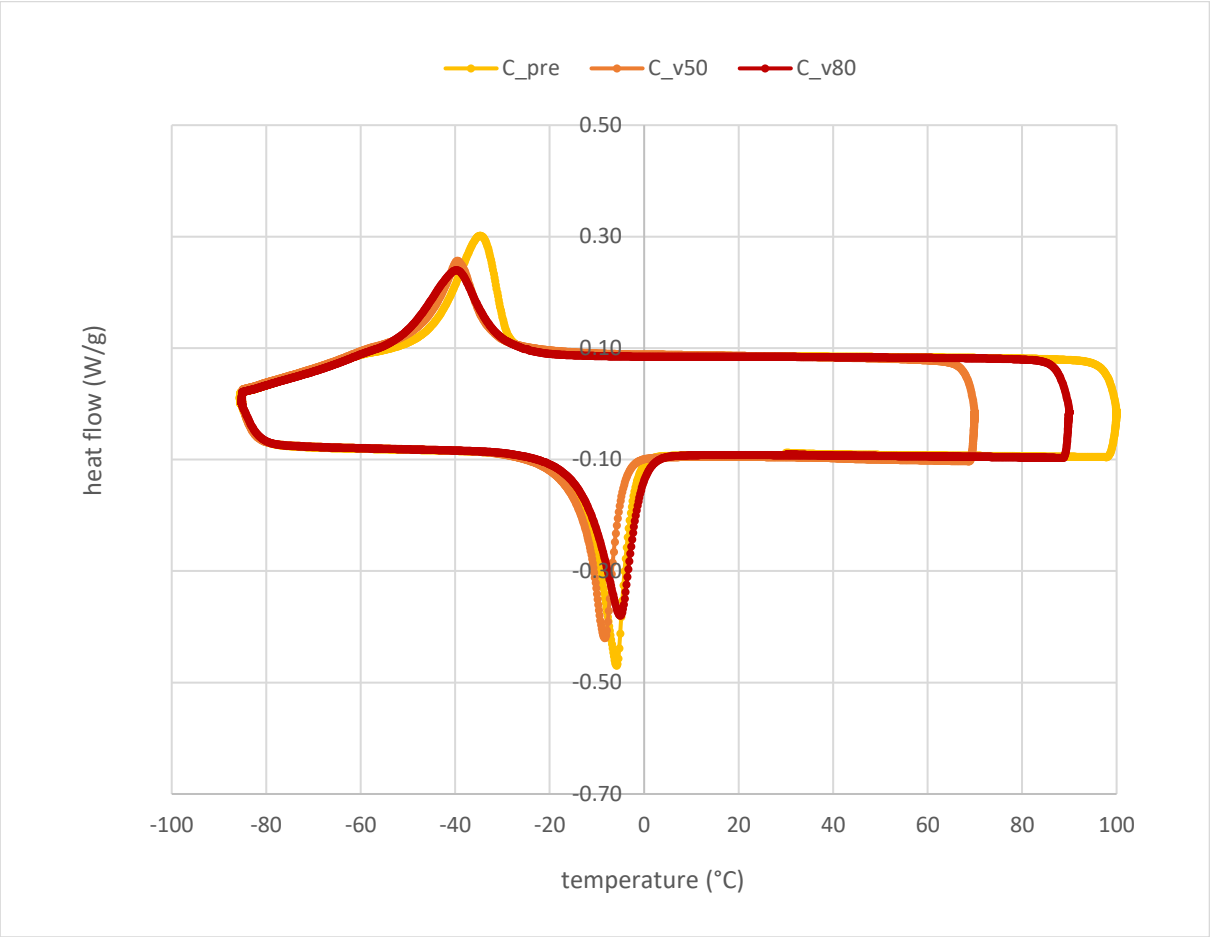

Figure 3.19 DSC conventional NiTi pre and post machining.

On the contrary, there is an evident rise in post-machining *Af* temperature in AM NiTi. However, when employing different cutting speeds, there are no notable distinction, as depicted in Figure 3.20. The phenomenon of *Af* rising can be attributed to the development of martensite phase occurring during machining stages of the additive components. The presence of R-phase in the graph, in data concerning AM post-machining, validates this assertion.

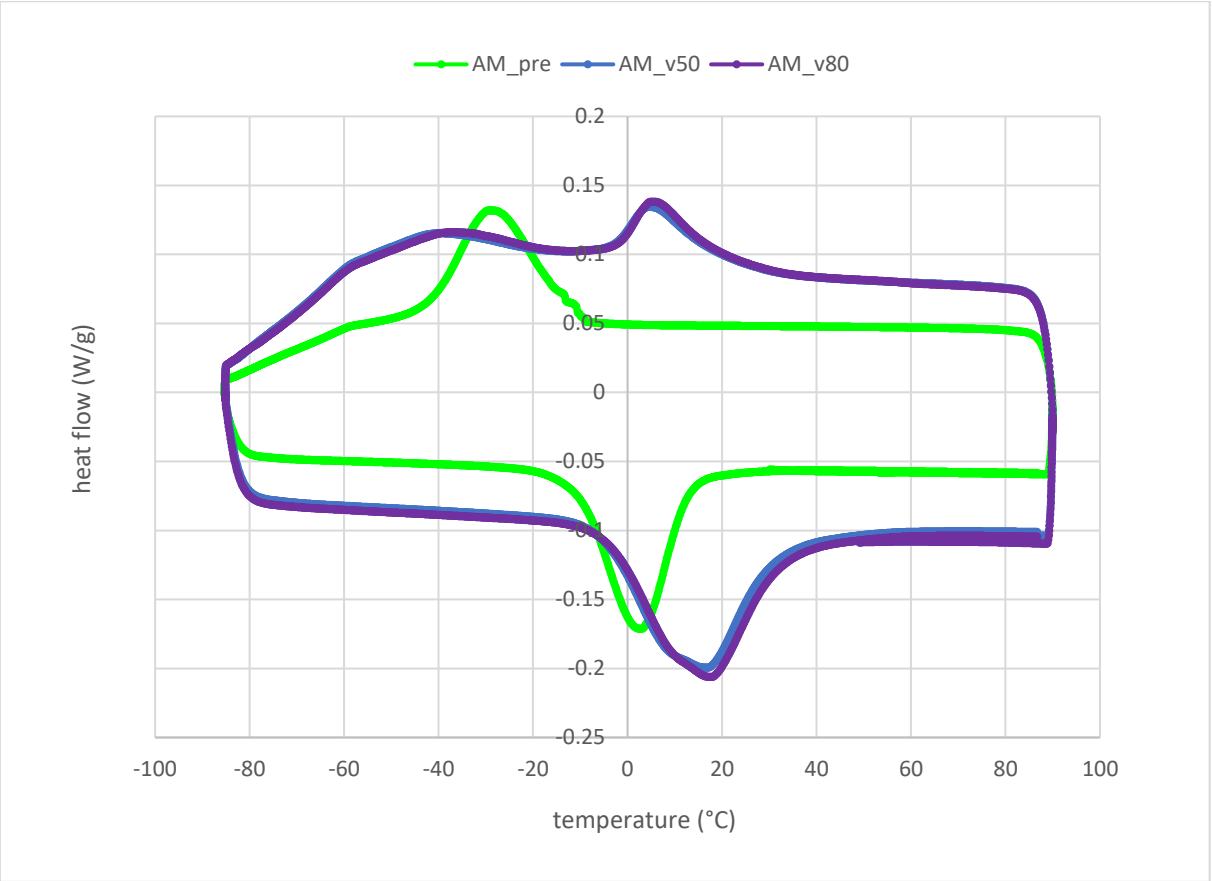

Figure 3.20 DSC additive NiTi pre and post machining.

In the context of the analysis of tool wear and its impacts on SE, a specific investigation of the behavior of the austenitic-martensitic transition temperature, namely *Af*, was conducted. The study involved DSC analysis conducted at both the initial stage of wear, referred to as w_min, and the final stage of maximum wear, denoted as w_max, for each experimental condition outlined in the test plan (see Table 3.2). The outcomes revealed that, in both instances, the *Af* temperature showed an increase after the machining process during the initial phase of wear. Nevertheless, upon reaching the maximum wear stage, a pronounced decrease in temperature *Af* was observed, effectively restoring it to approximately the values documented in the pre-machining phase. No significant differences were found in this trend attributable to shear rate effects, as shown in the Figure 3.21 and Figure 3.22 concerning the data collected in the AM case.

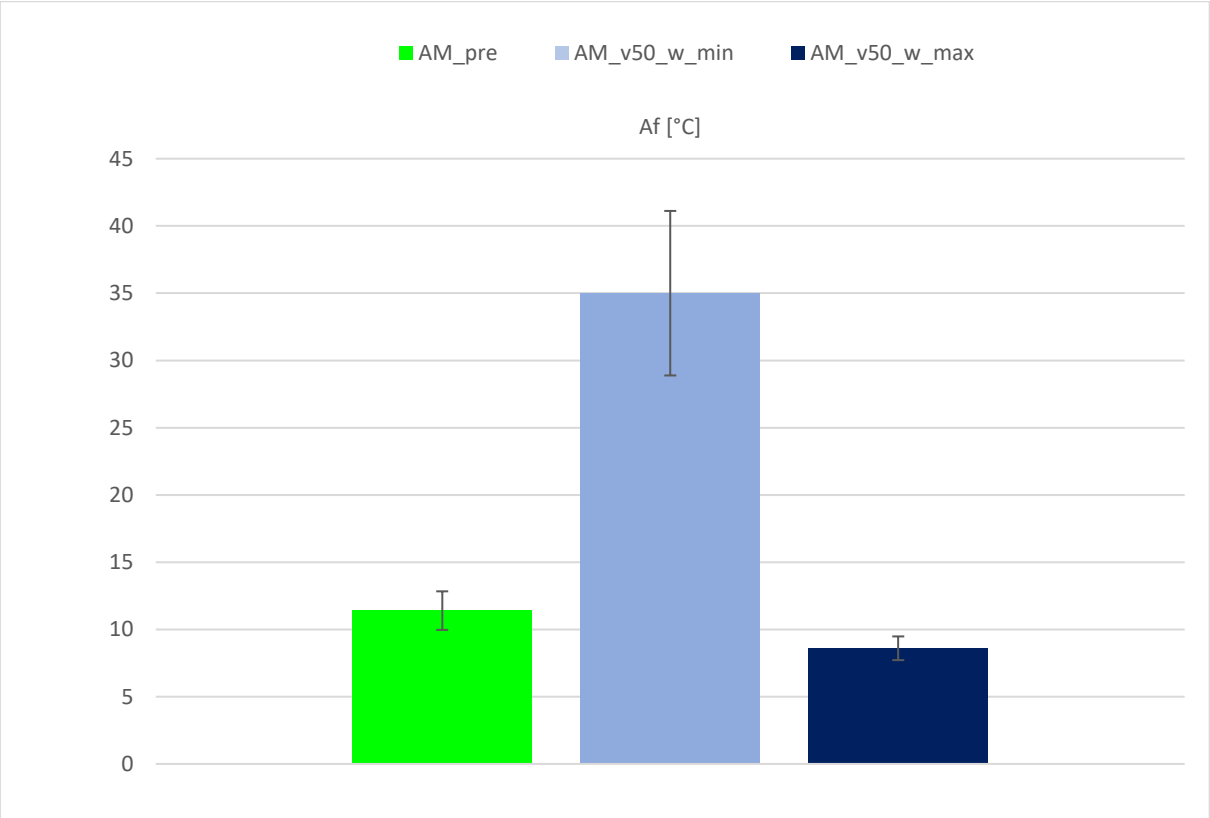

Figure 3.21 Tool-wear effect on Af in AM_v50.

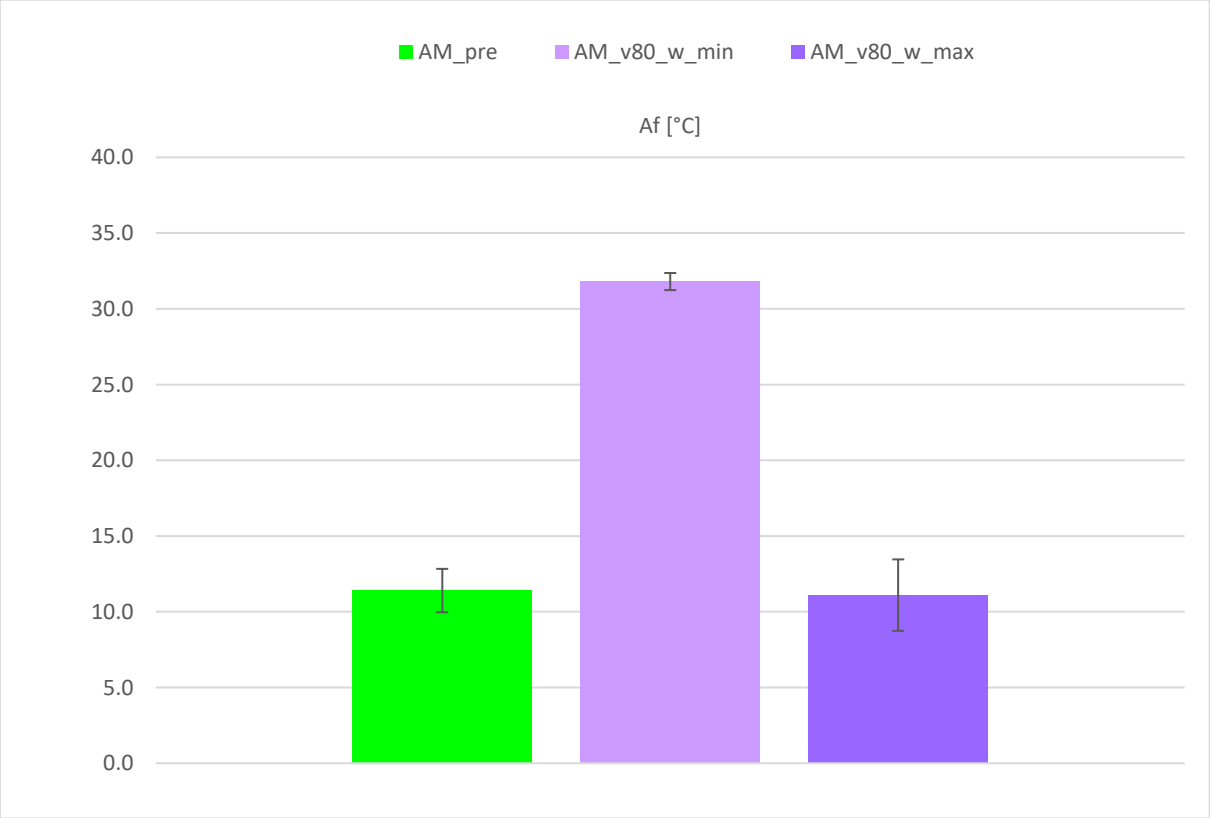

Figure 3.22 Tool-wear effect on Af in AM_v80.

3.2.1.3 Microstructural Analysis

The examination of surface and sub-surface microstructures reveals information about the impact of machining on two different samples. In both areas, a layer of severe plastic deformation (SPD layer) has been observed within each microstructure at 200x magnification. Figures below illustrate the microstructures of the cross-sections of the AM samples, highlighting the effects of two distinct cutting speeds at the points of maximum and minimum wear. Generally, higher cutting speeds correspond to thinner SPD layers, as elevated temperature cycles expose the material to less strain hardening. This trend remained consistent in these results, as depicted in the images below. The two upper images illustrate SPD layers in processing conducted at 50 m/min, while the lower images represent machining at 80 m/min. Furthermore, on the left side, the machining reflects the minimum wear step, whereas on the right side, it corresponds to the maximum wear step. The depth of the severe plastic deformation layer (SPD) in the phase of maximum wear exceeds that of the minimum wear phase. This discrepancy leads to a lack of correlation between the SPD layer and the A_f temperature. This divergence in the depths of the SPD layer suggests that factors beyond temperature A_f influence the formation and extension of the SPD layer. While *Af* temperature traditionally acts as a critical indicator for phase transformation in materials such as NiTi alloys, the presence of a deeper SPD layer in the phase of maximum wear indicates additional complexity. Other variables such as cutting speed, temperature fluctuations during machining and mechanical forces exerted during wear can contribute to the depth and distribution of the SPD layer. Similar observations have been noted in the conventionally manufactured parts. Discrepancies in the formation of the SPD layer based on the material's manufacturing method will be elucidated in § 3.2.2.3.

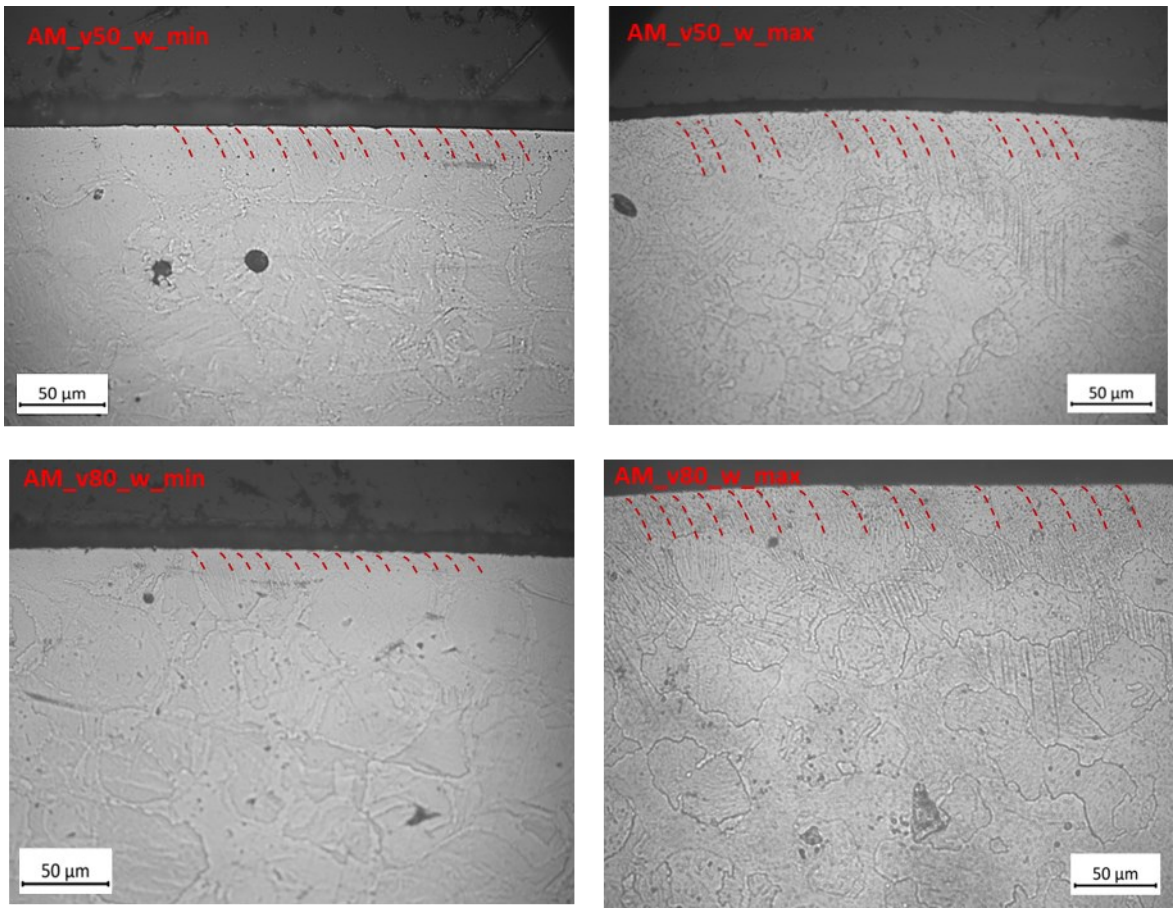

Figure 3.23 Effects on SPD layer of different cutting speeds on an AM NiTi.

3.2.1.4 Roughness Analysis

Wear of a cutting tool is well-known to affect tool life as well as the surface quality of the finished part. As already discussed in § 2.4.4, roughness of the tool is inversely proportional to its tip radius. Adhesive wear on the tool increases its tip radius, so the expected roughness value, *Ra*, should suffer a decrease. However, during the cutting process, as the cutting time increases, the working forces and temperature increase, and roughness also increases, leading to deterioration of the surface finish of the workpiece. Furthermore, the temperature sensitivity of the workpiece and its dynamic elastic modulus cause local vibrations on the machined surface that affect the measurement.

The measurement of *Ra* was made by averaging the values of six profiles obtained through profiling. The Figure 3.24 and Figure 3.25 show the results obtained from the examination of components manufactured through conventional (C) and additive methods (AM), respectively. The aim was to assess the effects on surface finish of using two different cutting speeds in turning at the level of the minimum wear step and the maximum wear step.

The average values obtained for case C are given in Table 3.3.

	Ra_C (µm)	
Vc (m/min)	w_min	w_max
50	0.37 ± 0.009	0.9 ± 0.05
80	0.39 ± 0.02	0.5 ± 0.02

Table 3.3 Ra values after machining with different cutting speeds in Conventional NiTi

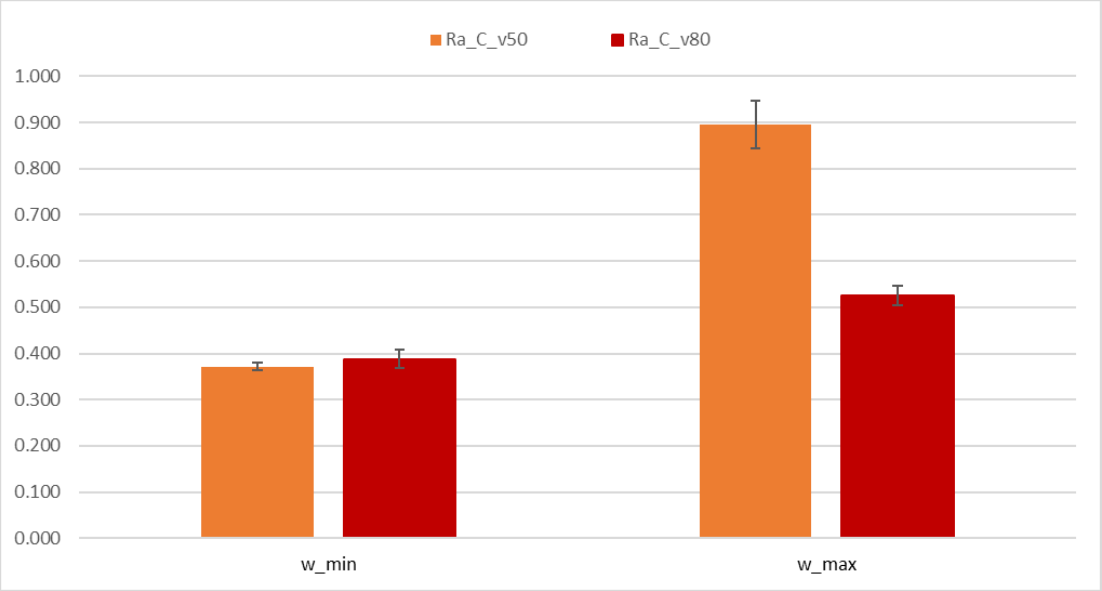

Figure 3.24 Effects of cutting speed on C NiTi Ra.

Comparing v50 and v80 cutting speeds (see Figure 3.24) it is evident that the increased speed v80 reduces by 45% the roughness of the final stage of wear (w_max).

The average values obtained for case AM are given in Table 3.4.

	Ra_AM (µm)	
Vc (m/min)	w_min	w_max
50	0.2 ± 0.004	0.2 ± 0.02
80	0.3 ± 0.01	0.24± 0.02

Table 3.4 Ra values after machining with different cutting speeds in AM NiTi.

In this case no significative differences are evident in terms of employing different cutting speeds.

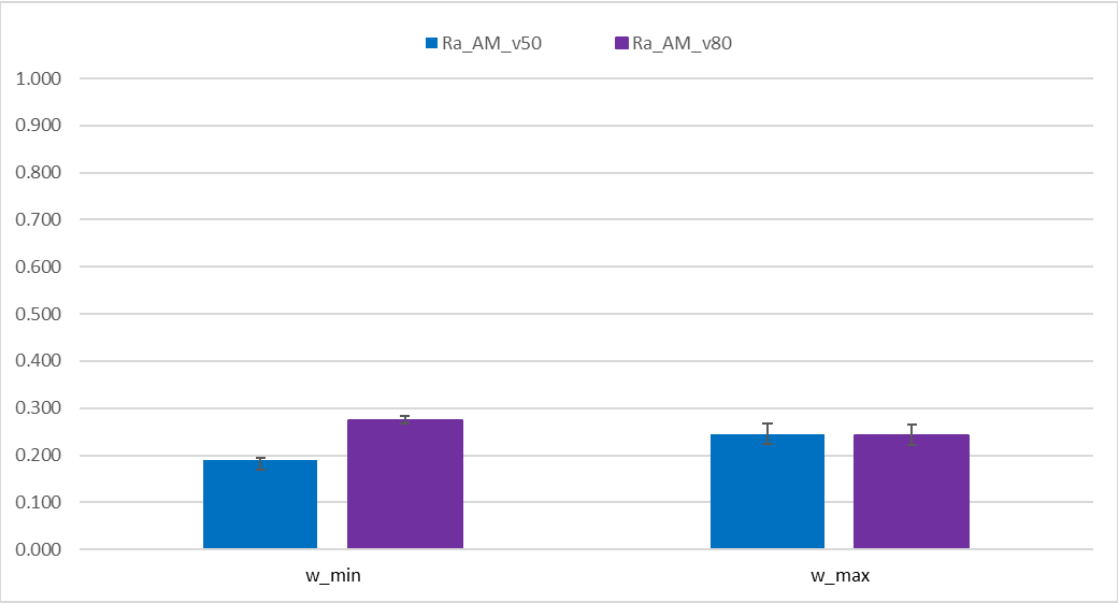

Figure 3.25 Effect of cutting speed on AM NiTi Ra.

The assessment of Ra at various wear stages involves establishing correlations with SEM images of tool face, as can be seen in Figure 3.26. It has been observed that an increase in roughness occur, resulting in deterioration in the workpiece's surface quality, when there's a detachment of the workpiece material previously adhered to the tool. This tendency was notably pronounced with conventionally manufactured materials machined at higher speed (v=80 m/min). During intermediate stages the *Ra* value decreased, on the contrary, during the maximum stage of wear, characterized by a decreased adhesion phenomenon (as affirmed by EDS analysis shown in Figure 3.18), an increase in the *Ra* value was recorded.

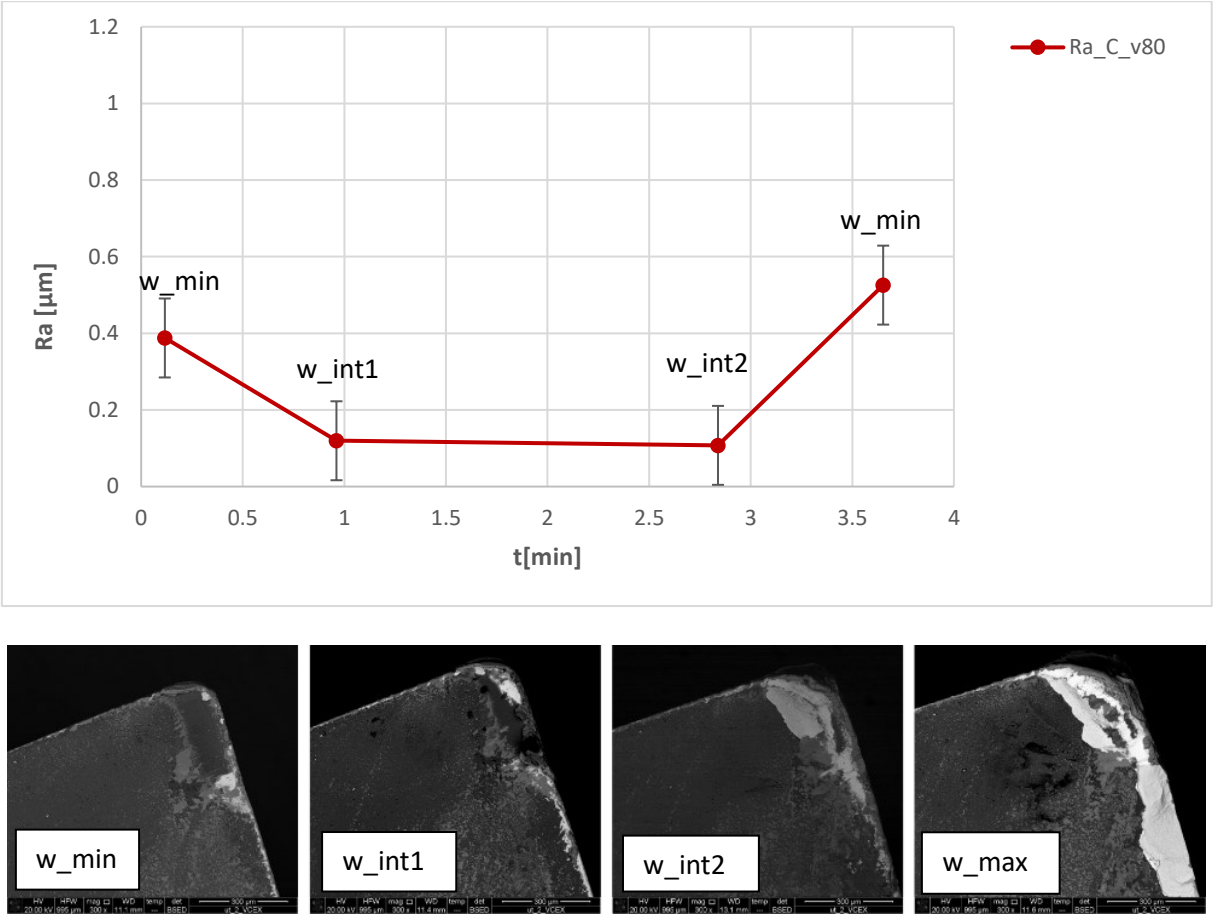

Figure 3.26 Correlation between Ra and face wear in C_v80 case.

3.2.1.5 Machining Forces Analysis

It is known that in a progressive tool wear measurement the generated force components increase as the tool becomes worn. This phenomenon occurs due to the heightened dissipation of energy throughout the machining process. Data obtained from the piezoelectric dynamometer confirm that employing a higher cutting speed in all examined scenarios amplifies the magnitude of all generated force components within the initial minute of machining. This trend is visibly illustrated in Figure 3.27, Figure 3.28, and Figure 3.29 depicting the force components of a conventional NiTi machining, where the steepest curve corresponds to the machining conducted at 80 m/min, and the less steep curve represents the employing of a 50 m/min cutting speed. The variation of the Fz component, namely the feed force Ft, demonstrates this trend clearly, compared to the other two force components.

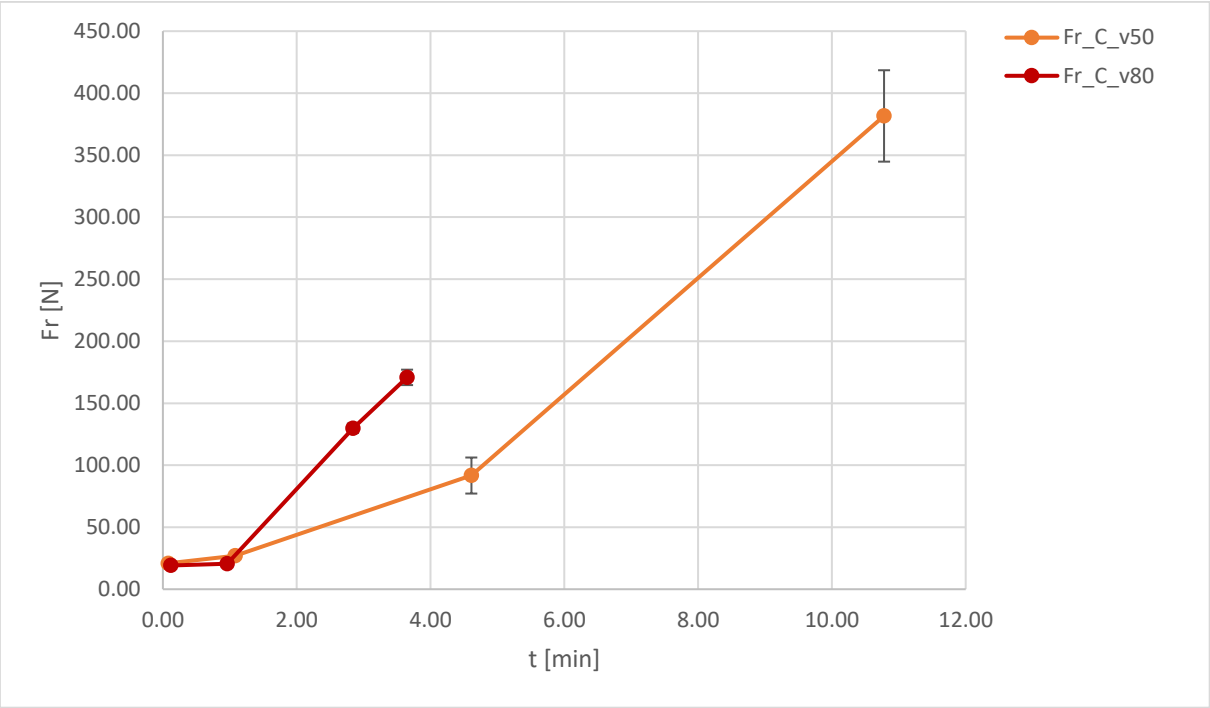

Figure 3.27 Variation of radial force over time for C_v50 and C_v80.

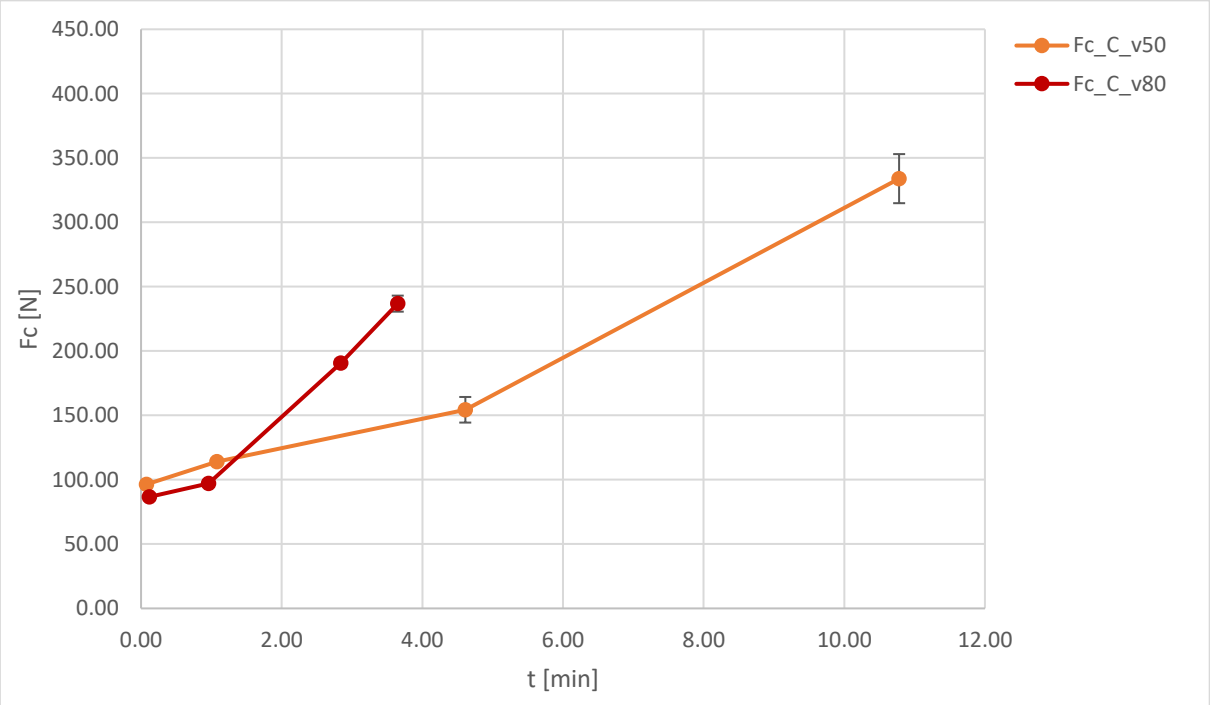

Figure 3.28 Variation of cutting force over time for C_v50 and C_v80.

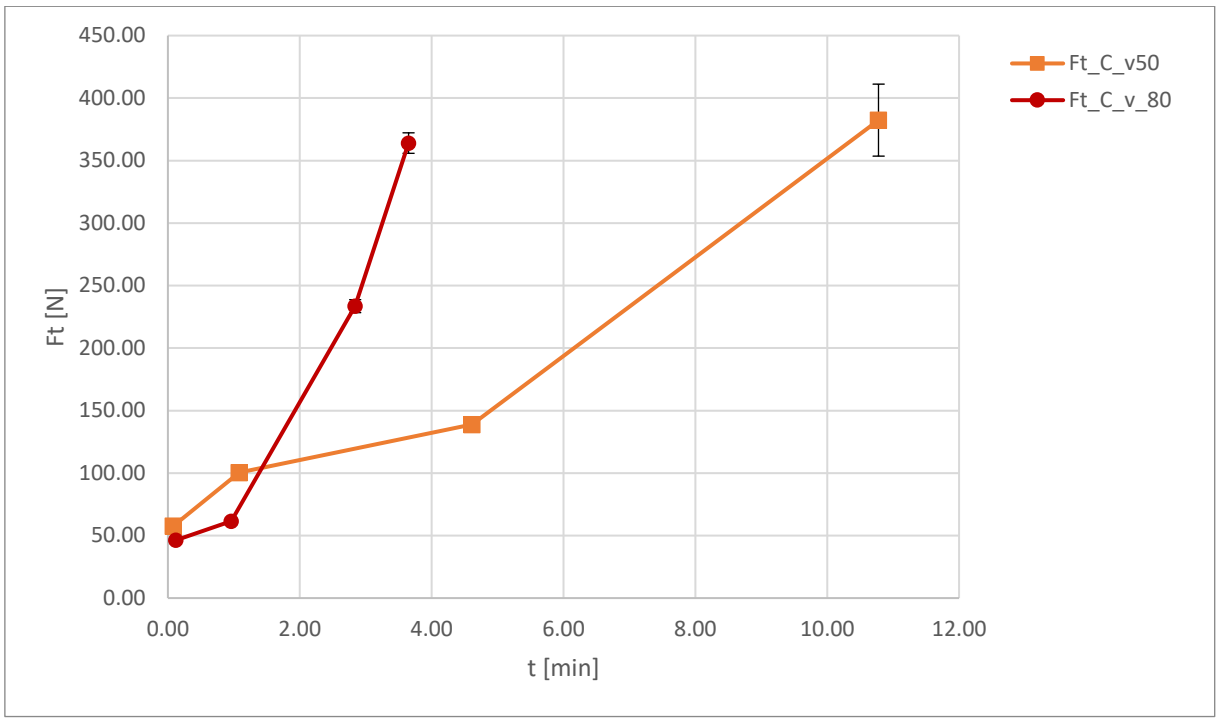

Figure 3.29 Variation of feed force over time for C_v50 and C_v80.

3.2.2 Effects Of Manufacturing Method

In subsections of this paragraph, the objective is to conduct comparison across all measurements, aiming to highlight the effects of two different NiTi fabrication methods, namely conventional and additive manufacturing on tool wear and machinability in general.

3.2.2.1 Tool wear Characterization

The starting assumption is the same as stated in § 3.2.1.1

3.2.2.1.1 Flank Wear

The SEM images depicted in Figure 3.30 illustrate the evolution of flank wear in the nose region for the C_v80 case, drawing a first qualitative comparison with the AM_v80 case, in Figure 3.31. No significant differences in flank wear morphology were detected, when comparing manufacturing methods.

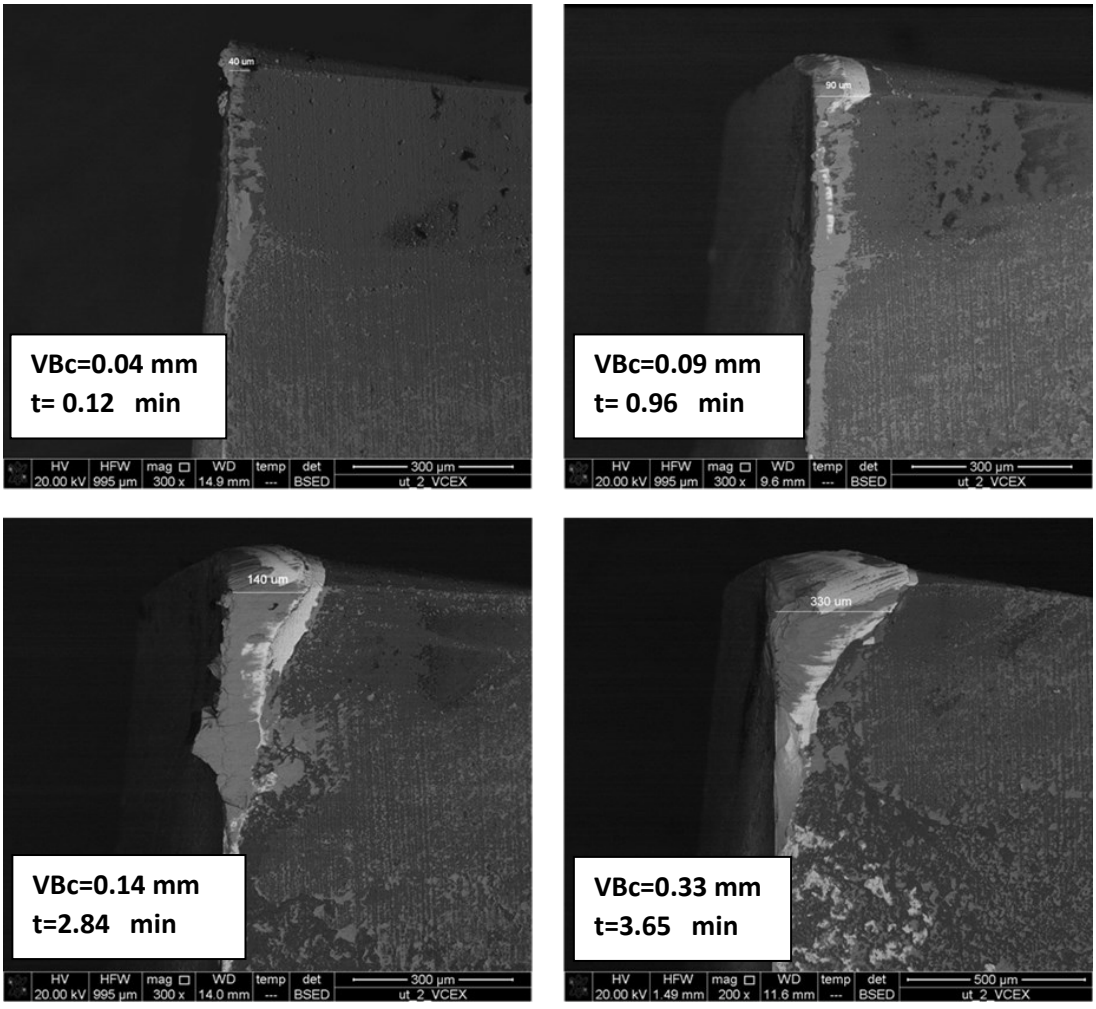

Figure 3.30 SEM images of VBcmax for C_v80.

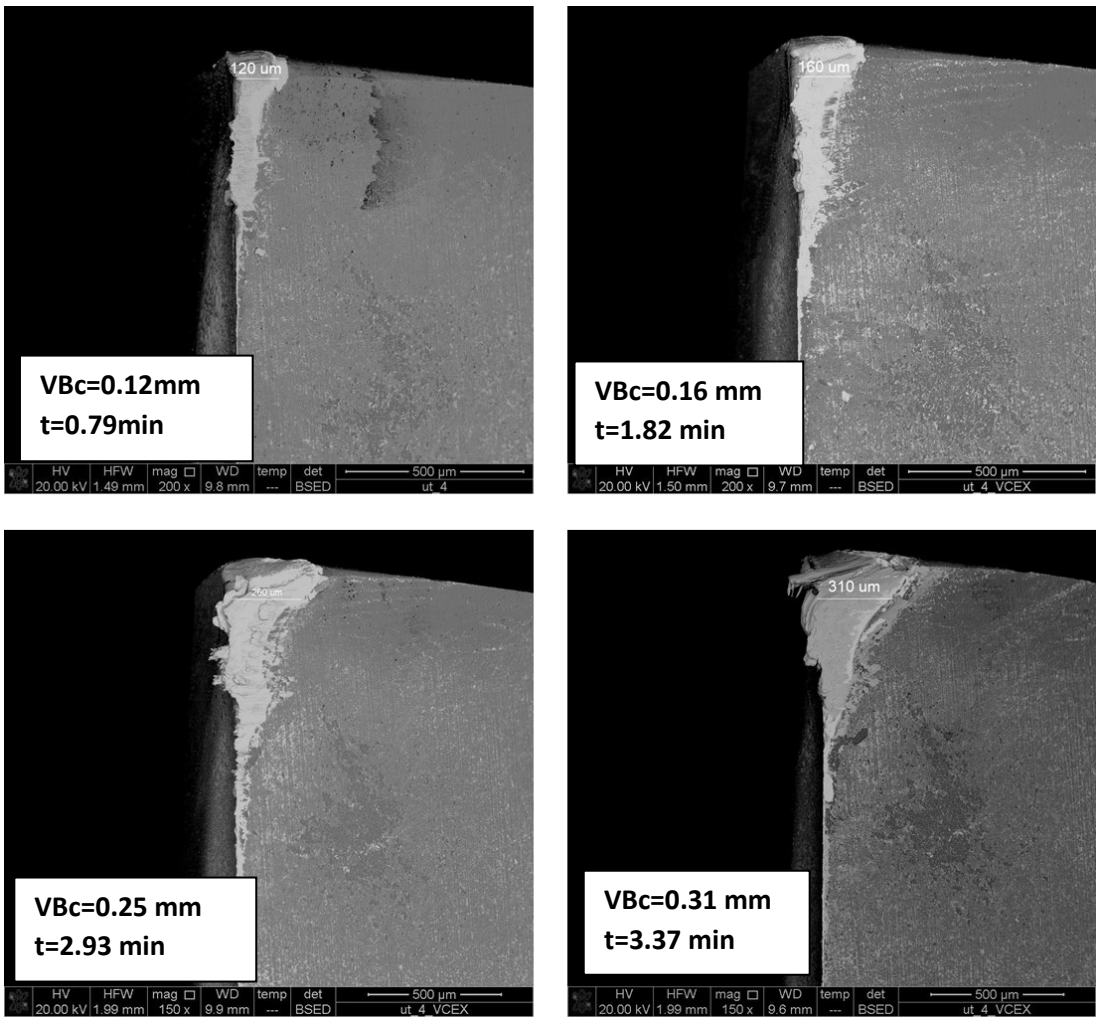

Figure 3.31 SEM images of VBcmax for AM_v80.

Graphs below illustrate a more detailed comparison of progressive wear at constant speed and variable material.

In Figure 3.32, it is observed that, within the first two zones of the curve, namely the phase of break-in and the stationary phase, the AM NiTi exhibits a more mitigated effect of tool wear in contrast to conventional manufacturing case. However, in AM_v50 case, the curve experiences a rapid acceleration in wear rate, after the first five minutes of machining, leading more quickly to the tool's end of life criterion.

Figure 3.33 provides a comparison between the two manufacturing methods in machining processes at speeds of 80 m/min, revealing nearly identical behavior.

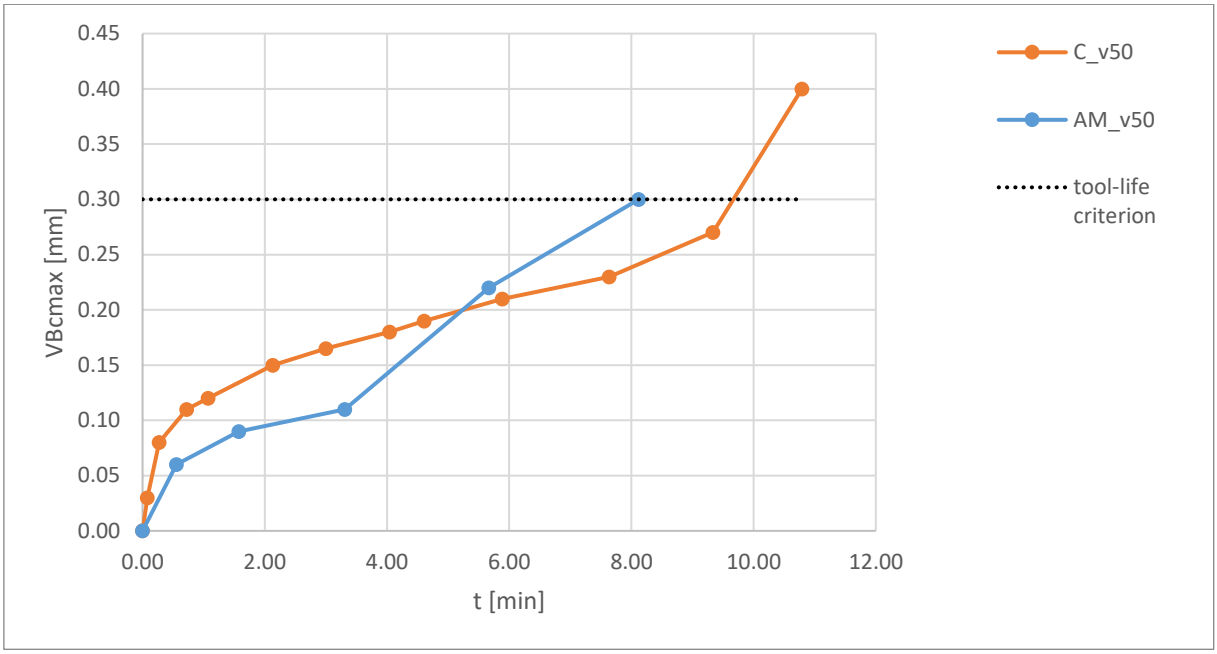

Figure 3.32 Effect of manufacturing in VBcmax progression with v=50 min.

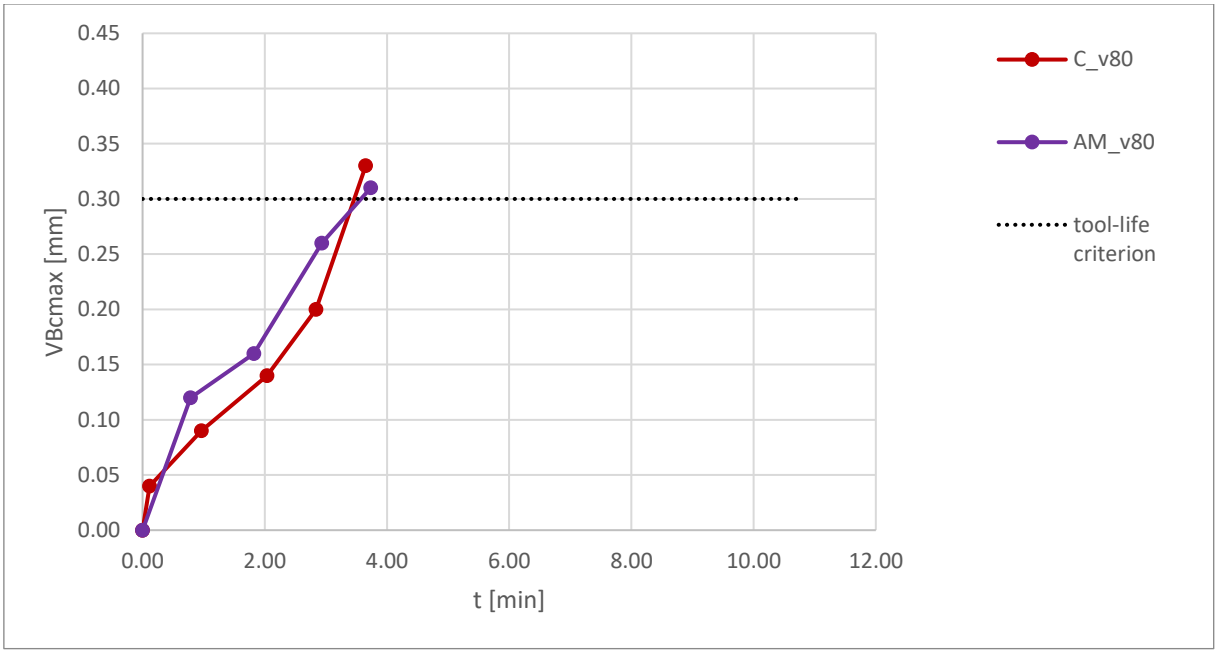

Figure 3.33 Effect of manufacturing in VBcmax progression with v=80 min.

3.2.2.1.2 Notch wear and Chipping

Notch wear and chipping of cutting edge are equally present in both conventional and additive manufacturing, as can be seen from the figures representing the maximum wear steps in which the criterion is reached, presented in previous sections. The SEM analysis therefore shows that these two types of wear appear to depend only on the cutting speed, as already seen in § 3.2.1.1.2.

3.2.2.1.3 Crater Wear

A confrontation of the progressive crater wear was conducted from a qualitative analysis to the SEM of the tool face, with same cutting speed and varying manufacturing method. It turns out that additive manufacturing slightly mitigates the formation of wear craters, especially during the initial stage of analysis, i.e. in the first minutes of processing, as shown in Figure 3.34 and Figure 3.35. The text box accompanying the images displays the machining time and the corresponding previously measured VBc value on the tool flank face, serving as an indicator of the reported wear step.

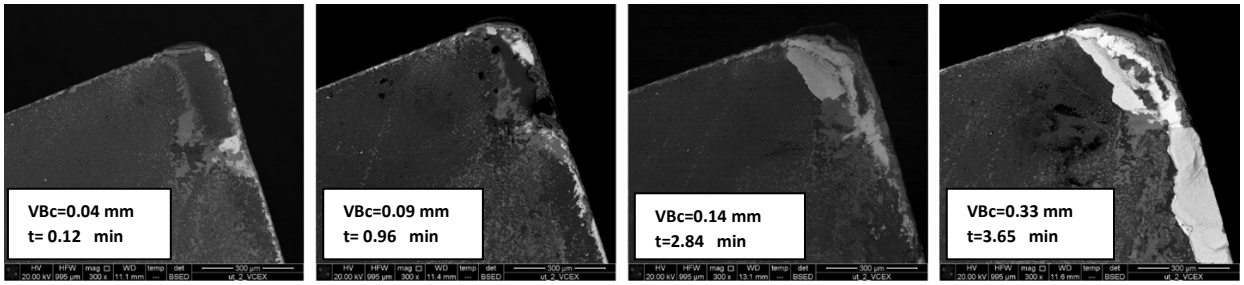

Figure 3.34 Crater wear progression in C_v80.

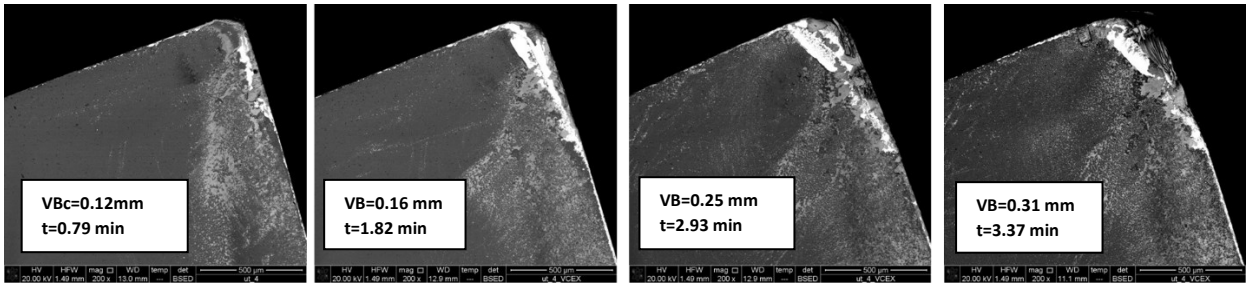

Figure 3.35 Crater wear progression in AM_v80.

An EDS analysis was also carried out to compare the maximum wear of the rake face tool according to the different manufacturing method. Figure 3.36 shows the EDS images of the AM_v80 case that must be compared with those in Figure 3.18, in which the C_v80 case is present. Differences in the pattern of wear attributable to the use of a different manufacturing method are not observed. Even the recorded at% of Ni, W and Co are almost equivalent.

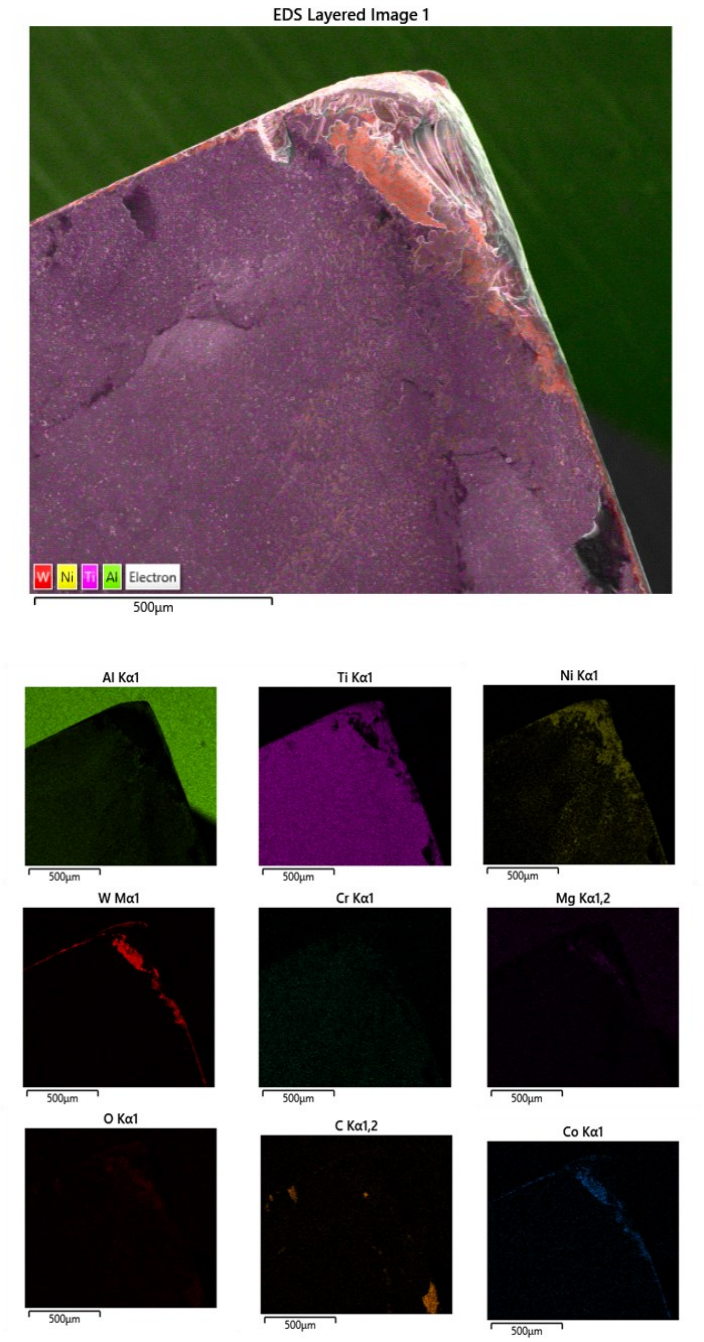

Figure 3.36 EDS of AM_v80_w_max.

3.2.2.2 DSC Analysis

Having examined the analysis in § 3.2.1.2, which explored variations using different cutting speeds, the focus now shifts in emphasizing distinctions between the wrought manufacturing approach and the additive method. It is evident that the transformation temperature (A_f) remains relatively stable in the former. Conversely, in the latter, a noticeable increase is observed, especially when the processing is conducted at a cutting speed of v50, resulting in a 90% rise in A_f between pre- and post-machining stages (see Figure 3.37).

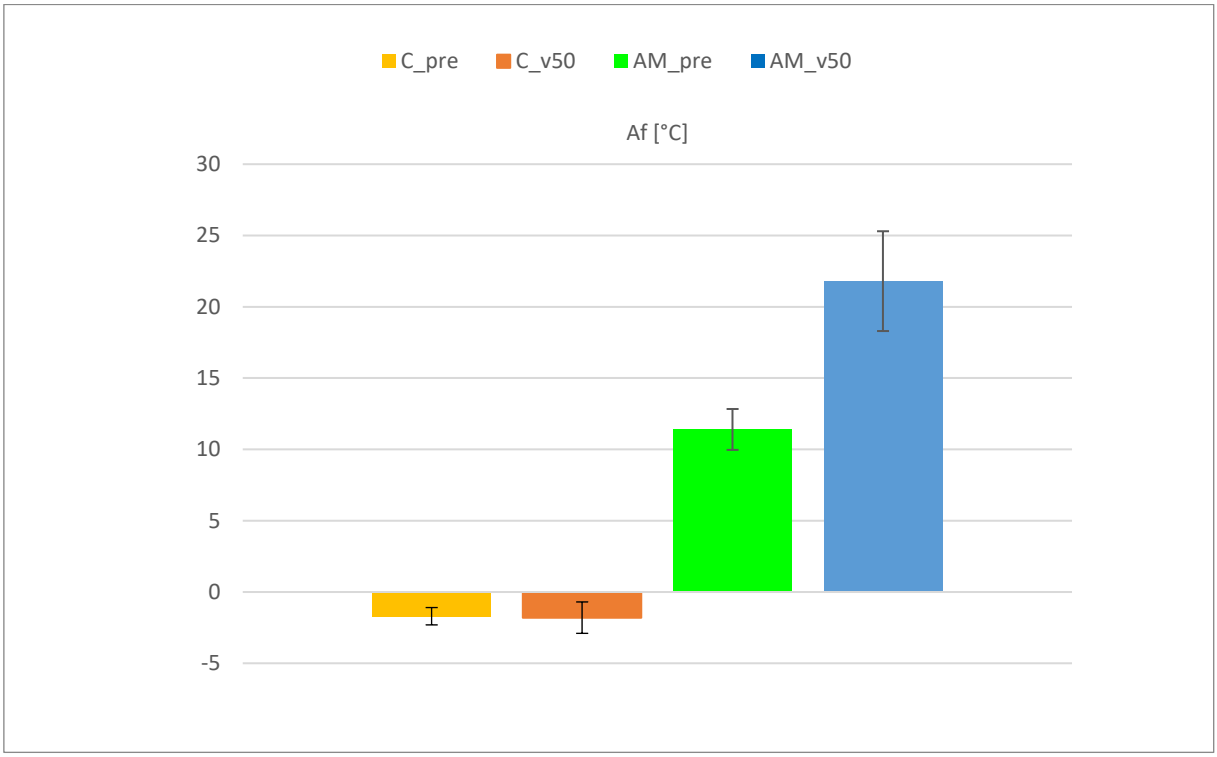

Figure 3.37 Effects of manufacturing method in Af.

Concerning the examination of A_f behavior at the two distinct wear steps (w_min and w_max), it can be asserted that the trend remains consistent for the two materials produced through different methods. However, it is noteworthy that in the additive case, there is a notably greater increase in A_f at the w_min step compared to the conventional NiTi, referring to both v50 and v80. The contrast between the additive and conventional manufacturing method is illustrated in Figure 3.38, focusing strictly on the case of machining at cutting speed 80 m/min for simplicity. Variation in microstructure and mechanical properties, including changes in hardness and ductility, can impact wear resistance and contribute to disparities in A_f behavior. Moreover, the layer-by-layer deposition in additive manufacturing results in distinct grain structures and orientations, while residual thermal and stress effects, arising from rapid heating and cooling

cycles and the introduction of residual stresses, further differentiate the additive process form conventional methods. These factors collectively contribute to heightened variation observed in A_f during the progressive tool wear study in case of AM pieces.

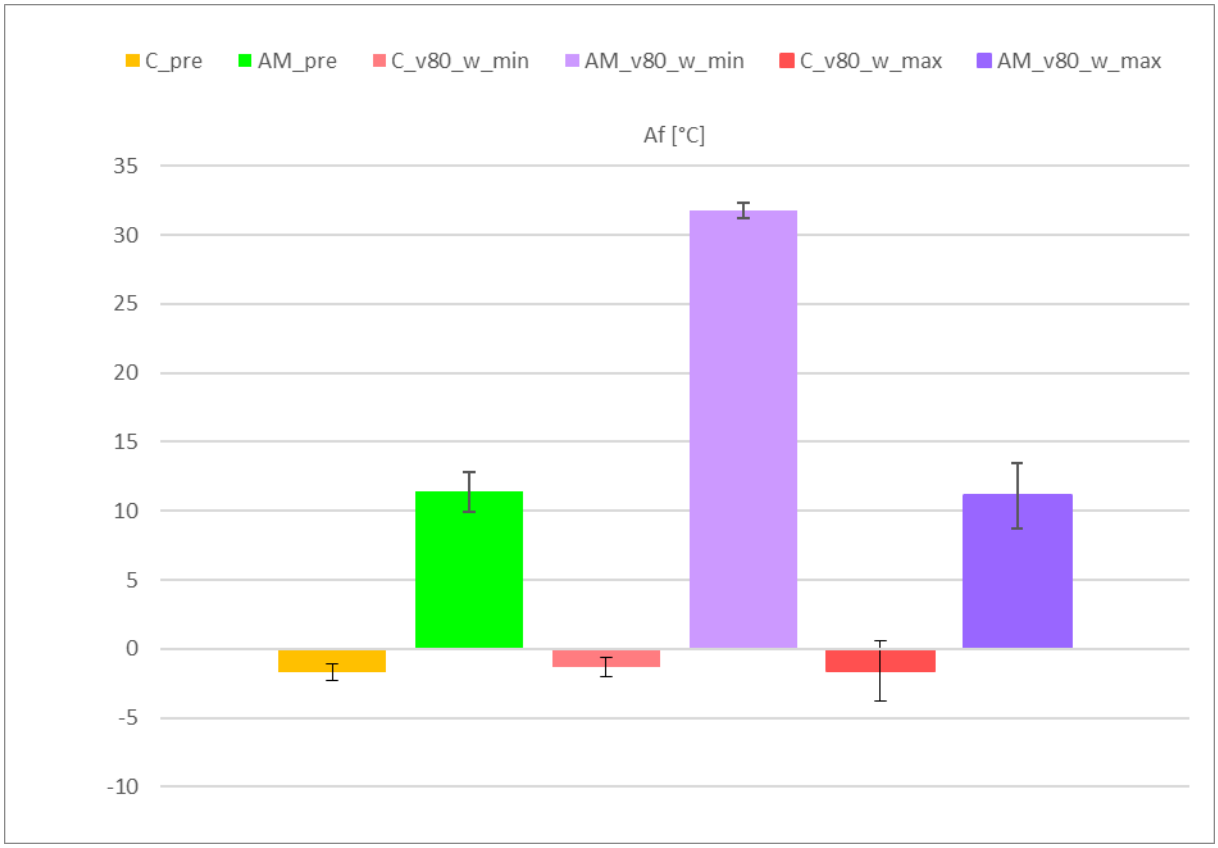

Figure 3.38 Tool-wear effect on Af in v80 case comparing C and AM.

3.2.2.3 Microstructural Analysis

When comparing the SPD layer between conventional manufacturing and additive manufacturing, the observations under the optical microscope revealed that the conventional method produces a thicker SPD layer compared to additive manufacturing (see Figure 3.39 and Figure 3.40). Additionally, a consistent trend emerged: regardless of the manufacturing technique, the SPD layer thickness at the maximum wear step consistently exceeds that at the minimum step. This highlights the significance of comprehending the intricacies of surface plastic deformation across various manufacturing methodologies. Specifically, at a constant speed of 50 m/min, in case C, there is a 100% increase in the SPD layer between the minimum wear step and the maximum wear step, while in case AM, the increase is 41%. At a speed set at 80 m/min, case C sees a 25% increase in the SPD layer as wear increases, while in case AM, the increase is 100%.

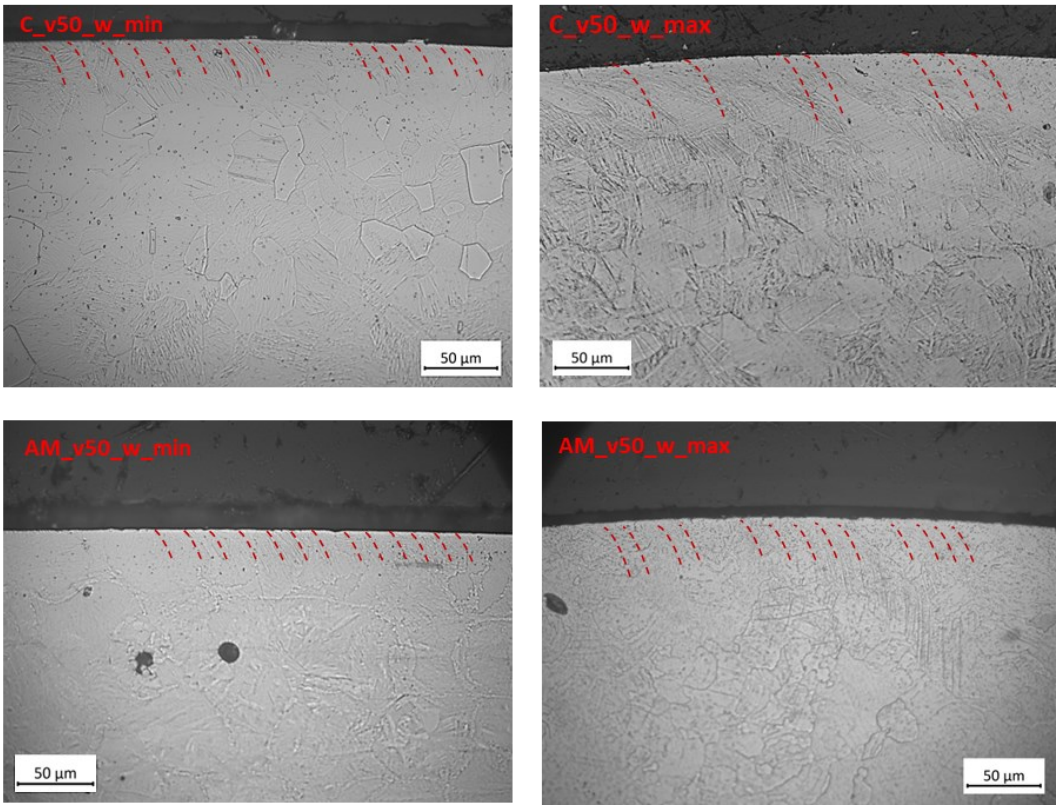

Figure 3.39 Effects of manufacturing method on SPD layer in case of v=50 m/min.

The thickness of the SPD layer, calculated by measuring the depth of this layer on the microscope image at 200x magnification, is depicted in the Figure 3.40, providing tangible evidence supporting the observations previously outlined.

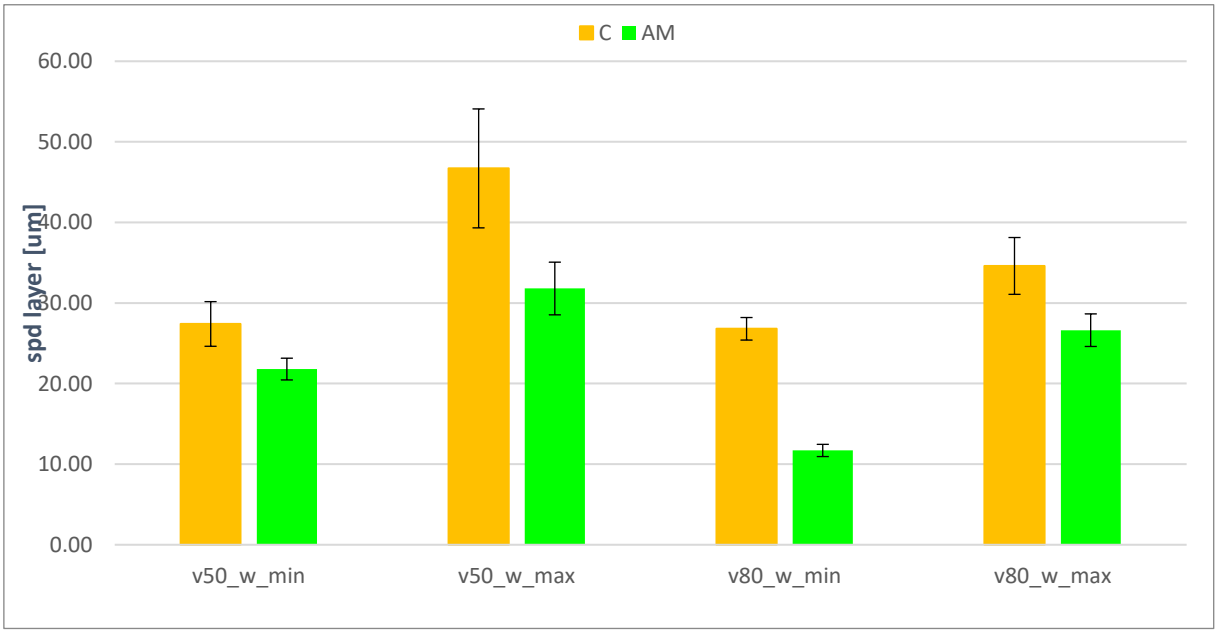

Figure 3.40 SPD layer thickness.

3.2.2.4 Roughness Analysis

Concerning the effects of different manufacturing methods on the surface roughness of the workpiece, the graphs illustrating the mean values of *Ra* parameter obtained from the analysis to the profiler are shown below.

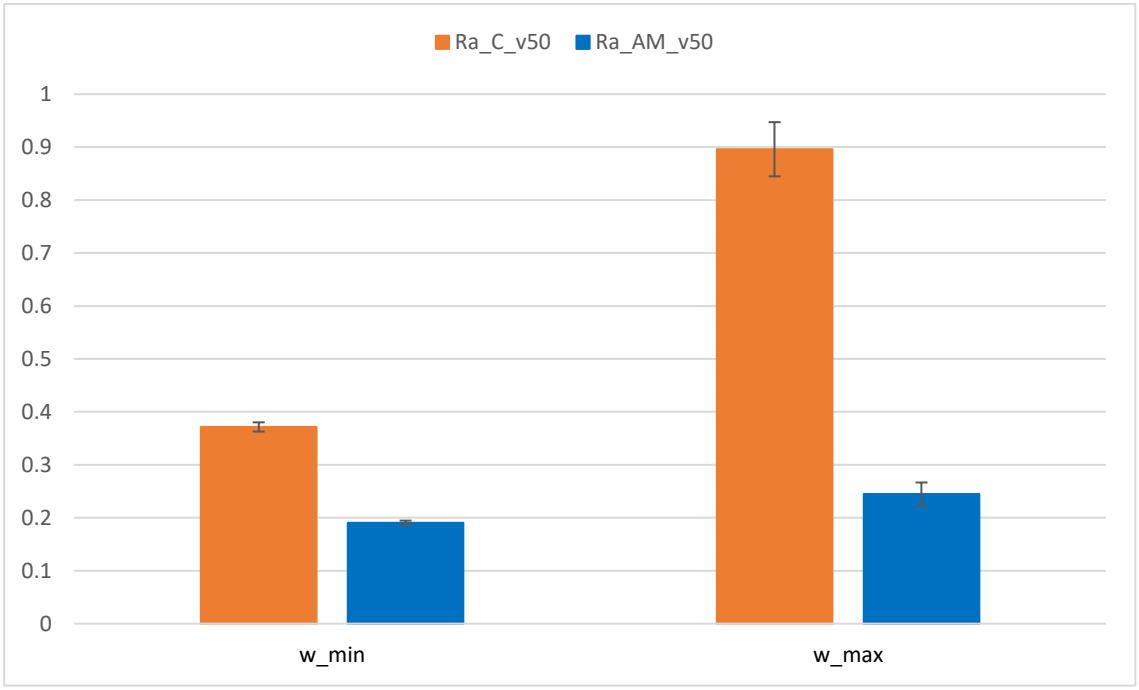

Figure 3.41 Effects of manufacturing in Ra for cutting speed of 50 m/min.

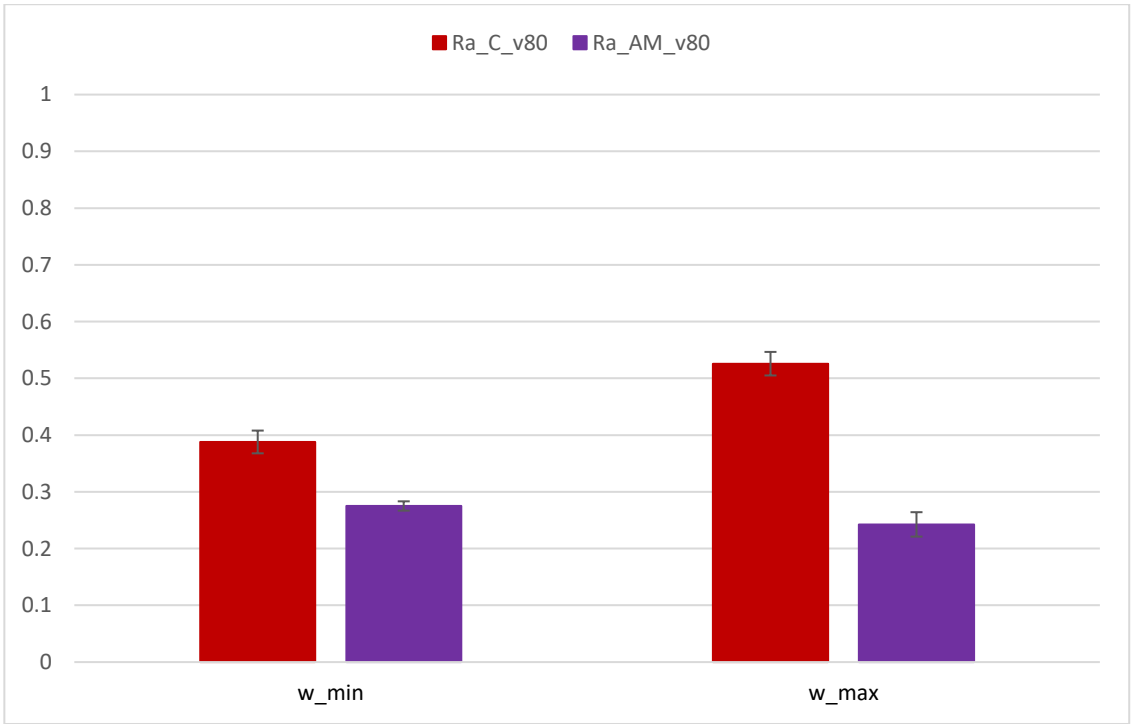

Figure 3.42 Effects of manufacturing in Ra for cutting speed of 80 m/min.

In Figure 3.41, the *Ra* values are reported for the case where machining was carried out at cutting speed of 50 m/min. Observations indicate that additive production yields Ra values lower than those from traditional methods, with a 49% decrease during minimal wear and a 78% decrease during maximal wear. The same trend applies in the case of machining conducted at speeds of 80 m/min, as evident in the graph shown in Figure 3.42. *Ra* is 29% and 52% lower for minimum and maximum wear step respectively.

3.2.2.5 Machining Forces Analysis

The force acquisitions were subsequently analyzed to delineate differences between the two distinct manufacturing methods, while keeping cutting speeds constant. It was found that the additive manufacturing technique is more advantageous than conventional methods in terms of development of forces, registering lower values specifically during machining at 50 m/min (see Figure 3.43, Figure 3.44 and Figure 3.45). Reduced force means lower power consumption. To support this findings, two histograms are presented below (Figure 3.46, Figure 3.47 and Figure 3.48) comparing the average force values acquired during the machining of the two NiTi types, with particular emphasis on stages of minimum and maximum wear. The radial force (Fr) diminishes drastically by 94%, while the cutting force component (Fc) experiences a 63% decrease, and the feed force component (Ft) sees a significant 70% reduction.

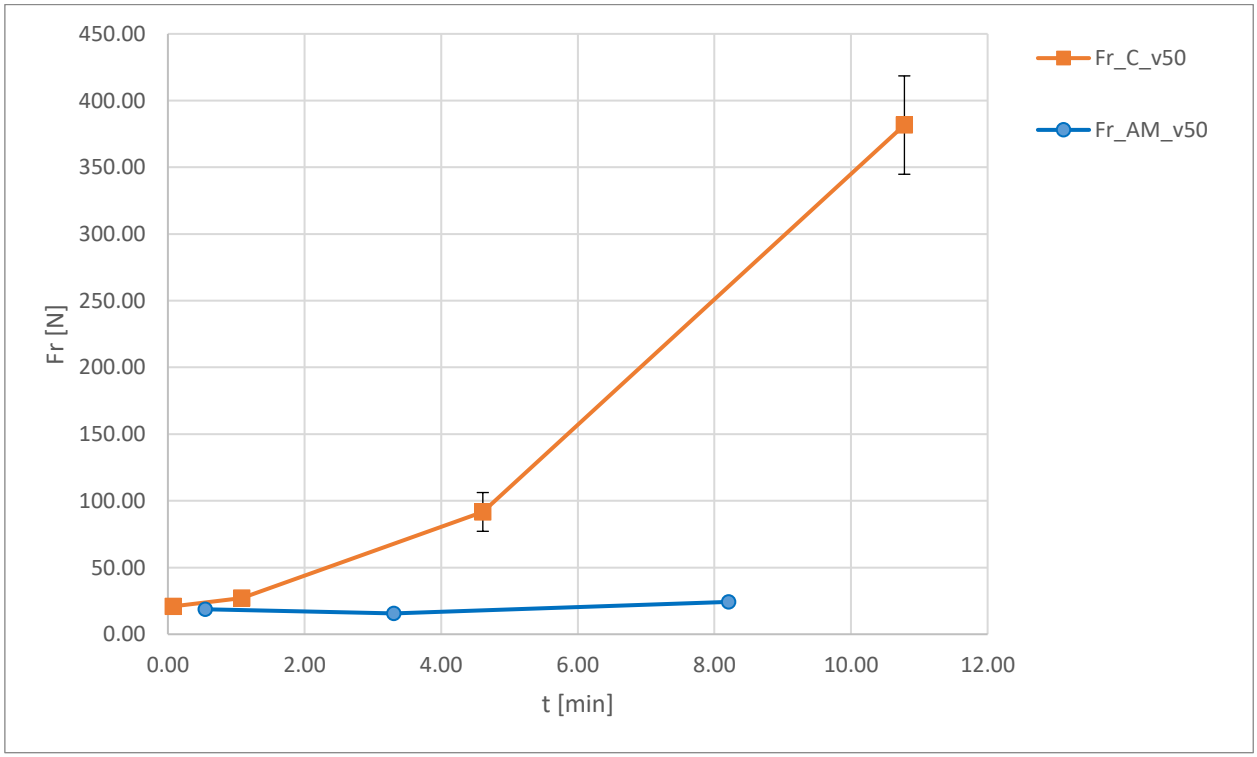

Figure 3.43 Variation of radial force over time for C_v50 and AM_v50.

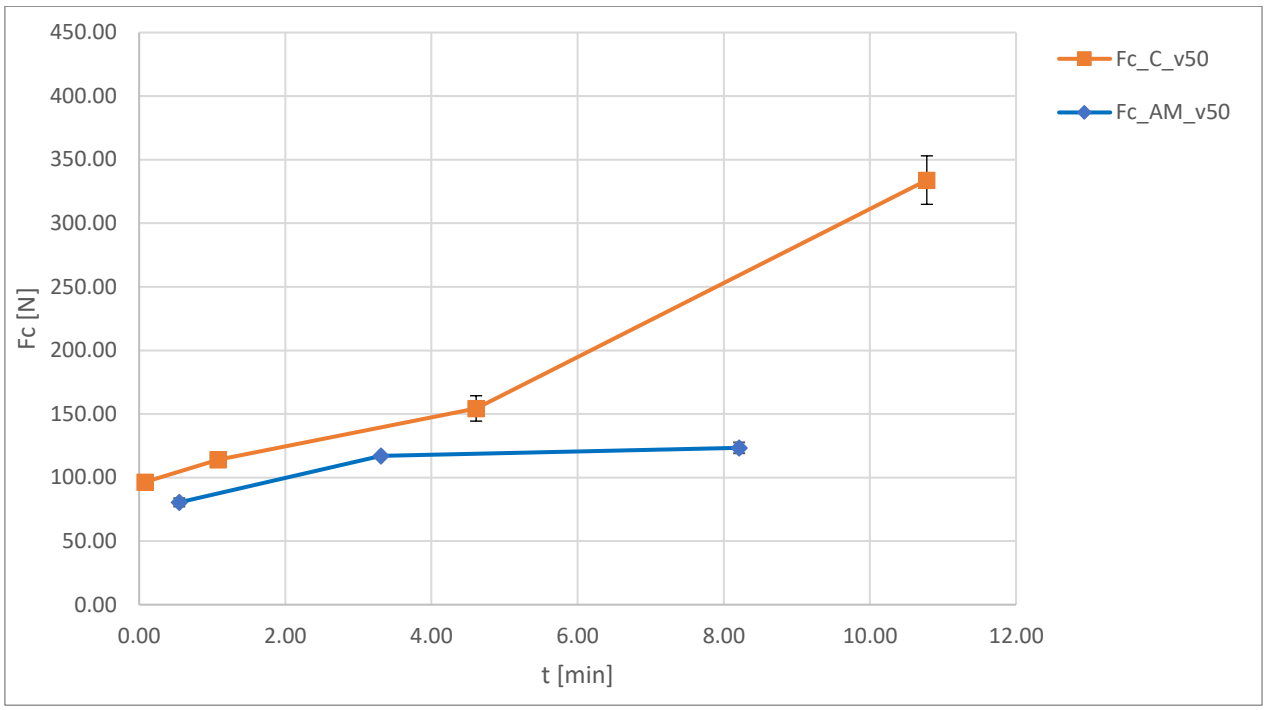

Figure 3.44 Variation of cutting force over time for C_v50 and AM_v50.

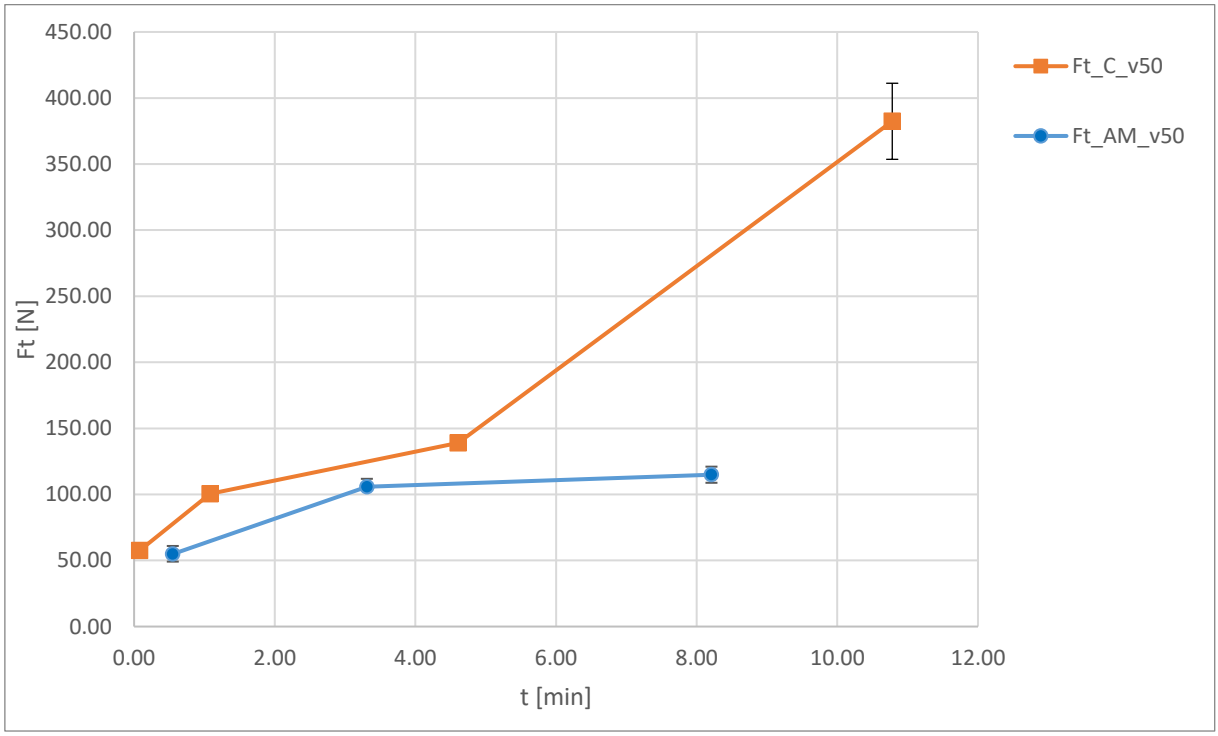

Figure 3.45 Variation of feed force over time for C_v50 and AM_v50.

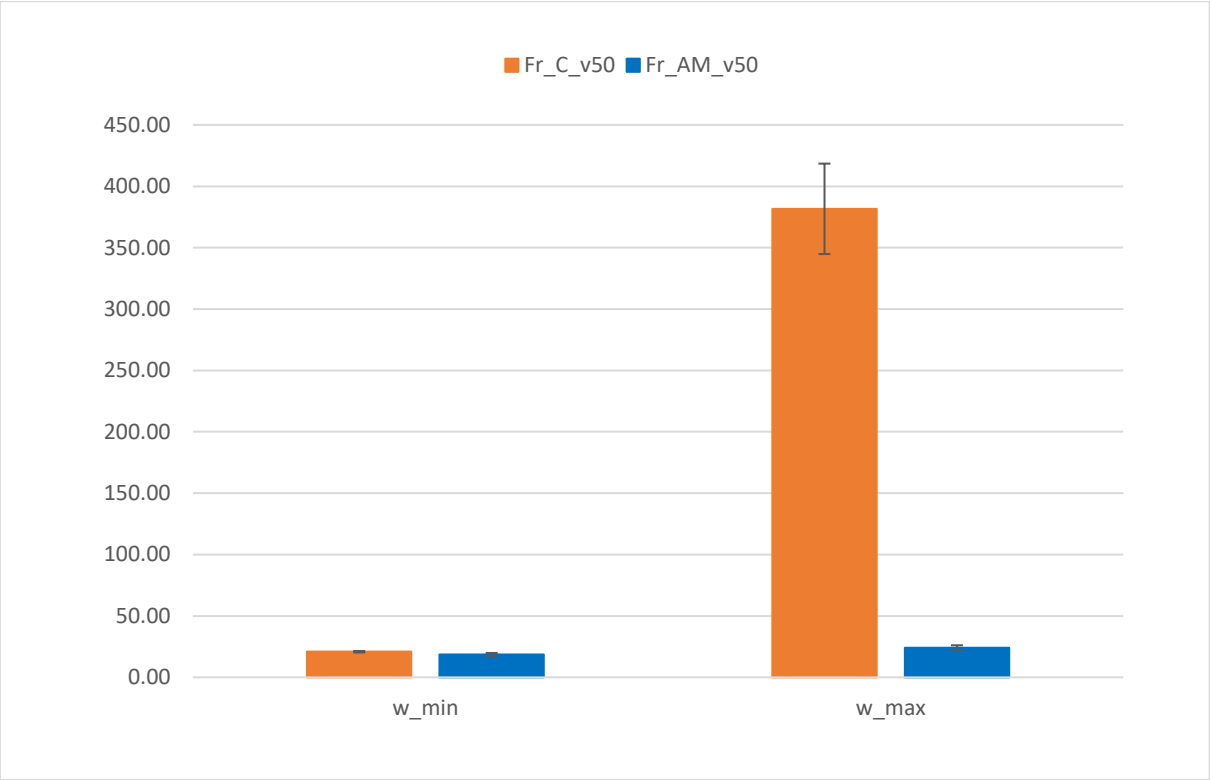

Figure 3.46 Effects of manufacturing in Fr for cutting speed of 50 m/min.

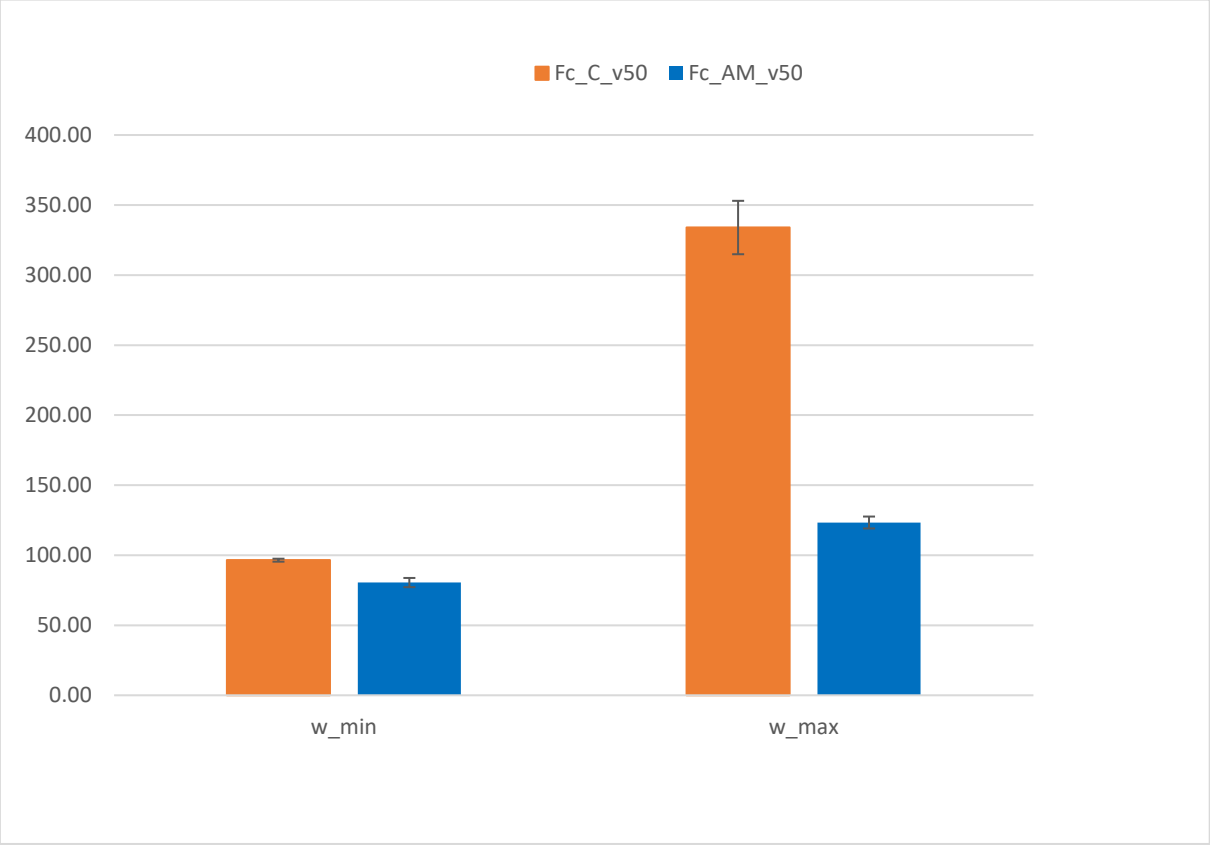

Figure 3.47 Effects of manufacturing in Fc for cutting speed of 50 m/min.

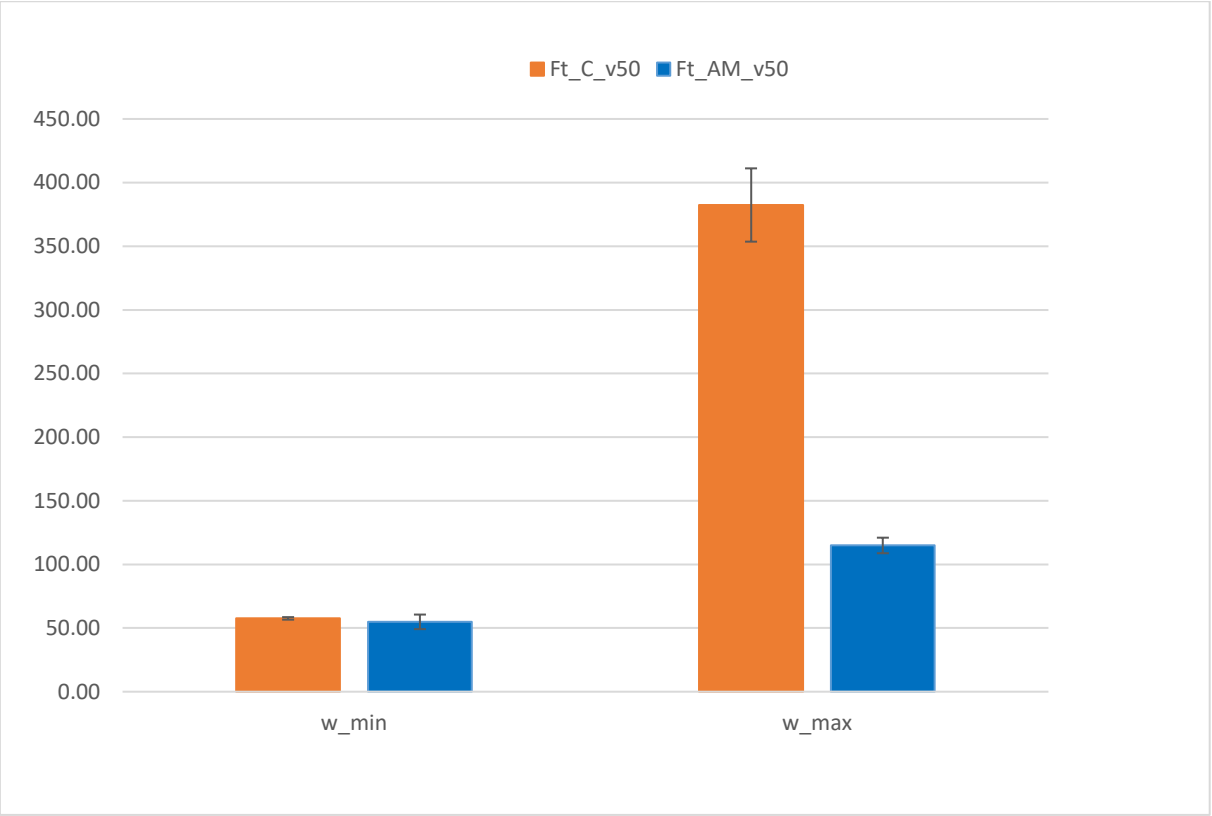

Figure 3.48 Effects of manufacturing in Ft for cutting speed of 50 m/min.

CHAPTER 4

4. CONCLUSIONS AND FURTHER DEVELOPMENTS

The aim of this study was to investigate the effects of tool-wear on the characteristics of NiTi (with a composition of 50.8% atomic Ni and 49.2% atomic Ti), above all its remarkable super-elastic behavior, under different machining conditions and manufacturing methodologies. While numerous prior investigations have delved into tool-wear progression on machining of a wrought NiTi, this research would aim to examine tool wear on a NiTi manufactured with a process chain involving the additive manufacturing of superelastic powders with subsequent heat treatment followed by machining. Results were analyzed by comparing two cutting speeds, namely 50 m/min and 80 m/min and two distinct manufacturing methods of Nitinol: conventional and additive. An attempt was made to assess the outcomes focusing on the minimum and maximum wear steps. These steps mark the point where the tool has operated for approximately one minute and when it reaches its end-of-life criterion (VBcmax=0.3mm), respectively. As the diversification of two production methods and cutting speeds are examined, it becomes evident that the comparison between conventional techniques and additive manufacturing reveals particularly interesting disparities. After characterizing the material before turning, the core of the study was the evaluation of the cutting edge life curves, i.e. the determination of the wear curves that each case produced progressively during a turning process. Characterization after machining results were evaluated in terms of alterations in phase temperatures, material microstructure, workpiece roughness and machining forces. Main observed phenomena are summarized as follows.

1. Austenite Finish (*Af*) Temperature Before Turning: The initial DSC analysis revealed that both materials exhibited an Austenite finish temperature below room temperature. However, C NiTi achieved the superelastic condition before AM NiTi. Throughout the transformations, no R-phase peaks, known for their adverse effects on superelasticity, were detected.
2. Microstructural Differences Before Turning: The conventional manufacturing method yield a more homogeneous microstructure compared to additive manufacturing. This is because in conventional method, the material undergoes processes like forging or rolling, which result in a more uniform distribution of grains. In contrast, additive manufacturing involves layer-by-layer deposition, leading to larger grain sizes. The differences in microstructure can affect material properties, including machinability and

response to tool wear. A more uniform microstructure favors a more even distribution of stresses during machining, thus reducing the risk of tool cracks and fractures.

3. Austenite Finish (*Af*) Temperature After Turning: The observed increase in Af during minimal wear in the additive manufacturing process suggests that machining decrease material SE, because of martensite formation during cutting, which reduces the amount of austenite that capable of undergoing the superelastic transformation. However, as wear progresses, the austenite phase becomes dominant again, leading to a return to pre-processing *Af* values. This behavior indicates a reversible phase transformation under different wear conditions which will have to be deepened.
4. SPD layer Thickness: The thicker SPD layer observed in the conventional method can be attributed to the finer grain structure, which results in less ductility and more localized plastic deformation during machining. In contrast, the additive manufacturing process produces larger grain sizes, which increase material ductility and distribute plastic deformation more evenly, resulting in a thinner SPD layer.

   It's important to note that there's a lack of correlation between SPD and *Af* variation. This suggest that other factors, such as local temperature gradients and stress concentrations, may influence the phase transformation behavior during machining.
5. Workpiece Roughness: the superior surface finish in additive process, especially at lower cutting speeds, can be attributed to the layer-by-layer deposition method, which results in lower surface irregularities. A finer control over process parameters in AM allows optimized surface quality.
6. Machining Forces: the lower forces observed during AM compared to C machining are a result of a reduced material removal and less resistance to tool cutting movement. Lower processing forces result in lower process energy consumption.

These results underline the complex interplay between material properties, manufacturing methods and machining conditions in NiTi processing, thus highlighting the need for further studies on machining conditions that can help improve overall process efficiency and reduce production costs.

Future studies recommended to explore nanoindentation tests for quantifying superelasticity and assessing material elastic modulus, hardness, thereby enhancing understanding of tool wear effects on NiTi properties, particularly in additive manufacturing processes.

BIBLIOGRAPHY

[1] A. Concilio and L. Lecce, “Historical background and future perspectives,” in *Shape Memory Alloy Engineering: For Aerospace, Structural, and Biomedical Applications*, Elsevier, 2021, pp. 3–52. doi: 10.1016/B978-0-12-819264-1.00001-7.

[2] E. Patoor, D. C. Lagoudas, P. B. Entchev, L. C. Brinson, and X. Gao, “Shape memory alloys, Part I: General properties and modeling of single crystals,” *Mechanics of Materials*, vol. 38, no. 5–6, pp. 391–429, May 2006, doi: 10.1016/j.mechmat.2005.05.027.

[3] Y. Guo, A. Klink, C. Fu, and J. Snyder, “Machinability and surface integrity of Nitinol shape memory alloy,” *CIRP Ann Manuf Technol*, vol. 62, no. 1, pp. 83–86, 2013, doi: 10.1016/j.cirp.2013.03.004.

[4] M. Maroof, R. Sujithra, and R. P. Tewari, “Superelastic and shape memory equi-atomic nickel-titanium (Ni-Ti) alloy in dentistry: A systematic review,” *Materials Today Communications*, vol. 33. Elsevier Ltd, Dec. 01, 2022. doi: 10.1016/j.mtcomm.2022.104352.

[5] M. H. Elahinia, M. Hashemi, M. Tabesh, and S. B. Bhaduri, “Manufacturing and processing of NiTi implants: A review,” *Progress in Materials Science*, vol. 57, no. 5. Elsevier Ltd, pp. 911–946, 2012. doi: 10.1016/j.pmatsci.2011.11.001.

[6] S. K. Patel, B. Behera, B. Swain, R. Roshan, D. Sahoo, and A. Behera, “A review on NiTi alloys for biomedical applications and their biocompatibility,” in *Materials Today: Proceedings*, Elsevier Ltd, 2020, pp. 5548–5551. doi: 10.1016/j.matpr.2020.03.538.

[7] M. Nematollahi, K. S. Baghbaderani, A. Amerinatanzi, H. Zamanian, and M. Elahinia, “Application of NiTi in assistive and rehabilitation devices: A review,” *Bioengineering*, vol. 6, no. 2. MDPI AG, 2019. doi: 10.3390/bioengineering6020037.

[8] J. P. Y. Cheung, D. Samartzis, K. Yeung, M. To, K. D. K. Luk, and K. M. C. Cheung, “A randomized double-blinded clinical trial to evaluate the safety and efficacy of a novel superelastic nickel–titanium spinal rod in adolescent idiopathic scoliosis: 5-year follow-up,” *European Spine Journal*, vol. 27, no. 2, pp. 327–339, Feb. 2018, doi: 10.1007/s00586-017-5245-x.

[9] M. Elahinia, N. Shayesteh Moghaddam, M. Taheri Andani, A. Amerinatanzi, B. A. Bimber, and R. F. Hamilton, “Fabrication of NiTi through additive manufacturing: A review,” *Progress in Materials Science*, vol. 83. Elsevier Ltd, pp. 630–663, Oct. 01, 2016. doi: 10.1016/j.pmatsci.2016.08.001.

[10] M. T. Andani, N. Shayesteh Moghaddam, C. Haberland, D. Dean, M. J. Miller, and M. Elahinia, “Metals for bone implants. Part 1. Powder metallurgy and implant rendering,” *Acta Biomaterialia*, vol. 10, no. 10. Elsevier Ltd, pp. 4058–4070, Oct. 01, 2014. doi: 10.1016/j.actbio.2014.06.025.

[11] R. Bertolini, S. Bruschi, A. Ghiotti, E. Savio, L. Ceseracciu, and I. S. Jawahir, “Surface integrity and superelastic response of additively manufactured Nitinol after heat

treatment and finish machining," *CIRP Annals*, vol. 72, no. 1, pp. 501–504, Jan. 2023, doi: 10.1016/j.cirp.2023.04.025.

[12] S. Khademzadeh, F. Zanini, J. Rocco, K. Brunelli, P. F. Bariani, and S. Carmignato, "Quality enhancement of microstructure and surface topography of NiTi parts produced by laser powder bed fusion," *CIRP J Manuf Sci Technol*, vol. 31, pp. 575–582, Nov. 2020, doi: 10.1016/j.cirpj.2020.08.009.

[13] M. R. Hassan, M. Mehrpouya, and S. Dawood, "Review of the machining difficulties of nickel-titanium based shape memory alloys," in *Applied Mechanics and Materials*, Trans Tech Publications Ltd, 2014, pp. 533–537. doi: 10.4028/www.scientific.net/AMM.564.533.

[14] H. Yang, K. Sakai, H. Shizuka, Y. Kurebayashi, K. Hayakawa, and T. Nagare, "Experimental investigation of the effects of super-elasticity on the machinability of NiTi alloys", doi: 10.1007/s00170-021-07166-4/Published.

[15] "ISO 3685".

[16] A. Bordin, S. Bruschi, A. Ghiotti, and P. F. Bariani, "Analysis of tool wear in cryogenic machining of additive manufactured Ti6Al4V alloy," *Wear*, vol. 328–329, pp. 89–99, Apr. 2015, doi: 10.1016/j.wear.2015.01.030.

[17] Y. Kaynak, S. W. Robertson, H. E. Karaca, and I. S. Jawahir, "Progressive tool-wear in machining of room-temperature austenitic NiTi alloys: The influence of cooling/lubricating, melting, and heat treatment conditions," *J Mater Process Technol*, vol. 215, pp. 95–104, 2015, doi: 10.1016/j.jmatprotec.2014.07.015.

[18] Y. Kaynak, H. E. Karaca, R. D. Noebe, and I. S. Jawahir, "Tool-wear analysis in cryogenic machining of NiTi shape memory alloys: A comparison of tool-wear performance with dry and MQL machining," *Wear*, vol. 306, no. 1–2, pp. 51–63, Aug. 2013, doi: 10.1016/j.wear.2013.05.011.

[19] I. S. Jawahir, P. X. Lil, R. Gosh', and E. L. Exner2, "A New Parametric Approach for the Assessment of Comprehensive Tool Wear in Coated Grooved Tools."

[20] "Q Series TM Getting Started Guide DSC Differential Scanning Calorimeter," 2007.

[21] "ASTM F2004-17".

[22] S. R. Schmi, "Serop e Kalpa kjian."

[23] Y. Kaynak, H. E. Karaca, and I. S. Jawahir, "Surface integrity characteristics of NiTi shape memory alloys resulting from dry and cryogenic machining," in *Procedia CIRP*, Elsevier B.V., 2014, pp. 393–398. doi: 10.1016/j.procir.2014.04.067.